Ph.D. Thesis

The complex physics of photoinduced charge carriers in novel materials

András Bojtor

Supervisor:

Ferenc Simon

Department of Physics

Budapest University of Technology and Economics

Industrial advisor:

Gábor Paráda

Semilab Semiconductor Physics Laboratory Co. Ltd.

Budapest
2024

Contents

1 Introduction and Motivation **5**

2 Theoretical Background **7**
2.1 Semiconductors 7
2.1.1 Conventional semiconductors 7
2.1.2 Perovskite semiconductors 10
2.1.3 Wide bandgap semicondcutors 14
2.2 Generation and recombination of charge carriers 16
2.3 Detection of photoexcited charge carriers 21
2.3.1 Measuring charge carrier density through the surface impedance 22
2.3.2 Transient and steady-state methods for the measurement of charge carrier density 26
2.3.3 Charge carrier density dependent recombination time measurement . . 28
2.4 Transport properties of multiband charge carriers 28
2.4.1 The van der Pauw method for sheet resistance measurement 28
2.4.2 Hall effect measurement 31

3 Experimental Methods **35**
3.1 Microwave photoconductivity decay measurements 35
3.1.1 Evaluation of charge-carrier recombination dynamics 35
3.1.2 CPW-based experiment 36
3.1.3 Cavity-based experiment 43
3.2 Hall effect and sheet resistance measurement 44
3.3 Studied samples 45

4 Charge-Carrier Dynamics in Hybrid Organic-Inorganic Perovskites **47**
4.1 Measurement of charge-carrier recombination time and photoconductivity with a microwave cavity 48
4.2 Temperature dependent charge-carrier lifetime in methylammonium lead halides 51
4.3 Reproducibility of the measurements 54
4.4 Quenching the crystal structure 54
4.5 Effect of Morphology 57
4.5.1 $MAPbBr_3$ 57
4.5.2 $MAPbI_3$ 58
4.6 Conclusions 59

5 Charge-Carrier Dynamics in Inorganic Perovskites: Cesium Lead Bromide 61
5.1 CPW-based microwave photoconductivity measurement 62
5.2 The microwave photoconductivity decay measurement of $CsPbBr_3$ single crystals 64
5.3 Temperature-dependent microwave reflection in dark conditions 65
5.4 Evaluation of the charge-carrier recombination dynamics 66
5.5 Temperature dependent recombination dynamics in the $CsPbBr_3$ perovskites . . 68
5.6 Trapping of charge carriers: model, simulation, and the explanation for ultra-long charge-carrier recombination times 72
5.7 Conclusions 77

6 Persistent Photoconductivity in Wide Bandgap Semiconductors 79
6.1 Observation of persistent photoconductivity 79
6.2 Amorphous Indium Gallium Zinc Oxide 80
6.3 α-Ga_2O_3 87
6.4 Conclusions 88

7 Summary and Thesis Points 91

List of Publications 93

Bibliography 97

List of Figures 115

Acknowledgement

I would like to express my gratitude to my supervisor, Prof. Ferenc Simon, for the time and patience he spared to shape my knowledge about and approach to scientific problems and questions. Without his support and help this thesis - and many others, I believe - would not have been written. I am thankful for the last 8 years and hope that, in some form, we will work on research projects together in the future.

I would like to thank Prof. László Forró for the opportunities he provided over the years. My interest and research in the field of photovoltaic materials, especially perovskites, started with a one-month internship in his laboratory at the École Polytechnique Federal de Lausanne. His support of my research with instruments, possibilities, and materials enabled most of the presented results.

I would like to thank Gábor Paráda who showed me how research and development is done outside the university. I learned a lot of important skills and knowledge from him.

I am grateful to Semilab Semiconductor Physics Laboratory Co. Ltd. for the opportunity and assistance connected to the KDP grant. This research was realized due to the opportunity provided by Semilab to not only pursue the development of devices but scientific research as well.

I am thankful for the guidance, enlightening discussions, and explanations of Dr. Sándor Kollarics who taught me the basics of most methods and tools I use on a daily basis.

I am thankful for the support of Dr. Bence G. Márkus who could always answer my questions. His numerous comments and suggestions helped form our publications into presentable scientific discussions.

I would like to thank Dr. Márton Kollár, Dr. Endre Horváth, and Dr. Xavier Mettan for providing the group with perovskite single crystals of outstanding quality. The samples enabled the measurements presented in this thesis.

I would like to thank Hitoshi Takane for the α-Ga_2O_3 thin films he provided for the measurements. These thin films enabled the measurements presented in this thesis.

I am indebted to Dr. Richard Gaál for the help with the cryogenic photoconductivity decay instrument. Without his help in obtaining the instrument the measurement setup could not have been realized in the way it was. This enabled two of the four publications presented in this thesis.

I would like to thank Ferenc Korsós, Dávid Krisztián, and Dr. Péter Tüttő for always providing the theoretical background and explanation of effects and results.

I am thankful to the colleagues that helped with the research and publication of results presented in this thesis: Gábor Csősz, Dr. Andrzej Sienkiewicz, Dr. Péter Szirmai, Dr. Konstantins Mantulnikovs, Anastasiia Glushkova, Dr. Hidetsugu Shiozawa, and Thomas Pinel.

No experimental work was ever completed at the Department of Physics without the skillful

hands of Béla Horváth and Márton Hajdú. I am thankful for their help.

I would like to thank my family for always trusting and helping me on this long journey. Without their support, I could not have achieved this feat.

I would like to express my gratitude to Bori, who supported me during the long years of research leading to this point and the nerve-wracking process of writing this thesis.

Project no. C1530638 has been implemented with the support provided by the Ministry of Culture and Innovation of Hungary from the National Research, Development and Innovation Fund, financed under the KDP-2021 funding scheme.

This thesis was also supported by the K137852, 2022-2.1.1-NL-2022-00004, 2019-2.1.7-ERA-NET-2021-00028 (V4-Japan, BGapEng), TKP2021-NVA-02 and TKP2021- EGA-02 grants of the NRDIF.

Chapter 1

Introduction and Motivation

The technological leaps of the past century led to an ever-increasing need for new materials and technologies in the photovoltaic and semiconductor industries. The energy needs of humanity skyrocketed and the increasing demand for green solutions to fulfill this demand is propelling the research and development of photovoltaic devices and materials. Technological advances in fields ranging from electric cars to consumer electronics lead to an increased need for more reliable, cheaper, easier-to-produce materials to be used in electrical components such as thin-film transistors, power electronics, and transparent conductors.

The metal-halide perovskites emerged as candidate materials for a wide range of applications due to their low fabrication cost, ease of manufacturing, and extraordinary photovoltaic properties[1–3]. Due to the fact that the optical properties of the materials can be tuned by selecting the halide ratio in a mixed halide perovskite[4, 5], these materials are outstanding candidates for light emitting[3, 5–7] and harvesting [1, 8–11] purposes. The solar cells based on metal-halide perovskites currently surpass 26% efficiency[12] and the material is proposed to be useable even in harsh environments such as outer space[13, 14]. The possible applications extend to the usage as gas sensors[15], photodetectors[16, 17], X-ray[18], gamma[19] and neutron[20] detectors.

Understanding sample properties and the effect of manufacturing processes and material composition is essential for realizing such a wide spectrum of applications. To this end, I investigated the temperature-dependent charge-carrier recombination time in methylammonium lead halide and cesium lead bromide perovskites. Studying the temperature-dependent recombination dynamics can enhance our understanding of the underlying physical processes, enabling the development of materials with optimized properties for specific applications and improving future devices.

Wide bandgap materials such as indium gallium zinc oxide and gallium oxide are intensively studied due to their potential use in areas where conventional semiconductors with narrower bandgap are not ideal, such as in high temperature conditions or power applications. The first thin-film transistor based on indium gallium zinc oxide was reported by Nomura *et al*. for both the single crystalline [21] and amorphous form [22] as late as in 2003 and 2004. Gallium oxide thin-films can be created in five structures. The most stable and thus widely used variation is the β-Ga_2O_3 variant that has a monoclinic structure, the α-Ga_2O_3 variant has the rhombohedral structure[23]. Much as the metal oxide semiconductors are suitable candidates for flat panel displays[24–26], flexible displays [27–29], power electronics[30], and a wide range of sensory applications [31–38], on the downside they exhibit persistent photoconductivity effect caused

by oxygen vacancy defects. The proper comparison and characterization of thin films that show the persistent photoconductivity effect is problematic due to the long-lasting change caused by optical excitation. I developed a measurement method that allows for the reliable comparison of samples that present the persistent photoconductivity phenomena.

In this thesis, I present the recombination dynamics of photoexcited charge carriers in novel semiconductors. The presented research is focused on perovskites in the form of methylammonium lead halide and cesium lead halide and metal oxides in the form of amorphous indium gallium zinc oxide and α gallium oxide thin films. The temperature-dependent charge-carrier recombination time of the perovskite crystals was investigated with the microwave photoconductivity decay measurement technique. The observation of the persistent photoconductivity effect and the measurement of wide bandgap semiconductors was realized with the PDL-1000 Hall effect measurement system of Semilab Semiconductor Physics Laboratory Co. Ltd. as the present thesis is the result of industry-academia partnership.

Contents of the thesis The structure of the thesis is as follows: First, the theoretical background of semiconductors, charge-carrier recombination processes and the theory of measurement methods are presented. A detailed description of the experimental systems used during the measurement processes is given in the next chapter. This is followed by chapters 4 through 6 presenting the results that serve as the basis for the thesis points. The results are summarized in Chapter 7 in the form of the thesis points.

Chapter 2

Theoretical Background

2.1 Semiconductors

2.1.1 Conventional semiconductors

In solid state physics, one kind of possible distinction that can be made between materials is based on the band structure. The three types of material in this regard are insulators, conductors, and semiconductors. The distinction between these materials is based on whether the highest energy band that has electrons in it is fully or partially filled and the size of the bandgap which is the gap between the conduction and valence band where electrons cannot occupy energy values. Figure 2.1. presents the difference between the band structure of conductors and insulators.

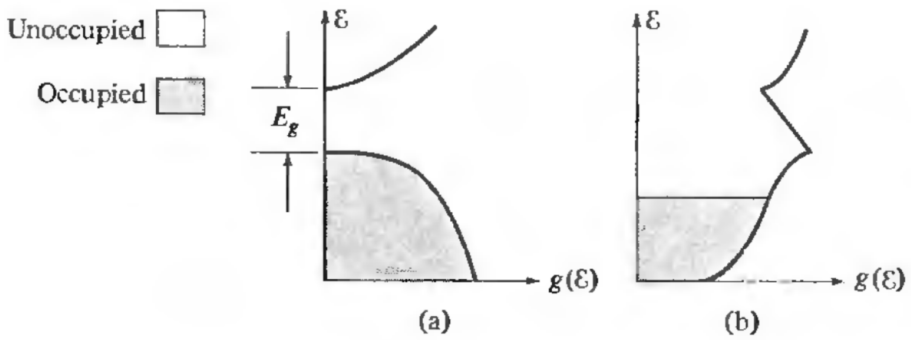

Figure 2.1: The band structure of a semiconductor or insulator is shown in subfigure (a) with a filled valence band and a bandgap between the valence and conduction band. The band structure of a conductor is shown in subfigure (b) with a partially filled band. $g(\varepsilon)$ is the density of states at a given ε energy, E_g is the bandgap. The figure is from *Solid State Physics* by Neil W. Ashcroft and N. David Mermin [39].

In the tight-binding approximation[40] the band structure of electrons in solid state materials is calculated by regarding electrons bound to atoms with a perturbation to their wavefunctions caused by the other ions of the system. The approximation assumes that there is no substantial overlap between the atomic wavefunction of neighboring atoms. When calculating the tight-binding approximation, we start from a crystal lattice with a very large lattice constant and decrease the distance between the atoms. If an atom acts on electrons with a potential of

$v_{\mathrm{a}}(\vec{r}-\vec{R}_j)$ where $\vec{r}$ is the position of the electrons and the atom is in the position $\vec{R}_j$ then the atomic wavefunctions (w_α) are given as the solution of the Schrödinger equation[40]:

$$\left[-\frac{\hbar}{2m_{\mathrm{e}}}\nabla^2+v_{\mathrm{a}}(\vec{r}-\vec{R}_j)\right]w_\alpha(\vec{r}-\vec{R}_j)=\varepsilon_\alpha w_\alpha(\vec{r}-\vec{R}_j), \tag{2.1}$$

where α represents the principal (n), azimuthal (l), and magnetic (m_l) quantum numbers of a given state, $\hbar$ is the reduced Planck constant, and m_{e} is the electron mass.

When the atoms are apart, the energy levels of atoms are the same and are N times degenerate for N atoms. When the distance between atoms is decreased the overlap of wavefunctions increases leading to the forming of the bands. If the overlap is not strong the wavefunction of the band state α can be sought as a linear combination of atomic wavefunctions[40]:

$$\psi_\alpha(\vec{k},\vec{r})=\frac{1}{\sqrt{N}}\sum_j e^{i\vec{k}\vec{R}_j}w_\alpha(\vec{r}-\vec{R}_j), \tag{2.2}$$

where $\vec{k}$ is the wave vector leading to the energy of α state as[40]:

$$\varepsilon_\alpha(\vec{k})=\varepsilon_\alpha+\sum_l e^{i\vec{k}\vec{R}_l}\int w_\alpha^*(\vec{r}+\vec{R}_l)\left[U(\vec{r})-v_{\mathrm{a}}(\vec{r})\right]w_\alpha(\vec{r})d\vec{r}, \tag{2.3}$$

where $\vec{R}_l=\vec{R}_j-\vec{R}_{j'}$ is the displacement between two lattice points.

By considering the overlap from distant neighbors to be negligible and introducing the $\gamma_\alpha(\vec{R}_l)=-\int w_\alpha^*(\vec{r}+\vec{R}_l)\left[U(\vec{r})-v_{\mathrm{a}}(\vec{r})\right]w_\alpha(\vec{r})d\vec{r}$ notation and calculating the sum over the lattice points leads to the energy values as[40]:

$$\varepsilon_\alpha(\vec{k})\approx\varepsilon_\alpha-\sum_l{}' e^{i\vec{k}\delta_l}\gamma_\alpha(\delta_l), \tag{2.4}$$

where the calculation only considers the nearest neighbors. With this model, it is possible to calculate the energy of electrons in the atomic s and p states.

Conductors are materials that have a partially filled band as the highest energy band with electrons in it. The charge carriers in these materials can move freely in the presence of an external electric field without the need for optical or thermal excitation. Insulators are materials that have a fully filled valence band while no electrons are present in the conduction band. The bandgap between the valence and conduction band is of such proportion in these materials that thermal excitation can not excite charge carriers from the conduction to the valence band.

Semiconductors fall between insulators and conductors in regard to resistivity[1]. These materials have a completely filled valence band and an empty conduction band. The gap between the conduction and valence bands are of such proportion that the thermal excitation of electrons from the valence to the conduction band is possible leaving behind a hole in the valence band. When charge carriers are excited from the valence to the conduction band the excited electron and the hole that is left behind can move freely in the material. If an external electric field is applied these charge carriers can move according to the force acting upon them. The resistance of semiconductors thus decreases as the temperature increases, since the conductivity of

[1] I note however, that the distinction between semiconductors and insulators is rather convention-based and somewhat artificial: diamond with a bandgap of about 5.5 eV is sometimes considered as a semiconductor as it can be doped to become a metal. On the other hand, Si_3N_4 with a bandgap between $3-4$ eV (depending on morphology) is mostly considered as an insulator when used as an insulating layer.

semiconductors is proportional to the density of mobile charge carriers as $\sigma = \frac{n_e e^2 \tau}{m_e^*} = n_e e \mu_e$ where μ is the charge carrier mobility, n is the charge carrier concentration, τ is the mean time between collision events of electron-electron scattering, and e denotes electrons[39]. This is a significantly different tendency from the temperature-dependence of conductivity in metals since the conductivity of metals decreases as the temperature increases. This is due to the fact that the mean time between scattering events decreases with increasing temperatures while the charge carrier density is unaffected by the change in temperature.

For semiconductors to exhibit conduction, charge carriers must be excited from the valence to the conduction band. The possible methods of excitation include thermal and optical excitation, in the following thermal excitation is regarded. The number or density of thermally excited charge carriers can be calculated based on the effective mass of electrons (m_e^*) and holes (m_h^*) and the energy values of the bottom of the conduction (ε_c) and top of the valence (ε_v) band. For a quadratic band dispersion, the density of states in the conduction (ρ_c) and valence (ρ_v) band are in three dimensions[40]:

$$\rho_c(\varepsilon) = \frac{1}{2\pi^2}\left(\frac{2m_e^*}{\hbar^2}\right)^{3/2}\sqrt{\varepsilon - \varepsilon_c}, \tag{2.5}$$

$$\rho_v(\varepsilon) = \frac{1}{2\pi^2}\left(\frac{2m_h^*}{\hbar^2}\right)^{3/2}\sqrt{\varepsilon_v - \varepsilon}. \tag{2.6}$$

To obtain the charge carrier density the Fermi-Dirac distribution is used[39, 40]. The concentration of electrons in the conduction band ($n(T)$) and holes in the valence band ($p(T)$) as a function of temperature are

$$n(T) = \int_{\varepsilon_c}^{\infty} \rho_c(\varepsilon)\frac{1}{e^{(\varepsilon-\mu)/k_B T}+1}d\varepsilon, \tag{2.7}$$

$$p(T) = \int_{-\infty}^{\varepsilon_v} \rho_c(\varepsilon)\frac{1}{e^{(\varepsilon-\mu)/k_B T}+1}d\varepsilon, \tag{2.8}$$

where k_B is the Boltzmann constant and $\mu \approx 1/2\,(\varepsilon_c + \varepsilon_v)$ is the chemical potential in intrinsic semiconductors that lies between the valence band and conduction band at low temperatures[40].

The previous discussion of semiconductors only considered the pure state of the material. These semiconductors are called intrinsic semiconductors. The electrical properties of semiconductors can be drastically changed by replacing atoms in the crystal lattice with heteroatoms. In the case of silicon, this is done by replacing silicon atoms with atoms from the groups VA or IIIA of the periodic table of elements. This process is called doping and leads to extrinsic semiconductors of n and p-type, respectively. The energy level of dopant atoms lies inside the bandgap near either the conduction or valence band. In the case of n-type semiconductors, the dopant is called a donor. The thermal excitation of the donor leads to an electron being excited into the conduction band and contributing to conduction. For p-type doping the energy level of the dopant lies near the energy of the valence band and can capture an electron through thermal excitation leaving behind a mobile hole in the valence band. This type of dopant is called an acceptor. The doping of semiconductors leads to a difference between the concentration of mobile electrons and holes. The charge carrier that is present in a higher concentration is called

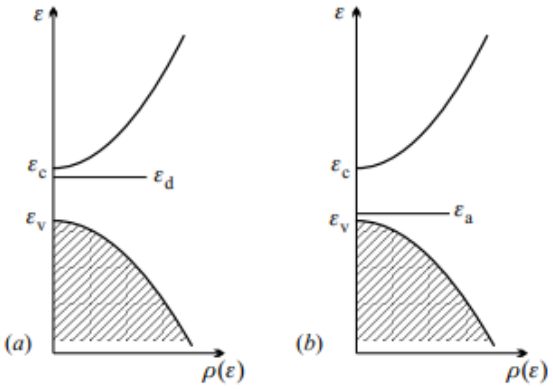

Figure 2.2: Energy levels of the acceptor and donor states in the band structure of semiconductors. From *Fundamentals of the physics of solids* by Jenő Sólyom[40].

the majority, the other type of carrier is called the minority charge carrier. It is important to note that despite the imbalance in the concentration of mobile charge carriers the charge neutrality of the semiconductor remains unchanged. The sum of the concentration of electrons in the conduction band and the concentration of ionized acceptors is equal to the sum of holes in the valence band and ionized donors. The energy levels of acceptors and donors in the bandgap are presented in Figure 2.2.

For doped semiconductors, the excitation of charge carriers has three distinct regions as the temperature increases. At low temperatures only the ionization of donors or acceptors takes place. This is the so-called freeze-out region. Once the temperature where all of the dopants are excited the charge carrier density of the material stays relatively unchanged as the temperature increases. This is caused by the temperature being inadequate for the thermal excitation from the valence to the conduction band. This is called the saturation range. Once the temperature reaches the level where thermal excitation is possible from the valence to the conduction band, the intrinsic range begins where charge carriers are excited through the bandgap. The change in chemical potential and the density of electrons in the conduction band as a function of temperature for an *n*-type semiconductor are shown in Figure 2.3.

2.1.2 Perovskite semiconductors

Metal halide perovskites are in the focus of scientific research[1, 41–45] due to their outstanding electrical and optical properties[1–3, 46] and easy, low-cost fabrication[47]. Their possible applications include solar cells[10], the detection of visible light[16, 17], X-rays[48], gamma rays[19], and neutrons[20], they can be used as gas sensors[15], light emitting diodes (LEDs)[5, 49], and lasers[6, 7]. Perovskites are proposed to be usable even in outer space[13, 14].

The perovskite crystal structure is named after the mineral called perovskite that corresponds to the $CaTiO_3$ formula. It was discovered by Gustav Rose in 1839 in the Ural mountains and named after Lev Alekseyevich von Perovski. Any material that has the ABX_3 crystal structure is referred to as a perovskite. In the following, the discussion focuses on organic-inorganic metal halide perovskites and inorganic metal halide perovskites.

The A component is a positive ion that can be either organic or inorganic. Organic cations

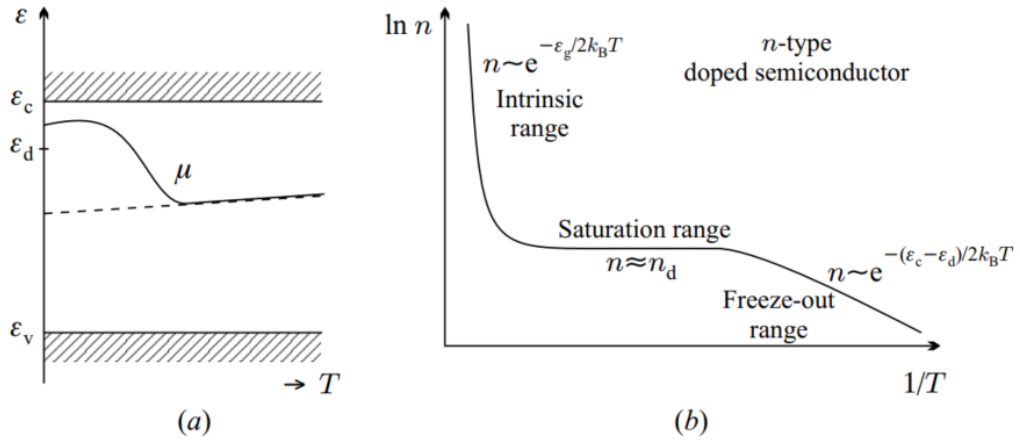

Figure 2.3: (a): Temperature dependence of the chemical potential and (b): temperature-dependent regions of charge carrier generation by thermal excitation. From *Fundamentals of the physics of solids* by Jenő Sólyom[40].

may be for example methylammonium (CH_3NH_3) or formamidinium ($NH_2CH{=}NH_2$) and the inorganic cations may be alkali metals such as cesium (Cs), rubidium (Rb) or potassium (K). The B component is a positive metal ion, usually lead (Pb) or tin (Sn). The X component is a negative ion of a halogen, that can be either iodide (I), bromide (Br), or chloride (Cl). The ABX_3 structure is presented in Figure 2.4. The structure is an octahedron formed by 6 halides in the corners and the metal ion in the middle. The organic or inorganic ions represented with A are surrounded by eight octahedra. The halide anions form covalent bonds with two metal cations and the organic or inorganic cation represented by A forms a bond with one of the halide ions. The symmetry of perovskites changes as a function of temperature. Starting from cryogenic conditions the materials first undergo a phase transition from orthorhombic to tetragonal that is followed by a phase transition from tetragonal to cubic.

There is a possibility of mixing the components of the perovskite thus realizing for example mixed halide perovskites. This is an important characteristic of the material group as this allows for the fine-tuning of the physical properties. By mixing the halide content between iodide, bromide, and chloride the electrical, optical, and magnetic properties of the material can be tuned between the values of the pure halide counterparts[4, 5]. This allows for example the growth of perovskite layers with the exact desired absorption edge for solar cell applications and the fine-tuning of the emission wavelength of an LED. In Figure 2.5. the change in the absorption and photoluminescence is shown as the halide content changes in the $CsPbX_3$ materials.

While the structure and general properties of organic-inorganic hybrid perovskites and fully inorganic perovskites are the same, there are important differences in their stability and robustness. The organic variants of metal halide perovskites are known to be more sensitive to degradation effects caused by temperature[52, 53], oxygen[54, 55], and moisture[56, 57], these processes are enhanced by illumination[58, 59]. The inorganic $CsPbBr_3$ counterpart is less sensitive to degradation[60]. There are possible solutions for this problem, such as the encapsulation of the device[61], the passivation of the perovskite layer[62]. While there are reports of point defects in all perovskites[63, 64], the methylammonium lead iodide perovskite is found to be less sensitive to defects than other perovskites[65].

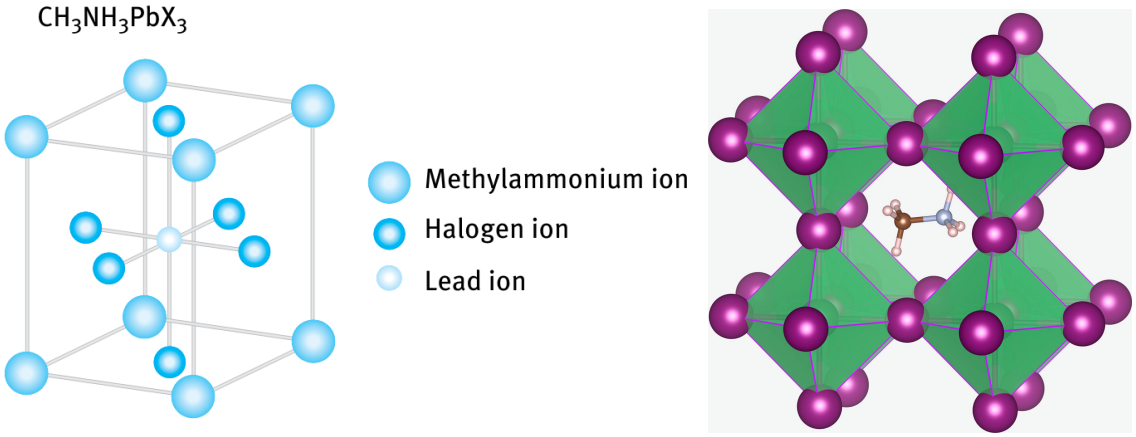

Figure 2.4: The crystal structure of methylammonium lead halide perovskites. The illustration on the left side presents one unit cell. From *Organic and Hybrid Solar Cells* by Lukas Schmidt-Mende, Stefan Kraner, and Azhar Fakharuddin[50]. The illustration on the right side presents the methylammonium group surrounded by eight octahedra of PbX_6. From *Ionic transport in hybrid lead iodide perovskite solar cells* by Christopher Eames *et al.*[51].

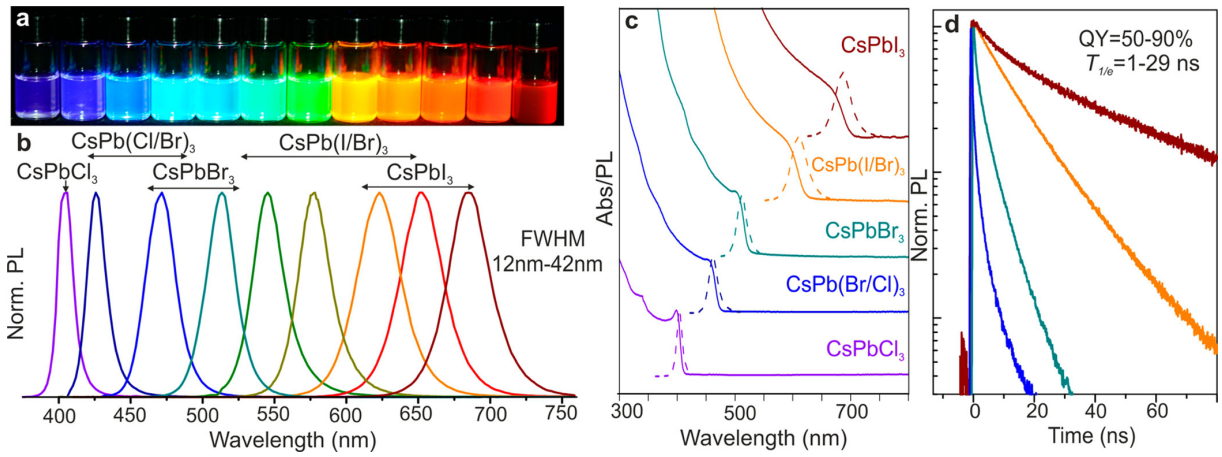

Figure 2.5: Subfigure (a) presents the colloidal form of the $CsPbX_3$ perovskites. In subfigure (b) the shift in the normalized photoluminescence is shown as the halide content changes. The absorption (solid lines) and photoluminescence (dashed lines) spectra are presented in subfigure (c) for samples with different halide content. Subfigure (d) shows the transient photoluminescent signal of the perovskites as the halide content changes. From *Nanocrystals of Cesium Lead Halide Perovskites ($CsPbX_3$, X = Cl, Br, and I): Novel Optoelectronic Materials Showing Bright Emission with Wide Color Gamut*, Loredana Protesescu *et al.*[5].

$\mathbf{MAPbX_3}$

The optical properties of pure halide versions of the methylammonium lead halide perovskites cover the visible spectrum[66]. The bandgap energy of $MAPbCl_3$, $MAPbBr_3$, and $MAPbI_3$ single crystals are 2.97 eV, 2.24 eV, and 1.53 eV, respectively[67]. The photoluminescent peak of the single crystals is found to be at 402 nm, 537 nm, and 784 nm for chloride, bromide, and iodide based methylammonium lead halides respectively. The bandgap of

methylammonium lead halides depends on the orientation of the methylammonium group in the perovskite structure. While the change is not huge, according to simulations the orientation of the methylammonium group leads to different bandgap energy values and may lead to a slightly indirect bandgap [68, 69].

The temperatures of the cubic↔tetragonal↔orthorhombic phase transitions of methylammonium lead halides are documented in the literature[70]. The $MAPbCl_3$ crystal has a space group of $Pm3m$ above 178.8 K, a space group of $P4/mmm$ in the $172.9 - 178.8$ K range, and a space group of $P222$ below 172.9 K. The $MAPbBr_3$ is in the space groups $Pm3m$ above 236.9 K, $I4/mcm$ between 155.1 K and 236.9 K, $P4/mmm$ in the $149.5 - 155.1$ K range, and $Pna2$ below 144.5 K, where the $149.5 - 236.9$ K regime has tetragonal symmetry with two different space group regions. The $MAPbI_3$ is cubic with a space group of $Pm3m$ above 327.4 K, tetragonal with a space group of $I4/mcm$ in the $162.2 - 327.4$ K range and has an orthorhombic symmetry with a space group if $Pna2$ below 162.2 K. The coexistence of domains of different phases around the phase transition temperatures has been observed before[71–73].

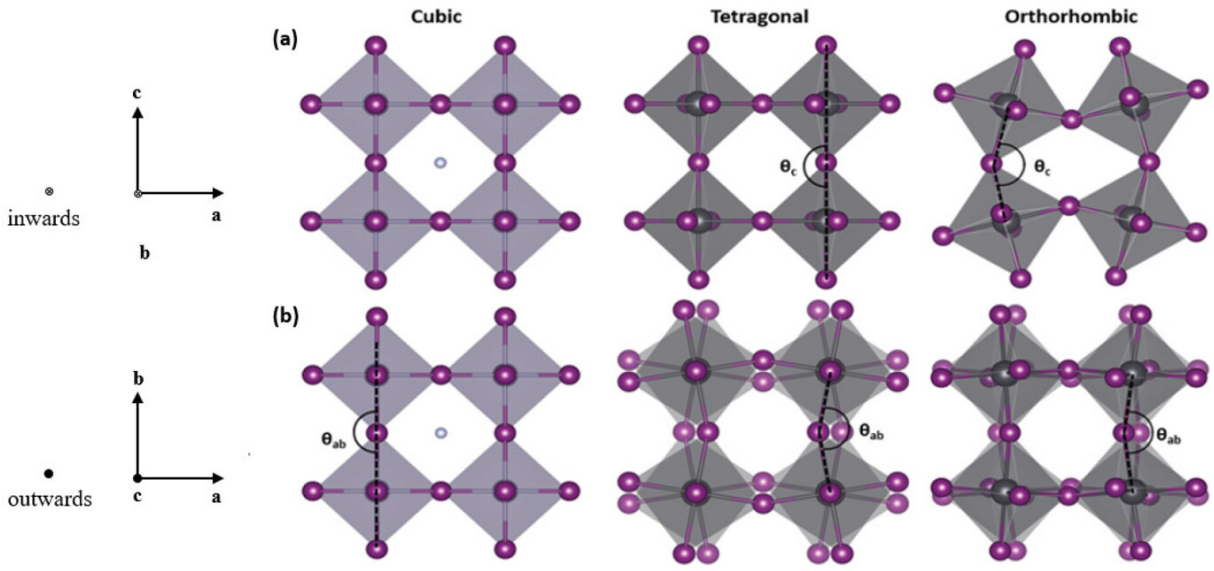

Figure 2.6: The structure of the cubic, tetragonal, and orthorhombic phases from two different viewpoints. The figure was made for tin-based perovskites. From *Tin Halide Perovskites: From Fundamental Properties to Solar Cells* by Matteo Pitaro *et al.*[74].

As the phase transitions occur in methylammonium lead halide perovskites the possible orientations of the methylammonium group in the structure are limited. In the cubic and tetragonal phases, the orientation of the MA cation changes between positions and has a high degree of freedom. As the temperature is decreased below the tetragonal to orthorhombic phase transition the methylammonium cation becomes fixed in one of two possible orientations along the axis of the unit cell. The dynamics of the methylammonium cation in the different phases and the fixed orientation of the cation in the orthorhombic phase are observed by measurements and simulations as well[75–79]. The orientation of the methylammonium cation highly influences the charge carrier dynamics in the orthorhombic phase. [80]

The ordering of the methylammonium group in the structure may lead to ferroelectric or antiferroelectric behavior[69, 80–82]. Experimental observations of ferroelectric domains have

been reported previously[83, 84]. The built-in electric field caused by the ferroelectric domains increases the separation of excited charge carriers leading to a higher charge-carrier lifetime and an increase in mobility[80].

$CsPbBr_3$

The cesium lead halide perovskites[85] are promising materials in the group of inorganic metal halide perovskites. While the chloride containing $CsPbX_3$ variant has a bandgap of 3 eV making it undesirable for photovoltaic applications[86] and the $CsPbI_3$ has a phase transition at room temperature that makes the material unstable and unusable as a solar cell material[87], the $CsPbBr_3$ has a direct bandgap located at ~ 2.16 eV making it ideal for photovoltaic applications[17]. It is also applicable as a scintillation detector[18]. The photoluminescent emission wavelength of $CsPbBr_3$ is 540 nm [5, 17], corresponding to ≈ 2.3 eV, and it is dependent on the preparation method and crystal size. The emission wavelength also depends on the temperature as multiple emission peaks can be observed at cryogenic conditions[5, 88–93]. It exhibits the orthorhombic symmetry below 361 K, tetragonal phase in the $361 - 403$ K range, and has cubic symmetry above 403 K[94]. This implies that it is in the orthorhombic phase during normal working conditions. The stability of $CsPbBr_3$ crystals in the presence of environmental effects is reported to be significantly better, than for methylammonium-based perovskites[60].

While the $CsPbBr_3$ perovskite has good photovoltaic and electrical properties despite the presence of traps[95], it is important to investigate the effect and presence of point defects and surface states. Thermally stimulated current measurements [64] and connected theoretical investigation [95] were conducted to investigate the possible point defects in the material. For multiple regions of a melt-grown sample, the concentration and activation energy were investigated and connected to the specific point defects possible in the $CsPbBr_3$ perovskite. The presence of surface states and defects at grain boundary trapping charge carriers were proposed in transient photoluminescence measurements[91, 96]. At low temperatures, the presence of trap states was observed through the emergence of additional photoluminescent peaks[90]. The presence of trap states was demonstrated by the comparison of transient photoluminescence and microwave photoconductivity decay measurements as well[97, 98].

One of the possible applications of perovskites is as tandem solar cells[99, 100]. Figure 2.7 presents a schematic diagram of a tandem solar cell that consists of $CsPbI_3$ and silicon as absorber layers. Tandem cells consist of multiple layers that absorb different portions of the electromagnetic spectrum. With this method, the efficiency of a single unit can be greatly increased. Tandem solar cells can be made in a manner that the two cells are two separate units stacked on top of each other or the two cells can be connected in series, with both methods having their advantages and disadvantages.

2.1.3 Wide bandgap semicondcutors

The semiconductor materials with a bandgap over 3.2 eV are commonly called wide-bandgap semiconductors[102]. Due to their unique electronic and optical properties, this subclass of semiconductors is an ideal choice for a wide range of applications, such as power electronics, LEDs, photodetectors, and thin-film transistors[30, 33, 103, 104]. Due to their wide

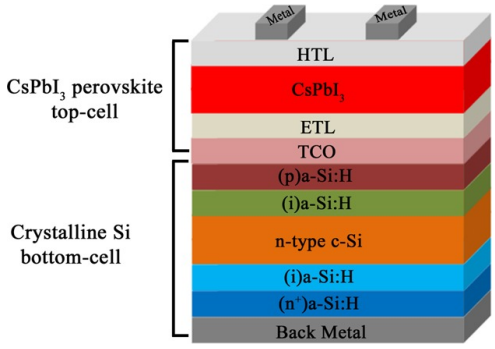

Figure 2.7: Schematic representation of a tandem solar cell. From *Inorganic $CsPbI_3$ Perovskite-Based Solar Cells: A Choice for a Tandem Device* by Waqar Ahmad *et al.* [101].

bandgap, the materials are ideal candidates for applications that require transparent components. The list of wide bandgap semiconductors includes diamond, silicon carbide, zinc oxide, indium oxide, gallium oxide, and indium gallium zinc oxide (IGZO)[102].

The first report of indium gallium zinc oxide in its crystalline form was in 1985 by Kimizuka and Mohri[105] but the material did not attract significant attention until the fabrication of thin film layers of single-crystalline[21] and amorphous[22] indium gallium zinc oxide by Nomura *et al.* in 2003 and 2004, respectively. The single crystalline thin film boasts a charge carrier mobility up to 80 cm^2/Vs but requires temperatures up to 1400°C during fabrication. The amorphous thin films can be fabricated at lower temperatures and can reach mobility values over 10 cm^2/Vs making it the preferred choice for thin-film transistor production. For comparison, the main thin-film transistor alternative hydrogenated amorphous silicon exhibits a mobility of ≈ 1 cm^2/Vs[106] and low-temperature polycrystalline silicon can reach mobility values in the $50-100$ cm^2/Vs range[107]. The amorphous IGZO thin films have a bandgap of 3.5 eV and the oxygen vacancies absorb light in the $400-550$ nm regime[108] making them essentially transparent in the visible regime. The amorphous IGZO thin films exhibit the percolation conduction effect over distributed potential barriers[109].

The first report of the five Ga_2O_3 polymorphs and their preparation method was reported in 1952[110], these being the α, β, γ, δ, and ε polymorphs. The β variant is the most stable with monoclinic structure followed by the ε with hexagonal and α polymorph with rhombohedral structure[111]. The α variant has the largest bandgap from all the polymorphs at $5.2-5.3$ eV[112, 113]. Due to its corundum structure, α-Ga_2O_3 thin films can be grown on sapphire with mist chemical vapor deposition[112, 113].

Persistent photoconductivity (PPC) is a known phenomena in IGZO[114–118] and Ga_2O_3[117, 119–122] thin films. The origin of the PPC effect in metal oxide semiconductors is still a matter of debate[123], but it is believed to be connected to oxygen vacancies in the material[124]. Oxygen vacancies can be created during the manufacturing process of the material or with deep UV illumination[124]. The oxygen vacancies act as donor states that can be ionized once or twice[123, 125] by optical excitation or by capturing holes drifting through the material[126]. The oxygen vacancy has a negative U behavior, meaning that the once positively charged vacancy has a less favorable energy than the neutral and twice ionized state. This leads to the neutral and twice ionized states being present in equilibrium and the, once ionized state emerging under illumination[124]. The holes are trapped at the oxygen vacancy site while electrons can move around freely. The PPC effect is believed to be caused by the decreased

probability of recombination due to the ionized oxygen vacancies leading to a prolonged relaxation process[127, 128]. The relaxation of the metastable twice ionized state to the neutral state is thermally activated[128].

2.2 Generation and recombination of charge carriers

The lifetime of excited charge carriers in semiconductors is a parameter of utmost importance. For solar cells the efficient excitation of charge carriers as a result of optical illumination is important but not enough, as the excited charge carriers only contribute to the fulfillment of humanity's insatiable hunger for energy if the charge carriers leave the solar cell without a recombination event. Since defects and contaminations decrease the lifetime of excited charge carriers the measurement of the recombination time is also an ideal method for the characterization of sample quality and purity.

The recombination process of electrons can occur through radiative recombination, Auger recombination, and the trap-assisted Shockley-Read-Hall (SRH) recombination processes[129–131]. The radiative, Auger, and SRH processes are depicted in Figure 2.8. We further distinguish the recombination processes that occur on the surface and in the bulk of the material. By including all of these the effective lifetime of charge carriers can be given as [132]

$$\frac{1}{\tau_c} = \left(\frac{1}{\tau_{SRH}} + \frac{1}{\tau_{Auger}} + \frac{1}{\tau_{rad.}} \right) + \frac{1}{\tau_{Surface}} = \frac{1}{\tau_{Bulk}} + \frac{1}{\tau_{Surface}}. \tag{2.9}$$

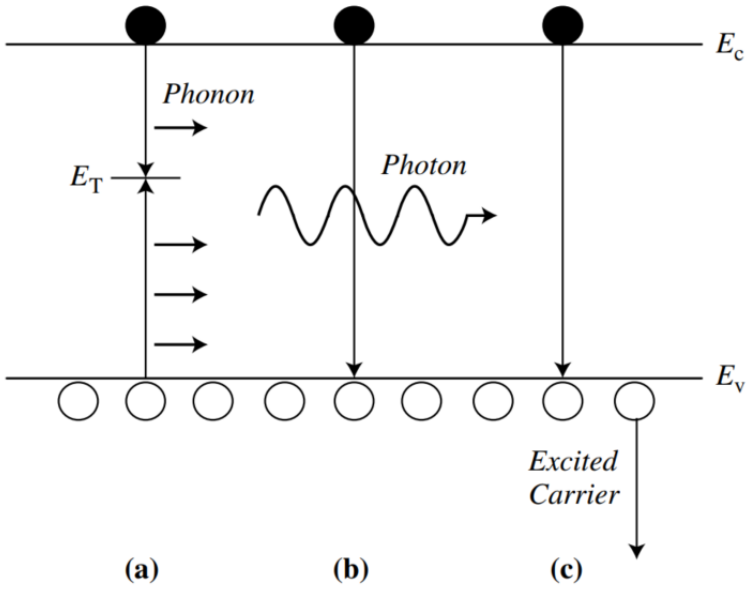

Figure 2.8: Schematic representation of the Shockley-Read-Hall, radiative, and Auger recombination process in subfigures (a), (b), and (c) respectively. From *Semiconductor Material and Device Characterization* by Dieter K. Schroder[133].

The recombination time of processes in the following will be calculated based on the connection between the recombination rate (U) and the change in excited charge carrier density as

a result of optical excitation (Δn) called the excess carrier density:

$$\frac{\partial \Delta n}{\partial t} = -U(\Delta n, n_0, p_0), \tag{2.10}$$

where n_0 and p_0 are the equilibrium carrier concentrations without optical excitation. From this, the recombination time can be obtained according to

$$\tau_c = -\frac{n(t)}{\frac{\partial n(t)}{\partial t}}, \tag{2.11}$$

as can be shown based on the rate equations. This leads to the lifetime as

$$\tau_c(\Delta n, n_0, p_0) = \frac{\Delta n}{U(\Delta n, n_0, p_0)}. \tag{2.12}$$

The lifetime based on the rate of each process can be calculated with this connection.

Radiative recombination is the process of an electron in the conduction band annihilating with a hole in the valence band while a photon with an energy of approximately the energy difference between the conduction and valence band is emitted. The rate of recombination for the radiative process is linearly proportional to the density of mobile charge carriers

$$U_{\text{rad}} = B\left(np - n_i^2\right) = B\left(n_0 + p_0 + \Delta n\right)\Delta n, \tag{2.13}$$

where $n = n_0 + \Delta n$ and $p = p_0 + \Delta p$ are the densities of mobile electrons and holes as a sum of thermally and optically excited carriers, $n_i^2 = n_0 p_0$, and B represents the quantum mechanical probability of the radiative transition. The recombination process is orders of magnitude more likely in direct semiconductors compared to semiconductors with indirect band structure, as the indirect transition requires the emission of a phonon as well. This leads to the radiative lifetime as[132, 133]

$$\tau_{\text{rad}} = \frac{1}{B\left(n_0 + p_0 + \Delta n\right)}. \tag{2.14}$$

The radiative lifetime can be regarded in low-level injection (LLI) and high-level injection (HLI) by assuming $\Delta n \ll n_0 + p_0$ and $\Delta n \gg n_0 + p_0$ respectively. The assumption is made that the trapping of charge carriers is low, leading to $\Delta n = \Delta p$. These assumptions lead to

$$\tau_{\text{rad}}^{\text{LLI}} = \frac{1}{B\left(n_0 + p_0\right)} \quad \text{and} \quad \tau_{\text{rad}}^{\text{HLI}} = \frac{1}{B\Delta n}. \tag{2.15}$$

The radiative recombination is thus shown to be independent of injection in the low injection limit and a constant value given by the doping level. According to the calculation, it is inversely proportional to the optically excited charge carrier density in the high injection limit.

The Auger recombination is a three-particle process where a mobile electron in the conduction band or hole in the valence band obtains the energy released by the recombination of an electron in the conduction band and hole in the valence band. This leads to different Auger coefficients (C_n and C_p) for the case when two electrons and a hole and when two holes and an electron take part in the process. The recombination rate of the Auger process is[132, 133]

$$U_{\text{Auger}} = C_n\left(n^2 p - n_0^2 p_0\right) + C_p\left(np^2 - n_0 p_0^2\right). \tag{2.16}$$

The Auger lifetime is thus

$$\tau_{\text{Auger}} = \frac{\Delta n}{C_n \left(n^2 p - n_0^2 p_0\right) + C_p \left(n p^2 - n_0 p_0^2\right)}. \tag{2.17}$$

The low and high-level injection limits can be calculated the same way as for the radiative recombination leading to[132]

$$\tau_{\text{Auger}}^{\text{LLI}} = \frac{1}{C_n N_D^2} \quad \text{for } n\text{-type and} \quad \tau_{\text{Auger}}^{\text{LLI}} = \frac{1}{C_p N_A^2} \quad \text{for } p\text{-type} \tag{2.18}$$

in the case of low injection limit and to

$$\tau_{\text{Auger}}^{\text{HLI}} = \frac{1}{(C_n + C_p)\,\Delta n^2} = \frac{1}{C_0 \Delta n^2} \tag{2.19}$$

in the case of high injection for both n and p-type semiconductors where $C_0 = C_n + C_p$ is the ambipolar Auger coefficient, N_D and N_A are the density of donors and acceptors.

The recombination time values in the low and high injection limits thus demonstrate that when the injection level is low, the recombination time is independent of the excess charge carrier density and is inversely proportional to the square of the doping concentration. In the case of high-level injection, the Auger lifetime is independent of the doping concentration and is inversely proportional to the excess charge carrier density squared.

For real processes, the model for the Auger recombination is more complex, the experimental results diverge from the model given above[132, 134]. This can be corrected by adding a Coulomb force to the model, thus creating the Coulomb-enhanced (CE) Auger recombination[132, 134].

If trap states are present in the forbidden region of the gap between the conduction and valence band the Shockley-Read-Hall recombination can take place. Defect levels in general can contribute to charge carrier dynamics with four processes. The defects can either emit or capture charge carriers and they can do so for both valence and conduction bands. This means the four processes are the emission of an electron into the conduction band, the capture of an electron from the conduction band, the emission of a hole into the valence band, and the capture of a hole from the valence band. The last two processes can be regarded as a capture and emission event of an electron as well. Depending on the position of the trap state in the bandgap the trap can be called a shallow or deep-level trap and the capture and emission coefficients of the processes change vastly. The SRH recombination takes place when an electron in the conduction band and a hole in the valence band recombine through a deep-level trap as a result of their subsequent capture.

The recombination rate for the SRH process is [132]

$$U_{\text{SRH}} = \frac{np - n_i^2}{\tau_{n0}\left(p + p_{\text{I}}\right) + \tau_{p0}\left(n + n_{\text{I}}\right)}, \tag{2.20}$$

where τ_{p0} and τ_{n0} are the capture time constants of electrons and holes, n_{I} and p_{I} are the so-called SRH densities. The capture time constants are given as $\tau_{p0} = \left(N_t \sigma_p \nu_{th}\right)^{-1}$ and $\tau_{n0} = \left(N_t \sigma_n \nu_{th}\right)^{-1}$, where σ_n and σ_p are the capture cross-sections, ν_{th} is the thermal velocity, and N_t is the density of trap states. This leads to the SRH lifetime in the form [132, 133]

$$\tau_{\mathrm{SRH}} = \frac{\tau_{n0}\left(p_0 + p_I + \Delta n\right) + \tau_{p0}\left(n_0 + n_I + \Delta n\right)}{p_0 + n_0 + \Delta n}. \tag{2.21}$$

The SRH lifetime in the high and low injection limit is thus[132]

$$\tau_{\mathrm{SRH}}^{\mathrm{HLI}} = \tau_{n0} + \tau_{p0} = \tau_{n0}\left(1 + k\right) \quad \text{and} \quad \tau_{\mathrm{SRH}}^{\mathrm{LLI}} = \tau_{n0}\left[\frac{p_0 + n_I}{p_0 + n_0} + k\frac{n_0 + n_I}{p_0 + n_0}\right], \tag{2.22}$$

where k is the symmetry factor given as $k = \sigma_n/\sigma_p = \tau_{p0}/\tau_{n0}$. The low-level injection case can be further divided into n and p-type cases by substituting $n_0 = 0$ and $p_0 = 0$ into the relation.

The SRH recombination time is a constant value in both low and high injection levels but the two values are different. The recombination time is determined by the time constant of the capture events in the high injection regime and the time constant, doping level, and SRH densities in the low injection limit. This means, that the SRH recombination time is represented by two different constant values at high and low injection limits with a changing tendency between the two limits.

The radiative, Auger, and SRH lifetimes are presented in Figure 2.9. as a function of injection density in silicon. The graph is a recolored version[2] of the same figure presented in *Untersuchungen zur Ladungsträgerlebensdauer in kristallinem Silizium für Solarzellen* by Kevin Lauer[135]. The general tendencies discussed previously in the text are observable. The low-level injection regime presents constant lifetime values for all three processes while the high-level injection regime is according to the linear and quadratic Δn tendency discussed before for the radiative and Auger process and constant for the Shockley-Read-Hall recombination.

The distinction between bulk and surface recombination with the SRH processes is important because of the vastly different nature of defects on the surface and in the bulk of a material. In the bulk, the recombination centers are imperfections in the crystal structure or impurities, for example, grain boundaries or point defects. On the sample surface, the sudden end of the crystal structure results in partially bonded atoms. These dangling bonds provide the defect levels for the SRH process[132]. The surface recombination time depends on the surface recombination velocity (S), sample thickness (W), and the diffusion constant (D) and has two possible values depending on whether the surface is well-passivated or not. The two cases are given as[132, 136]

$$\tau_{\mathrm{S}} = \frac{W}{2S} \quad \text{if} \quad \frac{SW}{D} < \frac{1}{4} \tag{2.23}$$

and

$$\tau_{\mathrm{S}} = \frac{W^2}{D\pi^2} \quad \text{if} \quad \frac{SW}{D} > 100, \tag{2.24}$$

meaning that if the surface is well passivated the surface recombination lifetime is big and the effective lifetime is determined by the bulk lifetime. However, if the surface recombination velocity is high the effective lifetime will be determined by the surface and bulk recombination processes. If the bulk lifetime and diffusion constant are high enough the recombination process may happen only on the sample surface. In this case, the sample thickness can be determined

[2]The recolored version was presented by the author at *Workshop on Test Methods for Silicon Feedstock Materials, Bricks and Wafers, München, 14. 6. 2012*.

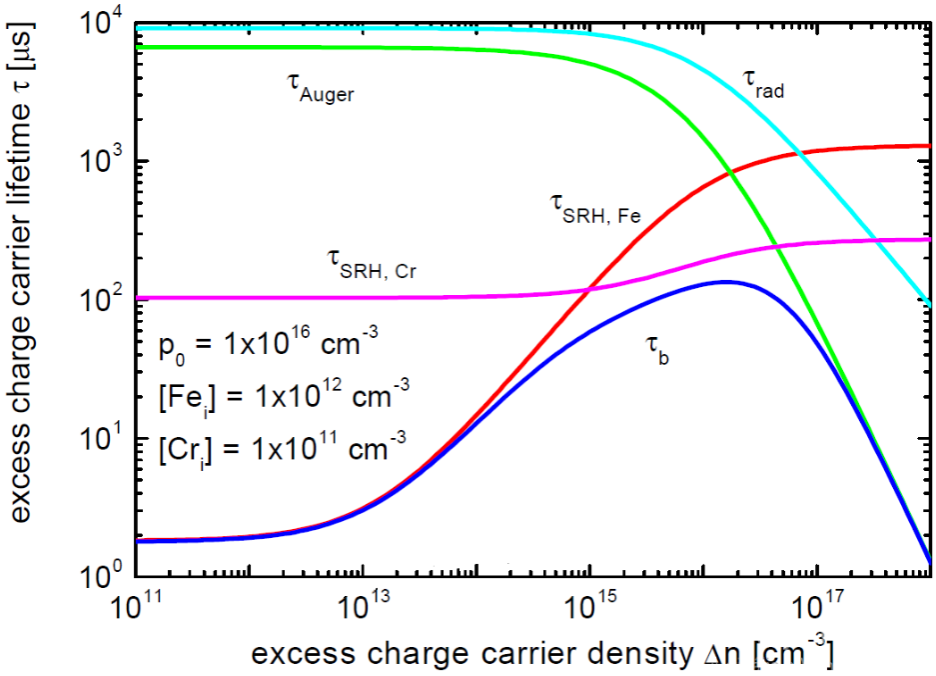

Figure 2.9: Injection-dependent lifetime for the Auger, SRH, and radiative recombination processes. The bulk lifetime is presented as well. The SRH process is shown for two different defects. From *Untersuchungen zur Ladungsträgerlebensdauer in kristallinem Silizium für Solarzellen* By Kevin Lauer [135].

from the recombination time and diffusion constant or the diffusion constant can be determined from the measurement of charge-carrier lifetime and sample thickness.

In applications where the surface recombination limits the device efficiency, for example, solar cell applications[137], the surface recombination velocity can be decreased by passivation. This passivation prevents the dangling bonds of the outer layer from acting as defect levels for the SRH process. The passivation can be done by several approaches, including chemical methods and the growth or deposition of a passivation layer[137, 138]. Figure 2.10. from *Semiconductor Material and Device Characterization* by Dieter K. Schroder[133] presents the dangling bonds on the surface of two silicon wafers with different orientations.

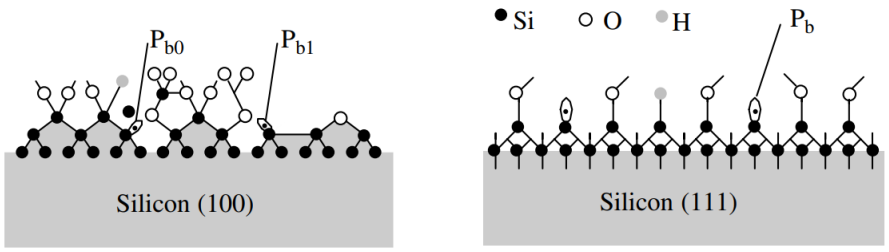

Figure 2.10: Dangling bonds on the surface of silicon wafers. P_1, P_b, and P_{b0} are the designations of the dangling bonds. From *Semiconductor Material and Device Characterization* by Dieter K. Schroder[133].

In Figure 2.11. from *Semiconductor Material and Device Characterization* by Dieter K.

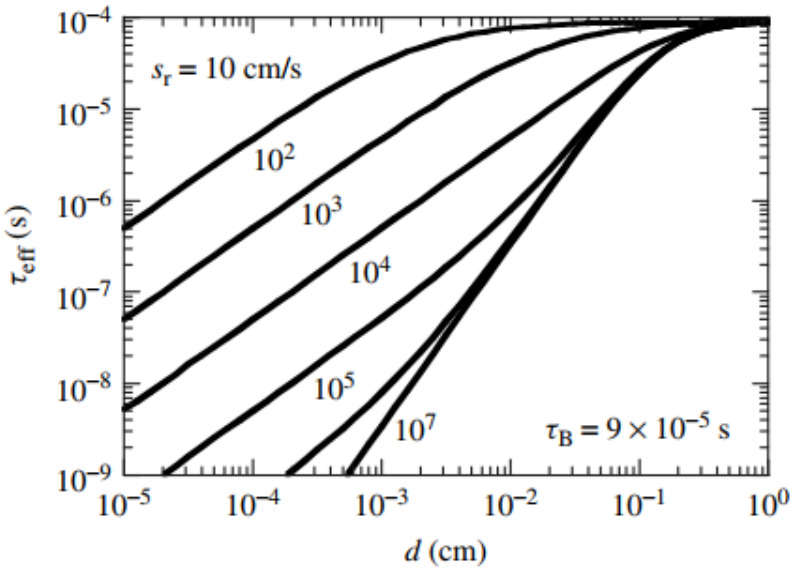

Figure 2.11: The effective lifetime of charge carriers (τ_{eff} in the figure) as a function of wafer thickness (d) for multiple surface recombination velocity (s_r) values. From *Semiconductor Material and Device Characterization* by Dieter K. Schroder[133].

Schroder[133] the effective lifetime is presented as the function of sample thickness for different surface recombination velocities. The effective lifetime decreases significantly as the surface recombination velocity increases. This presents the importance of surface passivation, as the passivation of the surface decreases the surface recombination velocity.

The measurement of charge-carrier recombination can be done through multiple methods and the measurement results may differ between these methods[133]. This is because of the different parameters measured by different methods, leading to the techniques being complementary to each other. For example, in microwave photoconductivity techniques the conductivity is measured that is in direct connection with the concentration of mobile charge carriers. While this method provides the effective charge-carrier lifetime it can not differentiate between holes and electrons. Transient photoluminescence measurements provide the radiative recombination time exclusively during the recombination process. This leads to the complementary measurement of transient photoluminescence and microwave photoconductivity that help with the disentanglement of radiative and nonradiative recombination processes. Both transient photoluminescence[91–93, 139, 140] and transient microwave photoconductivity[97, 141–144] measurements are used in the research of metal halide perovskites.

2.3 Detection of photoexcited charge carriers

The experimental method and simulations presented in this section are based on my publications presenting measurement results with the systems and the system itself. The article detailing the cavity-based measurement is titled *Ultralong Charge Carrier Recombination Time in Methylammonium Lead Halide Perovskites*[O1]. The articles presenting the CPW-based experimental setup are titled *Millisecond-Scale Charge-Carrier Recombination Dynamics in the*

CsPbBr3 Perovskite[O2] and *Time-resolved photoconductivity decay measurements with broadband radiofrequency detection and excitation energy*[O3].

The microwave photoconductivity measurement is a nondestructive noncontact measurement of the change in the conductivity of a given material as a result of optical excitation. The method determines the recombination time of photoexcited charge carriers in semiconductors. If optical excitation is applied to a semiconductor, charge carriers are excited in the material from the valence band to the conduction band. The change in mobile charge-carrier concentration leads to the change of conductivity[40]. The measurement of conductivity with microwaves is based on the probing of the sample with microwave radiation. There are two approaches to the detection of change in microwave reflection, transmission, and absorption: either an antenna or waveguide[145] is used for the emission and detection of the probing radiation, or the sample is placed inside a microwave cavity[146, 147]. In the case of a waveguide-based setup, the sample is probed with microwave radiation and either the reflected or transmitted microwave signal is measured[148, 149]. Since the reflected and transmitted microwave signal is proportional to the conductivity of the sample, the measurement of the change in conductivity can be measured through the change in transmitted or reflected microwave signal. In the case of a cavity-based measurement method, the sample is placed inside a microwave cavity and the photoexcitation of the sample changes the resonance frequency and quality factor of the cavity. The shift in these two parameters is connected to the change in the conductivity of the sample. It is generally assumed that the connection between the change in sample conductivity and the change in the microwave reflection is linear[148–151]. By measuring the change in conductivity the change in charge carrier density can be observed leading to the measurement of charge-carrier recombination time. Both methods have advantages and disadvantages: the cavity-based approach is more sensitive but limited in bandwidth whereas the antenna-based method is essentially high-speed but often lacks sensitivity. The latter method has the added benefit that it can be adapted to most sample geometries whereas the sample needs to be placed inside the cavity for the earlier technique.

2.3.1 Measuring charge carrier density through the surface impedance

To show the connection between microwave reflection and conductivity the surface impedance, Z_S, should be first taken into account. The surface impedance of a sample is [152, 153]:

$$Z_S = \sqrt{\frac{i\omega\mu}{\sigma + i\omega\varepsilon}}, \tag{2.25}$$

where $\mu = \mu_0\mu_r$ is the sample permeability with μ_0 representing the vacuum permeability, σ is the sample conductivity, and $\varepsilon = \varepsilon_0\varepsilon_r$ is the sample permittivity with ε_0 representing the dielectric constant.

There are two special cases for the surface impedance, which are the low conductivity and high conductivity limits. Depending on the relation between σ and the $i\omega\varepsilon$ product, one of these two may be simplified. In the low conductivity limit ($\sigma \ll \omega\varepsilon$) the simplification leads to $Z_S = \sqrt{\frac{i\omega\mu}{i\omega\varepsilon}} = \sqrt{\frac{\mu}{\varepsilon}}$. In the high conductivity limit ($\sigma \gg \omega\varepsilon$) the simplification gives $Z_S = \sqrt{\frac{i\omega\mu}{\sigma}} = \frac{1+i}{2}\mu\omega\delta$ where $\delta = \sqrt{\frac{2}{\mu\omega\sigma}}$ is the penetration depth of the microwave radiation into

the probed sample. A simulation of the real and imaginary part of the surface impedance is shown in Figure 2.12. The simulation presents two different probing frequencies. The change in probing frequency shifts the real and imaginary part of the surface impedance along the x axis, meaning a shift in the resistivity region where significant change is observed in the surface impedance.

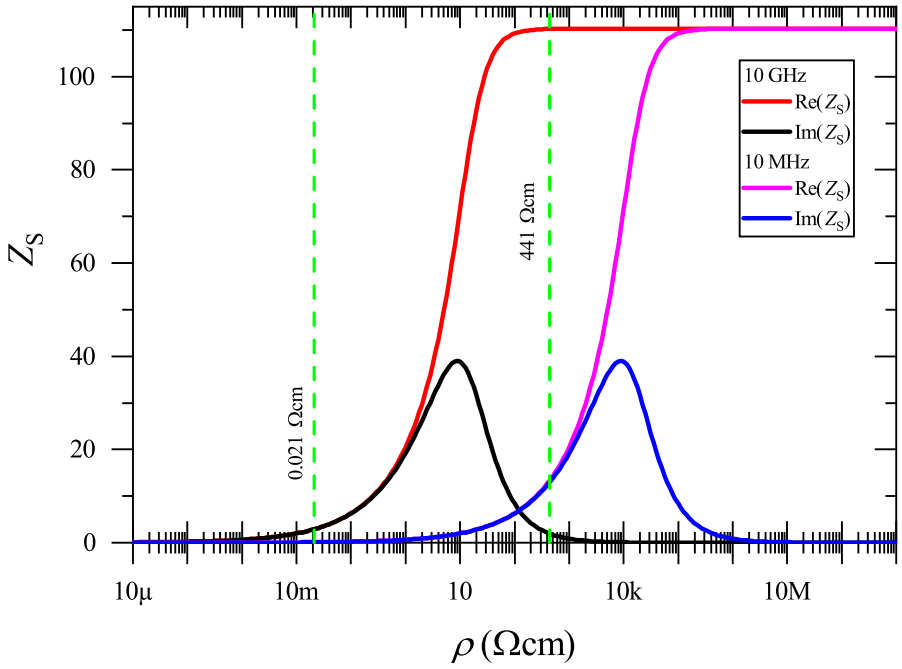

Figure 2.12: Simulation of the surface impedance as a function of resistivity for two frequencies. The real and imaginary parts of the surface impedance are both shown in the graph. The green dotted line presents two typical values for low and highly-doped silicon.

The surface impedance exerts different effects in the case of cavity and waveguide-based measurements. The perturbation caused by the placement of a sample with surface impedance Z_S on the surface of a coplanar waveguide is $Z_{\text{perturbed}} = \eta Z_S$[153, 154], where η is a filling factor dependent on sample geometry and the coverage of the coplanar waveguide. The perturbation causes a reflection of the microwave signal. The reflection coefficient denoted by Γ represents the quotient of the probing and reflected microwave voltages, U_{probing} and $U_{\text{reflected}}$. If there is no transmitted microwave radiation, the reflection coefficient is as follows[152]:

$$\Gamma = \frac{U_{\text{reflected}}}{U_{\text{probing}}} = \frac{Z_{\text{perturbed}} - Z_0}{Z_{\text{perturbed}} + Z_0}. \tag{2.26}$$

The Z_0 component in Equation 2.26 is the wave impedance of the coplanar waveguide. The value of Z_0 is further discussed later in the text. If there is also a transmission of microwave power, the equation of the reflection coefficient presented in Equation 2.26. is slightly modified[152]. In the following, I assume the transmission to be zero. A simulation of the reflection coefficient is shown in Figure 2.13. There are five curves in the figure. The absolute value of the reflection coefficient, which gives the reflected microwave signal as a function of resistivity, the imaginary and real part of the reflection coefficient, and the two special cases of low and high conductivity limits. The general solution of the reflection coefficient falls in line

with the low conductivity limit case at high resistance values and with the high conductivity limit case at low resistances, as expected.

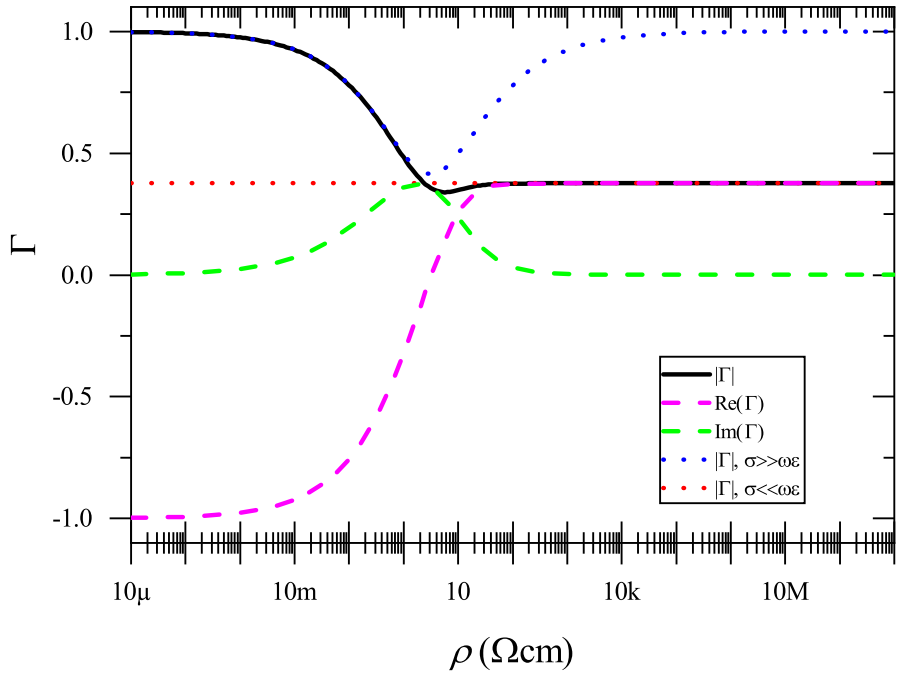

Figure 2.13: Simulation of the reflection coefficient for the general, low conductivity, and high conductivity cases. The figure includes the real and imaginary part of the reflection coefficient besides its amplitude as well. The low and high conductivity cases fall on the general case at their respective regions. Note that the engineering notation is used for the horizontal scale.

The reflection coefficient as a function of resistivity is shown in Figure 2.14. for four different probing frequencies. The monotonous regime of the reflection coefficient shifts in resistivity as the probing frequency changes. The probing frequency should always be chosen in a manner, that the reflection coefficient is monotonous in the studied range of resistivity.

The connection between the conductivity of the sample and the reflected voltage is generally assumed to be linear[148–151]. The previous discussion showed, that this is true for a broad range of conductivity values and that by carefully selecting the probing frequency the linearity holds for the sample under investigation. To connect the conductivity with the charge carrier density one has to take into consideration the Drude model[39, 40]:

$$\sigma = \frac{n_e e^2 \tau}{m_e^*} = n_e e \mu_e, \tag{2.27}$$

where e is the elementary charge, n_e is the density of electrons, τ is the momentum scattering time, m_e^* is the effective electron mass, and μ_e is the electron mobility. This equation holds for a single carrier model, but it can be expanded to electrons and holes as well. This is an important additional step since the microwave photoconductivity measurement does not differentiate between electrons and holes and detects all mobile charge carriers. The two-band model for conductivity results in[40]:

$$\sigma = n_e e \mu_e + n_h e \mu_h, \tag{2.28}$$

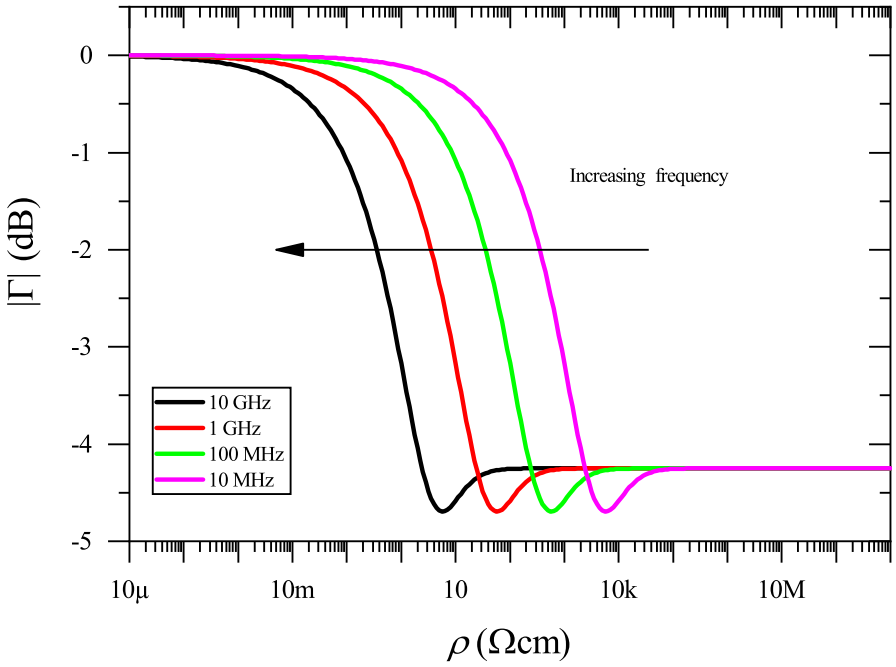

Figure 2.14: Simulation of the reflection coefficient for multiple different probing frequency values. A shift can be observed in the reflection coefficient towards lower conductivity values as the frequency of the probing microwave signal increases.

where n_h is the density and μ_h is the mobility of holes. In the following, I use the single carrier model for the calculations. The same can be shown for two carriers.

The connection between conductivity and the reflection coefficient can be further discussed by calculating the Taylor series of the surface impedance and reflection coefficient for small conductivity changes:

$$Z_\mathrm{S}(\sigma_0+\Delta\sigma) \approx Z_\mathrm{S}(\sigma_0)\cdot\left(1-\frac{\Delta\sigma}{2(\mathrm{i}\omega\varepsilon+\sigma_0)}\right), \tag{2.29}$$

$$\Gamma(\sigma_0+\Delta\sigma) \approx \Gamma_0\left(1-\frac{Z_0\cdot Z_\mathrm{S}(\sigma_0)}{Z_\mathrm{S}(\sigma_0)^2-Z_0^2}\cdot\frac{\Delta\sigma}{\mathrm{i}\omega\varepsilon+\sigma_0}\right). \tag{2.30}$$

If we consider $Z_\mathrm{S}(\sigma_0+\Delta\sigma) = Z_\mathrm{S}+\Delta Z_\mathrm{S}$, then this leads to the change in the surface impedance being linear with the change in conductivity:

$$\Delta Z_\mathrm{S} \approx Z_\mathrm{S}(\sigma_0)\left(-\frac{\Delta\sigma}{2(\mathrm{i}\omega\varepsilon+\sigma_0)}\right) \propto \Delta\sigma \propto \Delta n. \tag{2.31}$$

The same can be shown for the reflection coefficient, as $\Gamma(\sigma_0+\Delta\sigma) = \Gamma+\Delta\Gamma$ leads to:

$$\Delta\Gamma \approx \Gamma_0\left(-\frac{Z_0\cdot Z_\mathrm{S}(\sigma_0)}{Z_\mathrm{S}(\sigma_0)^2-Z_0^2}\cdot\frac{\Delta\sigma}{\mathrm{i}\omega\varepsilon+\sigma_0}\right) \propto \Delta\sigma \propto \Delta n, \tag{2.32}$$

since all other values beside $\Delta\sigma$ are unaffected by the change in charge carrier density in the formulas of ΔZ_S and $\Delta\Gamma$.

If instead of being placed on top of a waveguide, a sample is placed into a cavity with a quality factor of Q and resonant frequency of f_0, and filling factor η, the change caused by the presence of the sample is as follows[155, 156]:

$$\frac{\Delta f}{f_0} + i\Delta\left(\frac{1}{2Q}\right) = i\eta Z_S. \tag{2.33}$$

Since the cavity-based experimental system is equipped with an automatic frequency control system, the change in resonance frequency can be neglected. This shows, that the change in the surface impedance of the sample has a linear connection to the $\Delta\left(\frac{1}{2Q}\right)$ output of the system. Since the connection between the surface impedance and charge carrier density is linear according to the previous calculations, this shows that the change in the output of the experimental setup is proportional to the change in charge carrier density.

2.3.2 Transient and steady-state methods for the measurement of charge carrier density

The photoexcitation of a material with a light source of proper wavelength leads to the excitation of electrons from the valence band to the conduction band leaving behind holes in the valence band. These charge carriers can freely move in the material, increasing the conductivity of the semiconductor. Since the connection of conductivity and charge carrier density is linear, the measurement of photoinduced change in sample conductivity leads to the observation of the photoinduced change in charge carrier density.

The photogenerated change in charge carrier density leads to two possible measurements. Either a pulsed excitation or a continuous wave excitation is used. In the case of pulsed excitation, the decay of the microwave signal is proportional to the decay of charge carrier density through the connection to conductivity. This leads to the measurement of the charge carrier recombination process through the observation of the transient microwave photoconductivity decay (TRMCD) signal. By analyzing the transient photoconductivity decay curves, the recombination time of charge carriers can be extracted. The continuous wave (CW) excitation is based on the emergence of steady-state conductivity levels at different photoexcitation levels due to the balance between the charge carrier generation rate caused by photoexcitation and the recombination rate of charge carriers. By comparing two or more steady-state levels the difference between them can be used to obtain information on the charge carrier density and charge-carrier recombination time. It is also possible to combine the two methods by using the quasi-steady-state approach [157–159].

These connections can be shown by the simple analysis of the rate equations governing these processes. The rate equations give the change of charge carrier density, $\frac{dn}{dt}$, as a function of charge carrier density, n, charge-carrier recombination time or charge-carrier lifetime, τ_c, and charge carrier generation rate, G_{photo}. The rate equation is[133]:

$$\frac{dn}{dt} = -\frac{n}{\tau_c} + G_{photo}. \tag{2.34}$$

The differential equation can be solved for two different cases: pulsed and CW measurements. In the case of a CW measurement, the recombination and generation rates establish a

balance and a steady state emerges. This means, that the change in carrier density is zero, and the steady-state condition leads to the following:

$$n = G_{\text{photo}} \cdot \tau_{\text{c}}. \tag{2.35}$$

If multiple different generation rates are used, this allows for the measurement of the product of the generation rate and recombination time. Since the measured microwave voltage is proportional to the charge carrier density, by measuring the steady-state signal with the same excitation over a wide temperature range the product of generation rate and recombination time can be obtained. This carries information about the change in material properties.

In the case of a pulsed excitation, the general solution for the rate equation is:

$$n(t) = k \cdot e^{-t/\tau_{\text{c}}} + G_{\text{photo}} \cdot \tau_{\text{c}}, \tag{2.36}$$

where k is a constant. If we assume, that no charge carriers are excited before the pulse ($n(t = 0) = 0$), the rate equation is only be fulfilled if k is determined in the following way:

$$n(t) = G_{\text{photo}} \cdot \tau_{\text{c}}(1 - e^{-t/\tau_{\text{c}}}). \tag{2.37}$$

One can make the assumption, that the charge-carrier recombination time is significantly longer than the pulse width. In this case, the assumption can be made that there is no recombination process during the excitation. This is supported by the consideration, that if the recombination time is shorter than the pulse duration the change in conductivity is small since the process does not result in a high excited charge carrier density. If no recombination process happens during the pulse, then the charge carrier density following the pulse is the product of the generation rate and the pulse width of the exciting laser pulse, t_{pulse}. This is supported by calculating the Taylor series of $e^{-t/\tau_{\text{c}}}$ around $t = 0$, which gives $e^{-t/\tau_{\text{c}}} \approx 1 - \frac{t}{\tau_{\text{c}}} + \frac{t^2}{2\tau_{\text{c}}^2} - ...$[160]. By substituting the value obtained with the Taylor series into the rate equation and considering that $t \ll \tau_{\text{c}}$, we reach the aforementioned conclusion for the generated charge carrier density during the laser pulse:

$$n = G_{\text{pulse}} \cdot t_{\text{pulse}}. \tag{2.38}$$

The rate equation can be solved for the relaxation process as well. This is an easy task, since the generation rate is zero during the recombination process, leading to

$$\frac{\mathrm{d}n}{\mathrm{d}t} = -\frac{n}{\tau_{\text{c}}}, \tag{2.39}$$

which can be easily solved. The solution for the differential equation results in an exponential decay of charge carrier density with the characteristic time of the charge-carrier lifetime starting from the initial population obtained during excitation, $n_0 = G_{\text{pulse}} \cdot t_{\text{pulse}}$:

$$n(t) = n_0 \cdot e^{-\frac{t}{\tau_{\text{c}}}}. \tag{2.40}$$

This result leads to the conclusion that by fitting the time-resolved microwave photoconductivity decay curves during the relaxation process of the excited charge carriers one can obtain the charge-carrier recombination time. This simple consideration is made more complicated by the previously presented recombination dynamics through the Auger, radiative, and SRH recombination processes, as the charge-carrier recombination time changes as a function of charge carrier density[159, 161] during the recombination process.

2.3.3 Charge carrier density dependent recombination time measurement

If the recombination time changes as a function of charge carrier density as shown in Figure 2.9., then it also changes during the recombination process as the excited charge carrier density changes as a function of time. In such cases, the apparent charge-carrier recombination time can be evaluated using the time-dependent photoconductivity signal[150, 162]. Regarding the rate equation in the previous section, the connection between excess charge carrier density, its derivative, and the recombination time during the relaxation process can be given in the following form[133]:

$$\tau_c = -\frac{n(t)}{\frac{\partial n(t)}{\partial t}}. \tag{2.41}$$

If the connection between the charge carrier density and microwave photoconductivity signal, $U(t)$ is linear, then this can be written as:

$$\tau_c = -\frac{U(t)}{\frac{\partial U(t)}{\partial t}}. \tag{2.42}$$

Thus it is possible to evaluate the charge-carrier recombination time as a function of microwave signal, which is proportional to the charge carrier density. This allows for the evaluation of $\tau_c(t)$ or $\tau_c(U)$ tendencies, the latter being representative of the recombination time as the charge carrier density relaxes. This is the theoretical basis behind the method used in Chapter 5. If a trapping mechanism dominates the charge carrier recombination dynamics, the recombination time observed during the measurement process is usually not called the charge-carrier lifetime, since the characteristic time that is measured in these cases is dominated by the de-trapping of charge carriers and not the SRH, Auger, or radiative recombination.

2.4 Transport properties of multiband charge carriers

The Hall effect measurement is a widely used method for the characterization of electronic materials. The Hall effect measurement can uncover the majority charge carrier density and mobility of the material, while the van der Pauw method provides the resistivity of the material. These two measurements are crucial for the characterization of new materials and manufacturing methods in the semiconductor and solar cell industry as well as the scientific community. These measurements are based on simple transport measurements yet uncover important material information.

2.4.1 The van der Pauw method for sheet resistance measurement

The resistivity of a material can be calculated from the sheet resistance and the thickness of the sample as $\rho = R_S \cdot t$, where t is the thickness of the sample and R_S is the sheet resistance. The sheet resistance can be measured either with two or four point method, with four point methods being more accurate. With a four point probe method, two of the probes are responsible for flowing a current through two points of the sample while two additional points are used for the

measurement of potential difference. This measurement is conducted without a magnetic field, the magnetic field perpendicular to the sample surface is set to $B_z = 0$.

The van der Pauw measurement method[163] provides a reliable sheet resistance measurement for arbitrary sample shapes as long as the measurement conditions are fulfilled. The conditions for a flat sample are[163] (1) the contacts should be at the circumference of the sample, (2) the contacts should be sufficiently small, (3) the sample thickness is constant, and (4) the sample should not have any isolated holes. If the contacts on the sample surface do not fulfill these requirements the measurement accuracy is decreased. The most ideal geometry is the so-called clover-shaped geometry presented in subfigure (b) of Figure 2.15., but multiple other geometries are used as well, such as the Greek cross and the square shape. A few examples are presented in Figure 2.15[133].

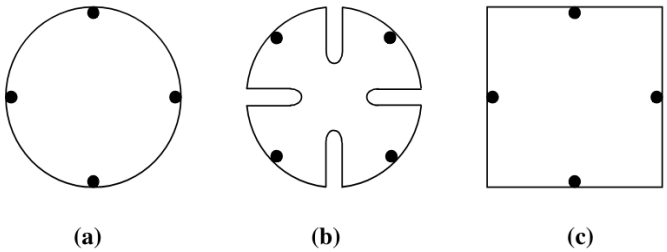

Figure 2.15: Possible contact realization on the sample surface for the van der Pauw sheet resistance measurement. The image is taken from *Semiconductor Material and Device Characterization* by Dieter K. Schroder[133].

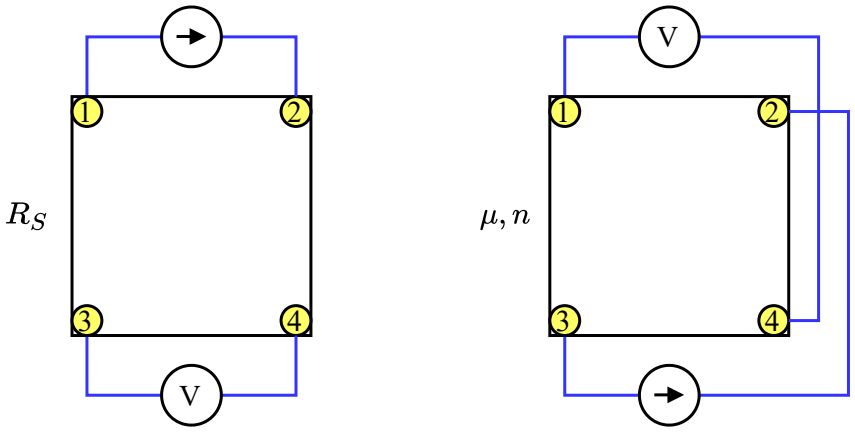

Figure 2.16: Schematic drawing of the contacts for the sheet resistance measurement on the left side and the Hall effect measurement on the right side.

The measurement of sheet resistance comprises the measurement of the potential along one edge of the sample while a current flows along another edge of the sample, as shown in Figure 2.16. The measured resistance values are defined as

$$R_{12,34} = \frac{V_{34}}{I_{12}}, \tag{2.43}$$

where I_{12} is the current flowing from contact 1 towards contact 2 and V_{34} is the potential difference between contact 3 and contact 4. For the measurement of sheet resistance, at least two resistance values are needed, these are the $R_{12,34}$ and $R_{23,41}$. With these values, the sheet resistance can be calculated by solving the following equation[163]:

$$e^{-\frac{\pi R_{12,34}}{R_S}} + e^{-\frac{\pi R_{23,41}}{R_S}} = 1. \tag{2.44}$$

This equation can be obtained by regarding the potential difference between two points resulting from a current flowing between two other points in the case of a simple geometry and then showing, that the relation holds for any shape[163]. From Equation 2.44 the resistivity can be calculated if the sample thickness is known as

$$e^{-\frac{\pi R_{12,34} t}{\rho}} + e^{-\frac{\pi R_{23,41} t}{\rho}} = 1. \tag{2.45}$$

The equation can be solved in the following way[163]

$$\rho = \frac{\pi t}{\ln 2} \frac{R_{12,34} + R_{23,41}}{2} \cdot f\left(\frac{R_{12,34}}{R_{23,41}}\right), \tag{2.46}$$

where f is a function of the ratio of the measured resistance values that fulfill the following relation[163]:

$$\frac{R_{12,34} - R_{23,41}}{R_{12,34} + R_{23,41}} = f \cdot \operatorname{arccosh}\left(\frac{e^{\frac{ln(2)}{f}}}{2}\right). \tag{2.47}$$

If the measured resistance values are almost equal, then the f function can be transformed into an approximated form where the value of it is close to one. In these cases[163]

$$f \approx 1 - \left(\frac{R_{12,34} - R_{23,41}}{R_{12,34} + R_{23,41}}\right)^2 \frac{\ln 2}{2} - \left(\frac{R_{12,34} - R_{23,41}}{R_{12,34} + R_{23,41}}\right)^4 \left(\frac{(\ln 2)^2}{4} - \frac{(\ln 2)^3}{12}\right), \tag{2.48}$$

leads to:

$$\rho = \frac{\pi t}{\ln 2} \frac{R_{12,34} + R_{23,41}}{2}. \tag{2.49}$$

The accuracy of the measurement can be increased by utilizing the theorem of reciprocity and reversing the polarity. Based on the theorem of reciprocity $R_{12,34} = R_{34,12}$ is true. By measuring the additional 2 resistances that can be obtained this way the accuracy of the measurement can be increased. By switching the polarity of the current flow and voltage measurement the effect of any offset voltage, such as in the case of thermoelectric effects, can be observed and cancelled out. This leads to the measurement of 4 additional resistance values. At the end of the measurement, the resistance values should be averaged:

$$R_A = \frac{R_{12,34} + R_{34,12} + R_{21,43} + R_{43,21}}{4}, \tag{2.50}$$

$$R_B = \frac{R_{23,41} + R_{41,23} + R_{32,14} + R_{14,32}}{4}. \tag{2.51}$$

The measurement of all eight resistance values leads to a more accurate calculation of the resistivity by canceling out the effect of built in potentials. If the measurement of reciprocity or reversed polarity shows a high difference, then the measurement has an inaccuracy that should be further investigated. The resistivity can be calculated with the R_A and R_B average resistances as follows:

$$e^{-\frac{\pi R_A t}{\rho}} + e^{-\frac{\pi R_B t}{\rho}} = 1. \tag{2.52}$$

2.4.2 Hall effect measurement

Edwin Herbert Hall discovered the Hall effect in 1879[164] when he was studying the effect of magnetic field on conductors carrying an electric current. He found, that a potential difference arises between the two sides of the sample while the current flows through the sample in a magnetic field perpendicular to the current. He also observed that the polarity of the potential is different for different materials.

When a conductor or semiconductor is placed in a magnetic field perpendicular to its surface, and a current flows through the sample perpendicular to the magnetic field, a force acts upon the charge carriers in a direction perpendicular to both the magnetic field and the original flow of the current, the force is the Lorentz force. This force leads to the accumulation of one kind of charge carriers on the side determined by the charge of charge carriers creating an electric field until a steady state is reached. The steady state emerges between the Lorentz force propelling the charge carriers perpendicular to the current flow and the electrostatic force acting between the charge carriers on one side of the sample and the charge carriers being deflected towards them.

The force acting on the charge carriers that move in a magnetic and electric field is the Lorentz and electrostatic force. The two forces acting on a charge carrier lead to $\vec{F} = q \cdot (\vec{E} + \vec{v} \times \vec{B})$[40]. In the case of the Hall effect measurement the magnetic field ($\vec{B}$) is perpendicular to the flow of charge carriers with a drift velocity of $\vec{v}$. The electric field is the field from the accumulated charge carriers as a result of their displacement by the magnetic field. This leads to the following based on the Drude model[39, 40]:

$$\vec{F} = q\left(\vec{E} + \vec{v} \times \vec{B}\right) - \frac{m\vec{v}}{\tau}, \tag{2.53}$$

where τ is the average time between collision events for the charge carriers. In the y direction, perpendicular to the flow of the current and the magnetic field this leads to

$$F_y = eE_y - ev_x B_z - \frac{mv_y}{\tau}, \tag{2.54}$$

where the drift velocity is $v_x = \mu E_x$, E_x is the electric field in the x direction that creates the j_x current density in the material, and the mv_y/τ component is zero under equilibrium conditions. A schematic representation of the Hall effect measurement is shown in Figure 2.17. The x and y directional components of drift velocity, electric field, and current are shown for one type of charge carrier as well as the z directional magnetic field. The potential difference emerging as a result of the deflection of charge carriers can be measured, this is the Hall voltage denoted by V_{H}.

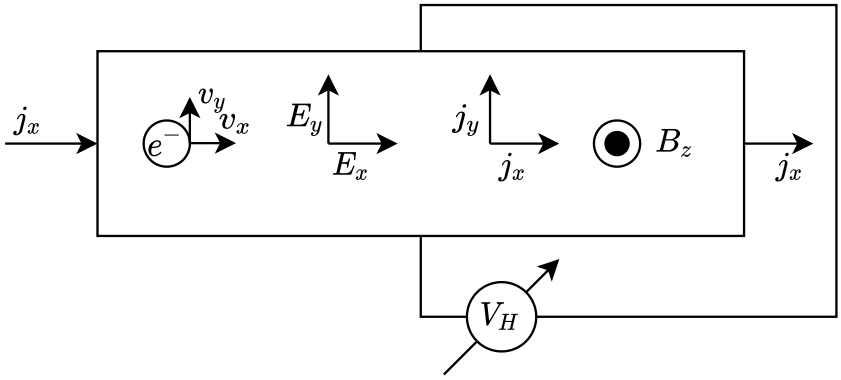

Figure 2.17: Schematic figure representing the direction of charge carrier transport, electric field, and magnetic field.

If one regards the F_y value as the effective force propelling the charge carriers in the y direction, it can be given in the form $F_y = \frac{ev_y}{\mu}$, where v_y is the velocity of charge carriers with mobility μ in the y direction. The text-book solution to the longitudinal resistivity gives $\rho_{xx} = \frac{1}{en\mu}$ and for the transversal term $\rho_{xy} = -\frac{B_z}{en}$.[40] The industry uses the method for the simultaneous determination of charge carrier density and mobility. This leads to the charge carrier density and mobility in the following form:

$$n = \frac{1}{e\left.\frac{\mathrm{d}\rho_{xy}}{\mathrm{d}B_z}\right|_{B_z=0}} \quad \text{and} \quad \mu = \frac{\left.\frac{\mathrm{d}\rho_{xy}}{\mathrm{d}B_z}\right|_{B_z=0}}{\rho_{xx}\left(B_z = 0\right)}. \tag{2.55}$$

The two-band Hall effect can be calculated in the simultaneous presence of holes and electrons[133, 165, 166]. The current density flowing through the material in case of two carriers is $j_x = epv_{x\mathrm{h}} + envx_{\mathrm{e}}$ where p is the density of holes, n is the density of electrons, and v_x denotes the velocity of charge carriers in the x direction as a result of the E_x electric field. The drift velocity of charge carriers in the y direction can be given in the following manner[166]:

$$F_{y\mathrm{h}} = eE_y - ev_{x\mathrm{h}}B_z, \tag{2.56}$$

$$-F_{y\mathrm{e}} = eE_y + ev_{x\mathrm{e}}B_z. \tag{2.57}$$

From these equations, we can obtain the current density in the y direction by substituting $F_y = \frac{ev_y}{\mu}$, which represents the drift of the charge carrier as a result of an effective force acting in the y direction. This value is null in equilibrium and will be substituted as such in the next step.

$$\frac{ev_{y\mathrm{h}}}{\mu_{\mathrm{h}}} = eE_y - ev_{x\mathrm{h}}B_z, \tag{2.58}$$

$$\frac{ev_{y\mathrm{e}}}{\mu_{\mathrm{e}}} = eE_y + ev_{x\mathrm{e}}B_z. \tag{2.59}$$

By multiplying both sides with the carrier density, rearranging the two equations, and adding the equations for electron and hole current density together, we obtain the current density of the holes and electrons perpendicular to the magnetic field and the current flow in the material denoted by j_x. With these steps, we reach:

$$j_y = e\left[\left(p\mu_\mathrm{h} + n\mu_\mathrm{e}\right)E_y - \left(p\mu_\mathrm{h}^2 + n\mu_\mathrm{e}^2\right)E_x B_z\right]. \tag{2.60}$$

Since the current in the y direction is zero in the case of equilibrium, the E_y electric field at the equilibrium condition can be obtained as follows:

$$E_y = \frac{p\mu_\mathrm{h}^2 - n\mu_\mathrm{e}^2}{p\mu_\mathrm{h} + n\mu_\mathrm{e}} E_x B_z = \frac{p\mu_\mathrm{h}^2 - n\mu_\mathrm{e}^2}{p\mu_\mathrm{h} + n\mu_\mathrm{e}} \frac{j_x}{e\left(p\mu_\mathrm{h} + n\mu_\mathrm{e}\right)} B_z. \tag{2.61}$$

From this, the Hall coefficient can be calculated by using the $R_\mathrm{H} = \frac{E_y}{j_x B_z}$ relation[40]:

$$R_\mathrm{H} = \frac{p\mu_\mathrm{h}^2 - n\mu_\mathrm{e}^2}{e\left(p\mu_\mathrm{h} + n\mu_\mathrm{e}\right)^2}. \tag{2.62}$$

It should be noted, that the results obtained for the Hall coefficient this way are true if the magnetic field is small[133, 165]. If the magnetic field is not small additional components are present in the calculation[133, 165]. Another solution would be to calculate the Hall coefficient with the help of the Boltzmann equation instead of the Drude model leading to a more accurate solution that includes the Hall scattering factor.

The one-band results can be reproduced easily from the two-band results by simply substituting zero in place of one of the charge carrier types. In the case of conductivity, the calculation leads to $\sigma = n_\mathrm{e} e\mu_\mathrm{e} + n_\mathrm{h} e\mu_\mathrm{h}$, from which the conductivity for a material containing only holes or electrons is $\sigma = n_\mathrm{h} e\mu_\mathrm{h}$ and $\sigma = n_\mathrm{e} e\mu_\mathrm{e}$ respectively[40]. The Hall coefficient can be similarly calculated leading to

$$R_\mathrm{H} = -\frac{1}{en} \quad \text{and} \quad R_\mathrm{H} = \frac{1}{ep} \tag{2.63}$$

for n and p-type materials respectively[133].

With these results, one can also calculate the resistivity matrix. The connection between the resistivity, electric field and current based on Ohm's law[167] is $\vec{E} = \overline{\overline{\rho}}\,\vec{j}$, or $\vec{j} = \overline{\overline{\sigma}}\vec{E}$ with conductivity where $\overline{\overline{\rho}}$ and $\overline{\overline{\sigma}}$ are the tensors of resistivity and conductivity, respectively. From the previous calculations, one can obtain the elements of the resistivity matrix as

$$\rho_{xx} = \frac{E_x}{j_x} = \frac{1}{e\left(n\mu_\mathrm{e} + p\mu_\mathrm{h}\right)} \quad \text{and} \quad \rho_{xy} = \frac{E_y}{j_x} = \frac{p\mu_\mathrm{h}^2 - n\mu_\mathrm{e}^2}{e\left(p\mu_\mathrm{h} + n\mu_\mathrm{e}\right)^2} B_z. \tag{2.64}$$

The Hall effect measurement consists of the measurement of the Hall voltage, V_H, between two diagonal points of the sample while a current flows through the sample between two other diagonal points. The sample is placed into a magnetic field perpendicular to the surface and the magnetic field usually changes during the measurement. The recording of Hall voltage values at different magnetic fields and using a Lock-in amplifier or fitting method increases the accuracy of the measurement. Figure 2.16. shows the pin sequence used for a Hall effect measurement on the right side. By measuring the Hall voltage, the charge carrier density for one carrier can be determined with the help of the ρ_{xy} value through $n = \frac{BI}{teV_\mathrm{H}}$, where t is the sample thickness.

The resistivity of the sample is obtained from the sheet resistance measurement without the presence of a magnetic field. With the help of the charge carrier density and resistivity values the mobility of charge carriers can be determined as $\mu = \frac{1}{en\rho}$. The thickness of the sample is not needed for the calculation of the mobility, since if the thickness is not known, the resistivity and carrier density both contain the thickness and it falls out during the calculation.

Chapter 3

Experimental Methods

In this chapter, I present the measurement methods and tools used during the research I conducted. The measurements presented in Chapters 4-6 were conducted with the help of the devices detailed in this chapter. The chapter presents two experimental systems developed for the measurement of temperature-dependent charge carrier recombination time with the microwave-detected photoconductivity decay method and a tool for the measurement of sheet resistance, charge carrier density, and mobility with the van der Pauw method and Hall effect measurement. At the end of the chapter, I present the sample preparation process for the materials used during the experiments.

3.1 Microwave photoconductivity decay measurements

The experimental setup presented in this section is based on my publications presenting measurement results with the systems and the system itself. The articles presenting the CPW-based experimental setup are titled *Millisecond-Scale Charge-Carrier Recombination Dynamics in the CsPbBr3 Perovskite*[O2] and *Time-resolved photoconductivity decay measurements with broad-band radiofrequency detection and excitation energy*[O3]. The article detailing the cavity-based measurement is titled *Ultralong Charge Carrier Recombination Time in Methylammonium Lead Halide Perovskites*[O1].

3.1.1 Evaluation of charge-carrier recombination dynamics

In Chapter 5, the charge carrier recombination dynamics of $CsPbBr_3$ single crystals are presented. Since the recombination time of the material changes significantly in the observed charge carrier density range, the fitting of one exponential decay process is not sufficient for the evaluation of the charge carrier lifetime. Due to this, the apparent charge-carrier recombination time can be evaluated[150, 162] using the rate equations presented in Equation 2.41.

Since the connection between the change in conductivity and the change in the reflected microwave voltage is assumed to be linear[148, 149, 151] and the connection between the conductivity and charge carrier density is linear, the charge-carrier recombination time can be evaluated based on the derivative of the photoconductivity signal as shown in Equation 2.42.

The easiest way to calculate the apparent charge-carrier recombination time based on these connections would be the numerical differentiation of the raw signal and the division of the

signal with the derivative. However, the noise of the measurement does not allow for such a solution, since the raw signal has a high enough noise to prevent this. The smoothing of the measurement results helps with the noise of the measurement, but the standard deviation of the results leads to the recombination time changing orders of magnitude from point to point.

The solution to this problem is the binning of the measurement data proposed and implemented by Dávid Krisztián. The measurement is divided into several parts and all measured points of the signal are averaged into one point. This leads to the advanced realization of the same principle that lies behind the smoothing of the signal. I used a binning method where the measured signal is divided along the y axis in a logarithmic manner. This leads to more points at the end of the relaxation process compared to the linear binning method while the bin size at the end of the measurement is bigger, than at the beginning of the measurement. It is important to increase the bin size at the end of the relaxation process since this allows for the higher amount of averaged data points leading to the accurate measurement of the recombination process. The bin size in the linear binning method is larger at the end of the recombination process. This means that the linear method provides a higher averaging at the end of the process than the logarithmic method and both of these calculations result in a higher averaging at the end of the process than at the beginning. Depending on the noise of the signal under investigation one or the other binning method should be chosen.

The detailed process behind the evaluation of charge-carrier recombination time is presented in Figure 3.1. Subfigure (a) shows the raw reflected microwave signal measured at 22 K for a $CsPbBr_3$ single crystal and the bins of the different binning methods as scatter plots on the signal. Subfigures (b-d) present different evaluation processes for the charge-carrier recombination dynamics. In subfigure (b) the signal is smoothed for 2000 points and the derivative of this signal is used for the evaluation process presented in Equation 2.42, to fall in line with the bin numbers used in the next step. Subfigures (c) and (d) were created by dividing the measurement results into 50 parts in either a linear or logarithmic manner along the y-axis after which the previously detailed method was used for the calculation of τ_c.

3.1.2 CPW-based experiment

A photograph of the coplanar waveguide-based measurement setup is presented in Figure 3.2. The block diagram of the experimental arrangement is shown in Figure 5.1. The measurement setup is capable of the temperature-dependent measurement of transient and steady-state photoconductivity. If time-resolved microwave photoconductivity decay measurements are conducted, the measurement system includes a high speed oscilloscope. For steady-state measurements, a lock-in amplifier is used and an optical chopper creates the dark and illuminated states. The system includes the options of IQ mixer-based and crystal detector-based detection.

Microwave source

The signal source is the most integral part of a microwave measurement system. The source used in this experimental setup (MKU LO 8-13 PLL, Kühne GmbH) can create signals in the $8.4 - 13.6$ GHz frequency range with a power level of 13 dBm.

The measurement can be extended to lower frequencies with a signal generator (SDG 1050, Siglent Inc.) that can operate in the radio frequency regime up to 50 MHz. If this frequency regime is used, some components of the system (for example, the Magic tee) must be changed to lower frequency variants.

The coplanar waveguide

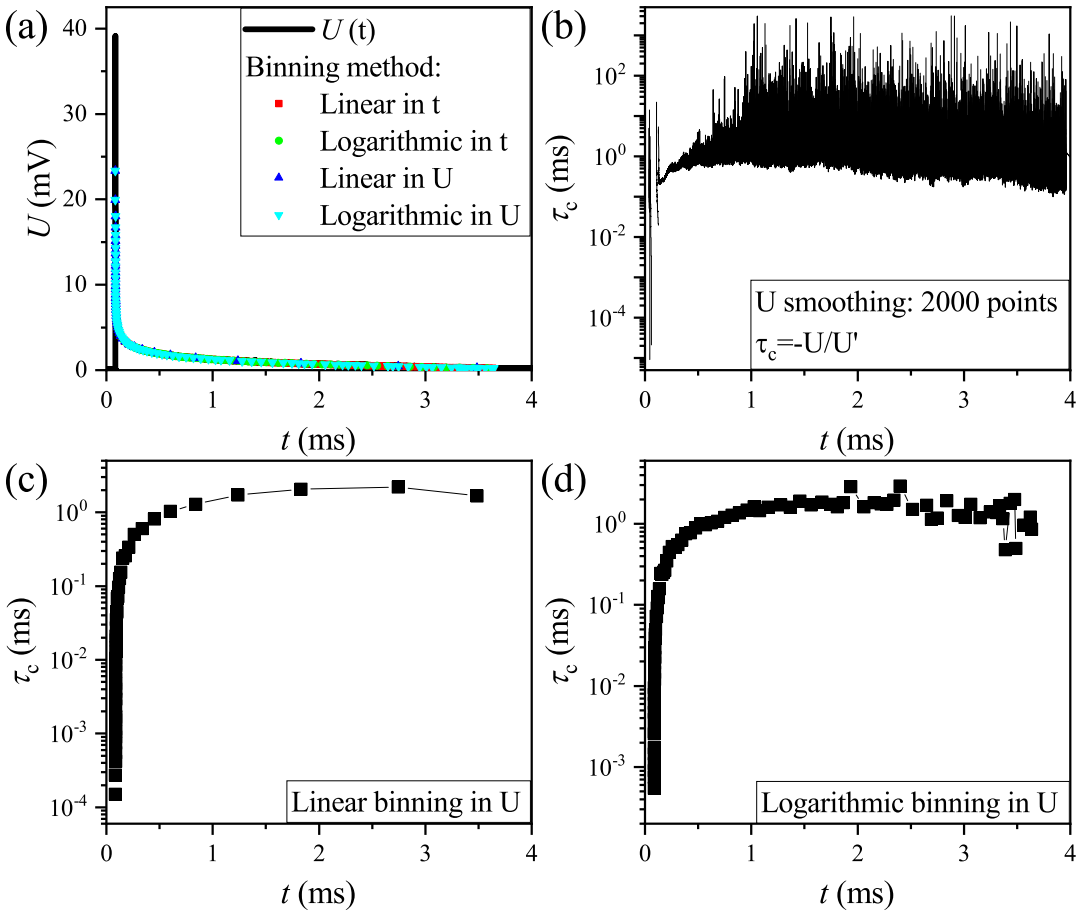

Figure 3.1: (a): Raw signal with the averaged values of the binning methods scattered on the signal. (b): Charge-carrier recombination dynamics calculated by smoothing the signal before the numerical derivation. (c-d): Charge-carrier recombination dynamics calculated by binning the measured data into linearly or logarithmically distributed bins.

The μPCD measurement can be realized with either an antenna or a cavity. The antenna can be a waveguide with the sample placed at the end of the waveguide, thus realizing the probing of the material. In this experimental system, the antenna approach is used, and the antenna is a coplanar waveguide[152, 168] that fulfills the role of emitting the probing microwave radiation and receiving the reflected microwave signal. The coplanar waveguide (CPW) used in this study is a conductor-backed coplanar waveguide (CBCPW). This device consists of a dielectric material between two conducting layers. The dielectric material is usually ceramic. The backside of the CPW is connected to the ground. The front side of the device is divided into three parts separated by gaps. The central strip is connected to the signal while the two metallic surfaces beside it are connected to the backside with so-called via-holes, holes in the dielectric layer with metallic filling that connect the metallic layer on the front and backside. The central strip and the two metallic regions are connected to the signal and ground of an SMA connector with soldering. A photograph of such a device is shown in Figure 3.3. The schematic diagram of the CPW is also shown in Figure 3.3 in subfigure (b).

The electric and magnetic field of a coplanar waveguide is shown in Figure 3.4. The mag-

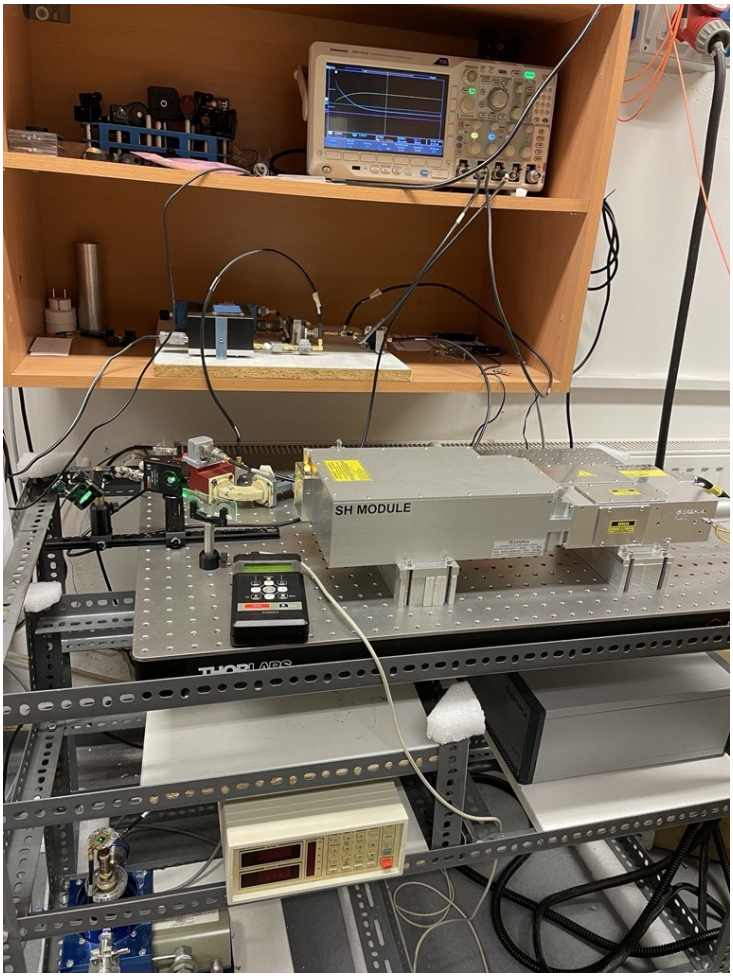

Figure 3.2: Experimental setup built with a coplanar waveguide acting as the antenna. The measurement system includes a cryostat, a Q-switched pulsed laser that can be easily switched between 532 nm and 1064 nm output, a self-assembled microwave bridge responsible for the generation and downconversion of the microwave signal, and an oscilloscope for the transient photoconductivity measurement.

netic field flux is highest above the gap between the signal and ground strips. The sample should be placed at the point with the highest magnetic field, which is above the gap. The reason behind this is that the μPCD signal is proportional to the magnetic field.

The wave impedance of the coplanar waveguide is designed to be $Z_0 = 50\ \Omega$. The wave impedance can be calculated with the following equation[152]:

$$Z_0 = \sqrt{\frac{\widetilde{R} + \mathrm{i}\omega\widetilde{L}}{\widetilde{G} + \mathrm{i}\omega\widetilde{C}}}, \tag{3.1}$$

where $\widetilde{L}$ is the inductance, $\widetilde{C}$ is the capacitance, $\widetilde{R}$ is the series resistance, and $\widetilde{G}$ is the shunt conductance of the waveguide, and all of these parameters are normalized to the unit length[152]. The equivalent circuit of a coplanar waveguide is shown in Figure 3.5. In this model, the $\widetilde{R}$ and $\widetilde{G}$ components are responsible for the loss in the waveguide. In an ideal, lossless system these parameters are zero and only the inductance and capacitance remain.

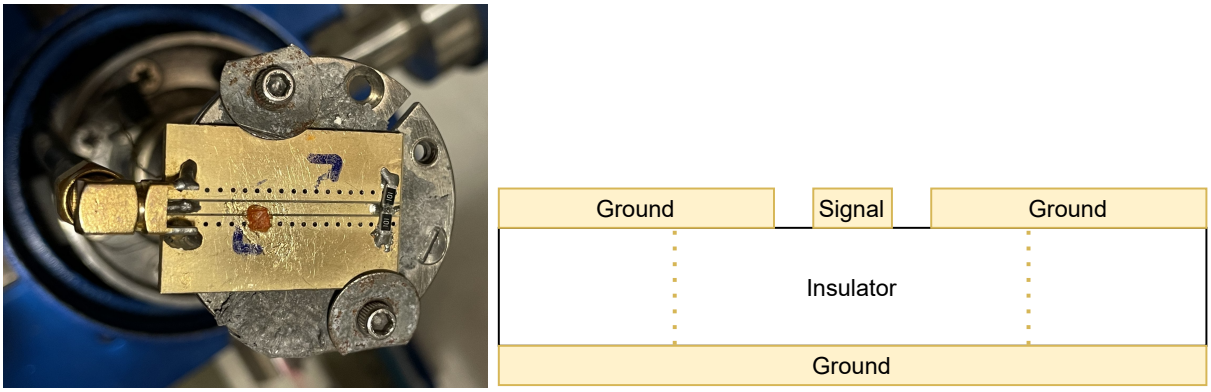

Figure 3.3: Left side: Photograph of the CPW placed on the cold finger of the cryostat. A sample is located on the surface of the CPW. The waveguide is terminated with two SMD resistances to realize a 50 Ω termination. Right side: cross-section of the conductor-backed coplanar waveguide. The dotted line in the insulator layer represents the via-holes.

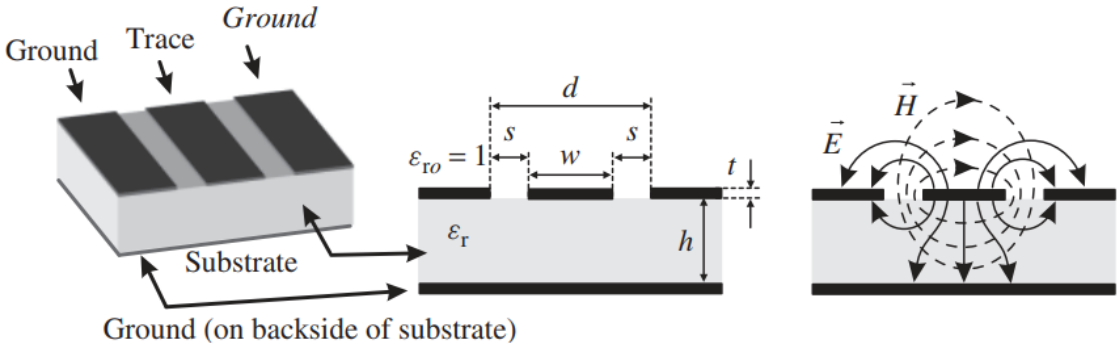

Figure 3.4: The geometry of a conductor-backed CPW is presented on the left and in the middle. The image on the right side presents a quasi-TEM wave's electric and magnetic field distribution. From *RF and Microwave Engineering: Fundamentals of Wireless Communications* by Frank Gustrau [169].

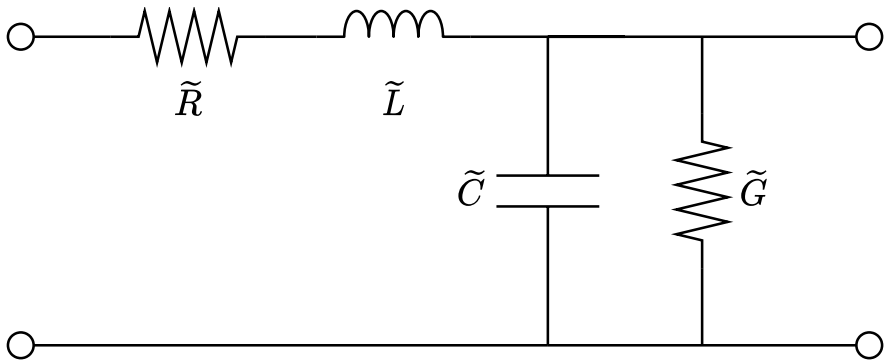

Figure 3.5: Equivalent circuit of a coplanar waveguide. The model is normalized to unit length.

Cryostat

The cryostat (M-22, CTI-CRYOGENICS) of the system is responsible for the cooling of the samples to cryogenic temperatures down to 10 K. The cryostat is equipped with a closed-cycle

helium refrigeration system that cools the sample through a cold finger.

Temperature controller

The temperature controller (LakeShore model 330, Lake Shore) is responsible for the control of the sample temperature. With a properly calibrated PID system and a thermometer on the sample stage, it can set the heating of the system to accurately stabilize the temperature of the sample.

Vacuum pump

For low-temperature measurements it is important to realize a high enough vacuum in the chamber of the cryostat, this way preventing the condensation and freezing of the contents of air inside the cryostat as well as decreasing the lowest possible temperature achievable with the system. The vacuum stand used in the setup (PT 50, Leybold systems) is a two-stage vacuum system with a turbomolecular pump and a rotary vane vacuum pump.

Lasers

A good optical excitation used during the measurement is of utmost importance. For pulsed measurements, a small pulse width enables the observation of quick processes, a tuneable repetition rate enables the observation of quick and slow processes by allowing for the appropriate relaxation time between pulses, and a high pulse energy results in higher excitation leading to a better signal-to-noise ratio. The laser used for the TRMCD measurements (NL201-2.5k-SH-mot, Ekspla) can be set for two wavelengths, 532 nm and 1064 nm, the repetition rate can be set up until 2500 Hz. The laser used for the Continuous Wave measurements (MGL-III-532-200 mW) has a wavelength of 532 nm. The experimental system can be expanded with multiple other excitation options with ease.

IQ Mixer

The IQ mixer (IQ-0618LXP, Marki Microwave Inc.) makes possible the detection of radiofrequency signals with high accuracy in the $6 - 18$ GHz frequency range. The two inputs of the instrument are a local oscillator (LO) port for the reference signal and a radio frequency (RF) port for the signal of interest. The instrument creates the sum and difference of the two signals and uses a low-pass filter to filter out the high-frequency component. This way a signal is obtained that corresponds to the change in the reflected microwave voltage and can be detected with an oscilloscope as a DC signal. The I and Q outputs of the IQ mixer are the in-phase (I) and out-of-phase (Q) components of the signal and correspond to the vectorial form of the measured signal. The Q output is obtained by applying a 90-degree phase shift to the LO signal and creating the difference signal in the same manner as mentioned before. The block diagram of the device is shown in Figure 3.6.

Crystal detector

The crystal detector (8472B, Hewlett Packard) is responsible for rectifying the signal thus enabling the measurement in the 10 MHz $- 18$ GHz frequency range. The output of the crystal detector corresponds to the amplitude of the radio frequency signal connected to the input of the device. By connecting the output to either an oscilloscope or lock-in amplifier, the changing amplitude of the reflected microwave signal can be measured.

Lock-in amplifier

For the steady-state measurement utilizing a CW laser and an optical chopper, a lock-in amplifier is used (SR830, Stanford Research Systems). This enables the accurate measurement of small changes in the signal level.

Oscilloscope

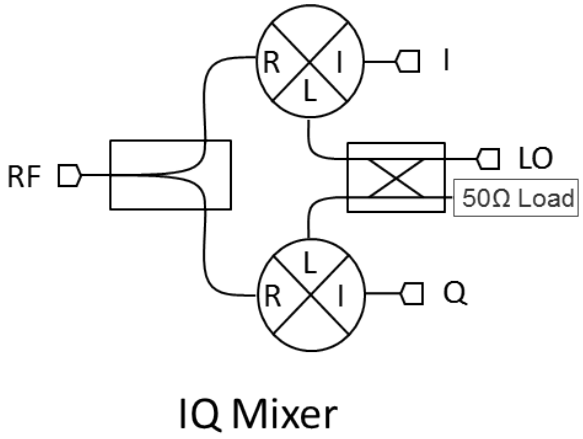

Figure 3.6: Block diagram of the IQ mixer. Downloaded from the manufacturers website, https://markimicrowave.com/products/connectorized/iq-mixers/iq-0618lxp/datasheet/ [170].

The I and Q outputs of the IQ mixer, the signal of the photodetector, and the signal coming from the crystal detector can be digitalized with a high-speed oscilloscope (Tektronix MDO 3024). This allows the measurement of charge carrier recombination dynamics in a huge dynamic range.

Isolator

The isolator (T-8S43U-20, Teledyne Microwave Solutions) placed after the hybrid coupler prevents any signal originating from the sample or other components of the system from traveling toward the signal generator. This prevents any potential damage from occurring by sending a signal onto the output of the microwave generator.

Hybrid coupler

The hybrid coupler used in this setup (Micronde R433721) splits the signal originating from the microwave generator into two equal parts with one of the outputs having a 90-degree phase shift. One part of the signal is sent towards the LO input of the IQ mixer while the other half is sent towards the sample.

Phase shifter

The phase shifter located before the LO input of the IQ mixer allows for the accurate setting of the phase of the signal sent to the LO input of the mixer. This allows for the accurate setting of the LO phase, resulting in the possible tuning of the signal on the I and Q output of the IQ mixer.

Phase shifter and amplitude modulator

The reference arm of the Magic tee consists of two components, a phase shifter (DKX 1) and an attenuator (TZC 504 Variable Attenuator, TKI). Both instruments are rectangular waveguides that are equipped with a movable wall. By setting the length of the reference arm with the help of the movable end wall, the phase of the reflected microwave signal can be tuned. By setting the cross-section in the middle of the waveguide, the attenuation can be set for the signal reflected from the reference arm. These two components allow for the accurate setting of the phase and amplitude of the reference arm of the Magic tee.

Low-noise amplifier

A low-noise amplifier (LNA) made by JaniLab Inc. is used in the measurement system

to amplify the signal before the IQ mixer. This ensures a detectable, strong signal during the measurement process. In the case of a strong photo response leading to a high signal level without the amplifier, the amplifier can be removed to prevent saturating or damaging the mixer. The amplifier works in the $6-18$ GHz range, has a gain of 18 dB, and has a noise figure of 1.7 dB.

Photodetector

The signal of a photodetector (DET36A/M, Thorlabs) is used for the triggering of the measurement when a TRMCD measurement is conducted. A small portion of the exciting laser pulse is outcoupled with a beam sampler onto the photodetector to synchronize the excitation and the measurement. The detector is sensitive in the $350-1100$ nm wavelength range, has a fast rise and fall time, and has a wide bandwidth.

DC blocks

It is important to galvanically isolate the IQ mixer from the rest of the measurement system to prevent applying any DC signals onto its LO and RF inputs. A high enough DC voltage can saturate or damage the mixer. To achieve this, two SMA-WR90 connectors were used facing each other with plastic sheets placed between them and plastic screws holding them together. The DC blocks are placed before the LO and RF inputs of the mixer.

Coaxial cables

The connection between instruments is realized with the help of coaxial cables with SMA and BNC connections. The usage of coaxial cables helps with decreasing the unwanted noises during the measurement process.

Magic tee

The Magic tee (TKI) is responsible for splitting the signal sent to its 'A' input into two equal parts and sending it toward a reference arm and the sample. It is also responsible for sending the signals reflected from the reference and sample arm toward its output 'D'. The exact process is detailed in the next subsection. The Magic tee used in the system is a rectangular waveguide-based instrument that is ideal for the 10 GHz frequency range.

Purpose of the Magic tee

The Magic tee is an instrument that splits the signal connected to the input to two ports and combines the signals input to the same two ports on the fourth port. If the 'A' port of the Magic tee receives a signal the signal is split in two and sent to the ports 'C' towards the reference arm and 'D' towards the sample. The phase of the signal sent to port 'C' is shifted by π. The signals going out from ports 'C' and 'D' are reflected from the sample and the reference arm respectively and re-enter the Magic tee. The reflection coming from the sample consists of two parts, a DC reflection caused by the sample without excitation and a reflection caused by the excitation during illumination. We set the phase shifter and attenuator located in the reference arm in a way that once the signals are added together on the output of port 'B' the DC reflection of the sample is canceled out. If we take the signal in the following form:

$$W = E \cdot \cos(kx - \omega t + \phi), \tag{3.2}$$

where E is the amplitude, k is the wavenumber, ω is the frequency, and ϕ is the phase of the signal. In this case, the signal going toward channel 'B' consists of the sum of the reflections received from channels 'C' and 'D' as follows:

$$W_{\text{D->B}} = F \cdot \cos(kx - \omega t + \phi_1) + G \cdot \cos(kx - \omega t + \phi_2), \tag{3.3}$$

$$W_{\text{C->B}} = H \cdot \cos(kx - \omega t + \phi_3), \tag{3.4}$$

$$W_{\text{B}} = W_{\text{C->B}} + W_{\text{D->B}}, \tag{3.5}$$

where F, G, and H are the signal amplitudes, the second term of $W_{\text{D->B}}$ is the signal caused by the photoexcitation, and we can tune the values of H and ϕ_3. Considering the trigonometric identity of the product of two cosine functions, $\cos(a) + \cos(b) = 2 \cdot \cos\left(\frac{a-b}{2}\right) \cos\left(\frac{a+b}{2}\right)$ it can be shown that the DC reflection of the sample can be canceled out. To do this one should set the attenuation and phase shift in the reference arm in such a way, that $F = H$ and $\frac{\phi_1 - \phi_2}{2} = n \cdot \pi/2$ are satisfied. This leaves only the change caused by the photoexcitation to remain, in an ideal case only a 0 DC level remains with the perturbation caused by photoexcitation changing this value periodically.

3.1.3 Cavity-based experiment

The cavity-based experiment utilizes components of a commercially available electron spin resonance spectrometer (BrukerElexsys E500). The measurement is made outstandingly sensitive by using the microwave bridge and cavity of the electron spin resonance spectrometer and by utilizing the automatic frequency control of the system. The block diagram of the measurement setup is demonstrated in Figure 4.1.

Signal preamplifier

The preamplifier (ER 047-PH, Bruker BioSpin) built into the spectrometer was used to increase the signal-to-noise ratio through the amplification of the signal thus achieving the detection of signals that would be lost in the noise otherwise.

Microwave bridge

The microwave bridge (ER049X, Bruker BioSpin) used in the measurements provides a plug-and-play solution for microwave measurements with high sensitivity.

Cavity

With the help of the microwave cavity (ER4122SHQE, BioSpin high-Q cavity) the effect of photoinduced change in conductivity is amplified for an outstanding detection capability[147, 171–173].

Cryostat

The cryostat used in the experimental system (ESR900, Oxford Instr. Sci.Div.) allows for the accurate setting of sample temperature between 4 K and room temperature. The system can be precooled to 4 K without the sample, this way allowing the placement of the sample into the cooled cryostat. This method is essential for the quenched measurements.

Lock-in amplifier

The lock-in amplifier used in this system (SR830, Stanford Research Systems) is responsible for the accurate measurement of the difference in the reflected signal between the dark and excited case. The reference signal of the optical chopper is connected to the reference signal of the lock-in amplifier.

Lasers

Two lasers were used for the measurements since the steady-state and transient measurements require vastly different excitation solutions. For the time-resolved measurements, a Q-switched pulsed laser (NPL45C, Thorlabs Inc.) was used with a wavelength of $\lambda = 450$ nm. The laser has a pulse width that can be set on the $6 - 129$ ns scale and a pulse energy of 200 nJ. The continuous wave laser (MBL-III-473, CNI LasersLtd) has a wavelength of 473 nm and a power of 50 mW.

Optical chopper

An optical chopper (SR540, Stanford Research Systems Inc.) was used to chop the CW laser for the lock-in based detection of the steady-state signal. This method provides illuminated and dark measurements with equal excitation time. The reference signal of the chopper can be used as the reference signal of the lock-in amplifier.

3.2 Hall effect and sheet resistance measurement

For the measurement of charge carrier density, mobility, and sheet resistance I used a commercially available standalone tool in the form of the PDL-1000. For the optical illumination, I used UV LEDs with appropriate wavelength for the amorphous Indium Gallium Zinc Oxide and α Gallium Oxide thin films. The PDL-1000 system is presented in Figure 3.7.

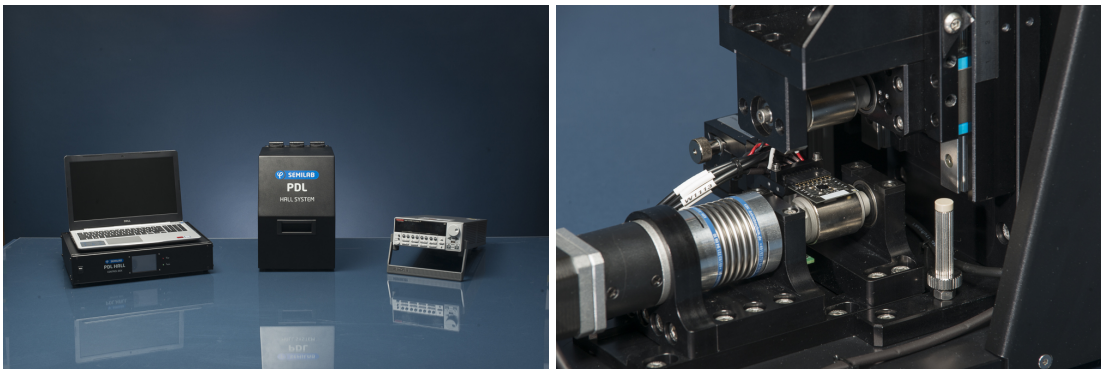

Figure 3.7: The PDL-1000 Hall effect measurement system is shown on the left side and the cylindrical magnet pair inside the measurement system is shown on the right side[174].

PDL-1000

The PDL-1000 used for the Hall measurements is a standalone tool for the measurement and evaluation of sheet resistance, charge carrier density, and mobility developed by Semilab. The system conducts contact check, sheet resistance, and Hall effect measurements and their evaluation automatically. For the presented measurements I used a needle stage setup for the contacting of the samples.

The PDL-1000 is equipped with a parallel dipole line system[175]. The two, cylindrical magnets create a homogeneous magnetic field between them. The lower magnet is rotated with a stepper motor, and the magnetic coupling between the lower and upper magnet causes the upper magnet to rotate with the lower magnet thus realizing a harmonic change in the magnetic field perpendicular to the sample surface. Due to this sinusoidically changing magnetic field, the Hall voltage changes with the same tendencies, realizing a Hall measurement with an AC

magnetic field. This solution allows for the utilization of a lock-in amplifier for an outstanding signal-to-noise ratio in the Hall effect measurement.

Optical illumination in the UV regime

For the illuminated measurements, I applied an optical excitation with the help of UV LEDs. The LED used for the measurement of Indium Gallium Zinc Oxide thin film samples (M340L5, Thorlabs) has a wavelength of 340 nm and a maximal power of 69.2 mW. A lens was placed before the LED to create a homogeneous excitation of the whole sample surface. The LED used for the optical excitation of Ga_2O_3 samples (DUV265-SD353E, Roithner LaserTechnik GmbH) has a central wavelength of 265 nm.

3.3 Studied samples

Thanks to multiple international cooperations I had the opportunity to measure perovskite samples and wide bandgap materials. I did not manufacture or take part in the manufacturing process for any of the samples used during the measurement processes.

The perovskite samples created by the group have been the focus of multiple publications including but not limited to their usefulness as X-ray detectors [48], information storage devices [176], and gas sensors [15].

$MAPbX_3$

The $MAPbX_3$ samples were created with three different preparation methods. The acid-based growth consists of the pipetting of methylamine solution into an ice-cooled solution of PbX_2. In a temperature gradient of 15 °C in the acidic media, single crystals of the methylammonium lead halides grow on the cold side of the liquid container. The inverse temperature method consists of dissolving $MAPbBr_3$ crystals in DMF at room temperature thus creating a saturated solution. By increasing the temperature of the solution nice, cube-shaped samples can be grown. The method requires γ-butyrolactone and 50 V/V% DMF / 50 V/V% dimethyl sulfoxide (DMSO) in the case of $MAPbI_3$ and $MAPbCl_3$, respectively. The needle-shaped crystals were created by cooling down the saturated solution from room temperature to -15 °C and harvesting the crystals at this temperature. Three $MAPbX_3$ samples are shown in Figure 3.8. Márton Kollár synthesized the samples at The École Polytechnique Fédérale de Lausanne.

$CsPbBr_3$

The $CsPbBr_3$ single crystals were grown with the inverse temperature growth technique[177, 178] from a precursor solution. The precursor solution is heated up to 120 °C and the forming crystals are harvested. The crystals are then placed into a fresh precursor solution and act as seed crystals for the growth process. The precursor solution was created with a modified version of the method published by Dirin *et al.*[179] by dissolving CsBr and $PbBr_2$ in DMSO, heating and steering the solution, and filtering at the end of the process. A $CsPbBr_3$ single crystal is presented in Figure 3.8. Márton Kollár synthesized the samples at the KEP Innovation Center.

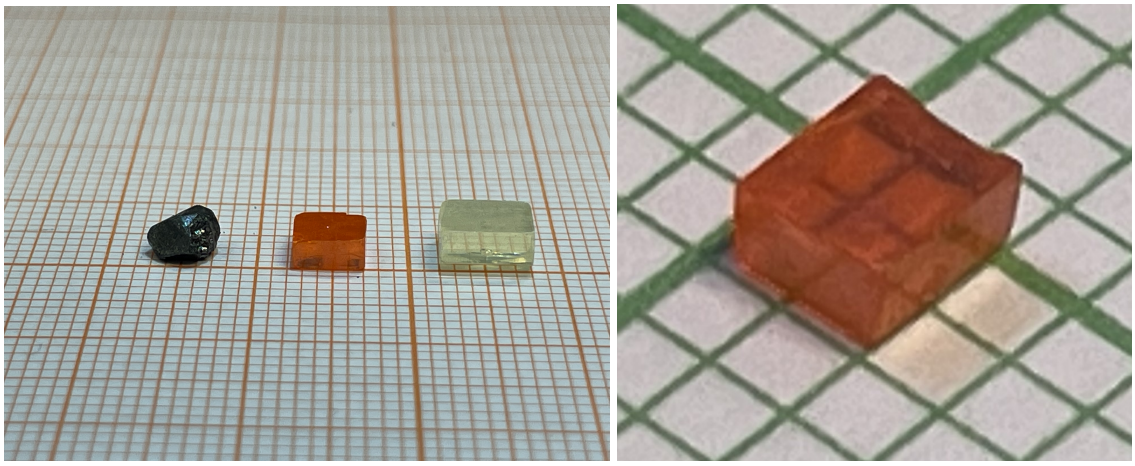

Figure 3.8: Left side: Three methylammonium lead halide single crystals presented on millimeter paper for scale. From left to right: $CH_3NH_3PbI_3$, $CH_3NH_3PbBr_3$, and $CH_3NH_3PbCl_3$. Right side: $CsPbBr_3$ single crystal placed on millimeter paper for scale.

Amorphous indium gallium zinc oxide

The amorphous indium gallium zinc oxide (a-IGZO) samples were created with physical vapor deposition. The process consists of sputtering atoms on a carrier substrate in an atmosphere that is a mixture of Argon and O_2. The high-quality film is created with thermal treatment. The sample series contains samples with varying thicknesses, the partial pressure of oxygen in the chamber during the preparation process, and the presence and lack of an insulation layer.

α-Ga_2O_3

The α-Ga_2O_3 sample was created with the mist CVD technique. The substrate used for the process is an M-plane sapphire. The sample was created with a thickness of 1400 nm in the van der Pauw geometry. The sample had a Si/Ga ratio of 10^{-4} in the source thus realizing the Silicon doping of the material. The α-Ga_2O_3 samples were made by Hitoshi Takane at Kyoto University.

Chapter 4

Charge-Carrier Dynamics in Hybrid Organic-Inorganic Perovskites

In this Chapter, I present the time-resolved microwave photoconductivity measurement of methylammonium lead halide single crystals on a temperature range of 4 to 290 K. With the presented measurement method I present the change in photoconductivity and the charge-carrier recombination time as a function of temperature. I performed the non-destructive and contactless measurement method for all three parent metal halide perovskites, namely $MAPbI_3$, $MAPbBr_3$, and $MAPbCl_3$ single crystals. I present the effect of structural phase transitions on the charge-carrier recombination dynamics of the materials. I observed substantial change in photoconductivity and recombination dynamics at the orthorhombic to tetragonal phase transition while no such effect is observable at the tetragonal to cubic transition. I present ultralong charge-carrier recombination times approaching 70 μs in the orthorhombic phase. I present further results detailing the difference in slowly cooled and quenched samples. I compared the temperature-dependent photoconductivity and recombination time in three samples with vastly different morphology. The quenched and morphology-based measurements show the importance of the amount of domain barriers found in the samples and the effect of these domains on the photoconductivity and charge-carrier recombination time of photoexcited charge carriers in perovskites.

The presented results shed light on the interplay between the structure of methylammonium lead halide crystals and the photovoltaic properties relevant to the application of methylammonium lead halides as solar cell materials, namely the recombination time and photoconductivity. A deeper understanding of the effects influencing the recombination process of charge carriers can propel further improvement of the photovoltaic efficiency of hybrid organic-inorganic perovskites. The presence of significantly longer charge-carrier recombination times in the orthorhombic phase indicates that research connected to the development of perovskite samples that possess similar properties at room temperature may help with the improvement of such devices.

The measurements presented herein were conducted with the help of a high quality factor microwave resonator, a commercially available microwave bridge, and a helium gas flow cryostat. The optical excitation was realized with a Q-switched laser for the transient measurements and a CW laser for the QSS measurements. The measurement system was developed for the temperature-dependent recombination time study of methylammonium lead halides.

The presented measurement of the temperature-dependent recombination dynamics of

charge carriers in methylammonium lead halides, the effect of morphology on the recombination dynamics, and observation of quenched single crystals presenting substantially different recombination dynamics than the slowly cooled perovskites, and the novel solution for the measurement of charge-carrier recombination time as a function of temperature with the help of a microwave cavity and bridge of an electron spin resonance spectrometer are published in ACS Photonics. [O1]

4.1 Measurement of charge-carrier recombination time and photoconductivity with a microwave cavity

I studied the photoinduced charge-carrier recombination dynamics of methylammonium lead halide samples in a wide temperature range with the microwave photoconductivity decay method. The microwave photoconductivity measurement setup used during the research presented in this chapter is shown in Figure 4.1. The presented measurements were conducted in the $4-270$ K temperature range.

The measurement system was built based on the components of a commercially available electron spin resonance spectrometer. The two components used during the presented measurements are the microwave cavity with a high Q-factor and the microwave bridge with automatic frequency control. The microwave cavity allows for a measurement with high sensitivity and the automatic frequency control sets the frequency of the microwave source to the resonant frequency of the cavity. The microwave bridge of the ESR spectrometer is surrounded by a dotted line in the block diagram presented in Figure 4.1., the cavity is also part of the spectrometer. The setup contains two possible solutions for illumination, the optical chopper is needed in the case of the CW illumination. Subfigure (b) and (c) present the light delivery solution to the sample placed inside the cavity through a quartz rod.

The optical excitation of a material changes its surface impedance. The perturbation of surface impedance leads to the change in the quality factor of the cavity and the change in the resonant frequency of the cavity. Due to the application of the automatic frequency control, the microwave bridge realizes a measurement where only the change in the Q-factor is measured, which is connected to the change in sample conductivity. A detailed description of microwave measurement of surface impedance is given in the Theoretical Background chapter.

Due to the utilization of the microwave cavity of the ESR spectrometer, the possibility arises for rapidly cooled measurements. Thanks to the design of such cavities, the sample can be placed inside the cooled cavity filled with helium thus realizing the quenching of sample properties through quick cooling. The bandwidth of the cavity limits the detectable recombination dynamics of the samples under investigation due to the shortest detectable transient being $\tau_{\mathrm{tr}} = 2Q/\omega_0$. The quality factor of the loaded cavity is $Q \approx 6550$, and the probing microwave frequency is $\omega_0 \approx 2\pi \cdot 9.5$ GHz, leading to a lower limit of $\tau_{\mathrm{tr}} \approx 220$ ns for the measurement of recombination dynamics. Since the detected recombination time values in the presented measurements are in the range of microseconds and above, the limitation imposed by the bandwidth of the system does not pose any problem.

The sample is placed into the center of a microwave cavity where the magnetic field is maximal. The electromagnetic mode of the cavity is TE011. The cavity is equipped with a double-walled quartz insert allowing for liquid helium cooling, resulting in a temperature range

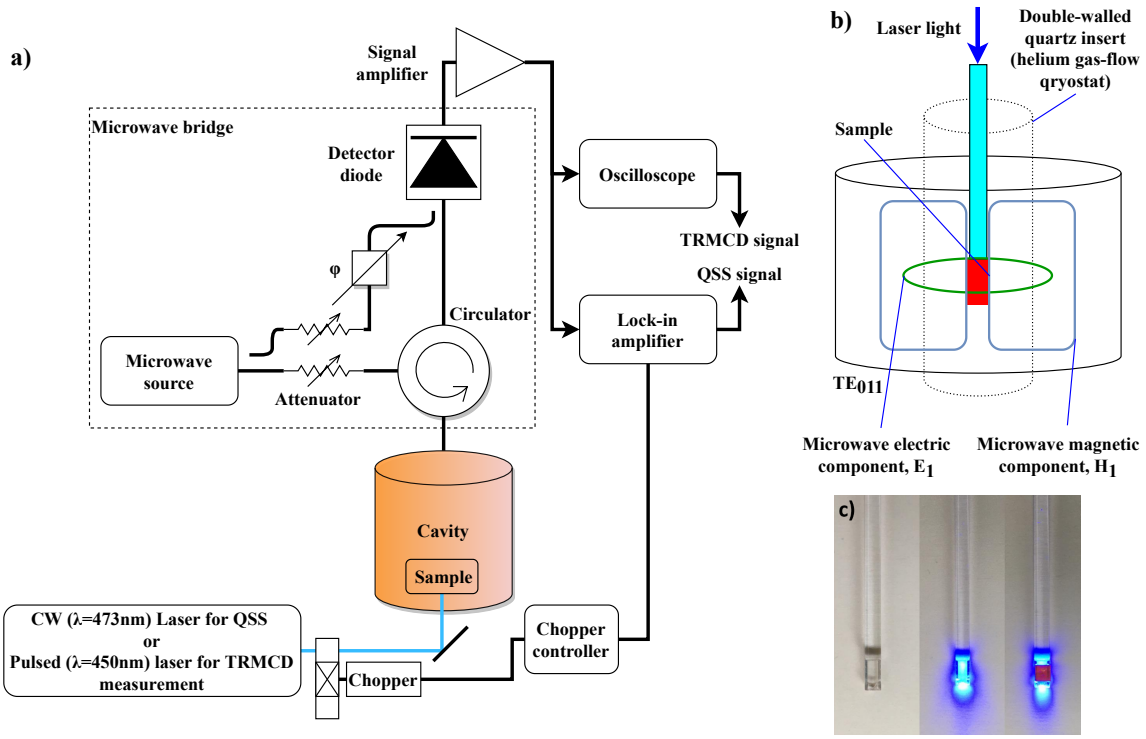

Figure 4.1: The experimental setup used for microwave photoconductivity measurements during the presented study is shown in subfigure (a). The block diagram includes the modification needed for switching between steady-state and transient photoconductivity measurements. (b) Schematic diagram of laser light delivery to the sample placed inside the microwave cavity with the TEM modes of the cavity presented. The illustration of the light delivery system is presented in subfigure (c). The left photo in (c) presents the quartz rod used during the measurement without the sample, the middle photo shows the same rod when the optical excitation is present, and the right photo shows the $MAPbBr_3$ sample attached to the rod ready for measurement. The optical excitation used for the illustration of the light delivery system is not the same, as the laser used for the measurement. The light source used for illustration is a CW LED with a wavelength of $\lambda = 470$ nm made by ADSresonances Sàrl.

of $4 - 300$ K for the measurement.

The samples were illuminated with the help of a quartz rod by placing the sample on the bottom notch of one end of the quartz rod while the light was directed at the other end of the rod. Due to the refractive index of the quartz rod, the light is guided along the length of the rod and excites the sample placed at the other end. This illumination technique was based on the solution previously presented by Mantulnikows *et al.*[180].

The measurement system is capable of both transient and steady-state photoconductivity measurements. For the transient photoconductivity decay measurements the excitation of the sample happens with a Q-switched pulsed laser that has a 450 nm wavelength. The decay curves are measured with an oscilloscope placed after an amplifier and recorded with the help of a measurement software. For the steady-state measurement, a CW laser is used with a wavelength of 473 nm. The CW laser is chopped with an optical chopper. This way the steady-state photoconductivity can be measured as a change from the corresponding value in dark condi-

tions. The reference signal of the chopper is connected to a lock-in amplifier thus realizing the measurement of the difference in the dark and illuminated photoconductivity.

The comparison of the measurement of the same sample with the help of a lock-in amplifier and an oscilloscope is presented in Figure 4.2. The key difference between the two methods is the ability to measure the recombination time of charge carriers. With the help of a lock-in amplifier, one can measure the change between the dark and steady-state or two steady-states with different excitation. The measured signal is proportional to the charge carrier density, which is equal to the product of the recombination time and the generation rate, as explained in the Theoretical Background section. This means, that without information on the charge carrier density and generation rate, the recombination time can not be obtained from these measurements, but the tendencies of the product of the two quantities can be observed with high accuracy. By evaluating the results of steady-state and transient measurements even more information can be gained regarding the recombination processes, as presented in the next chapter. The hysteretic effect can be observed with a higher detail for the quasi-steady-state measurement due to the higher sensitivity of the measurement. Due to the high sensitivity of the lock-in detection, the same heating protocol leads to an increased amount of measurement points, allowing the observation of phase transitions with a significantly higher detail.

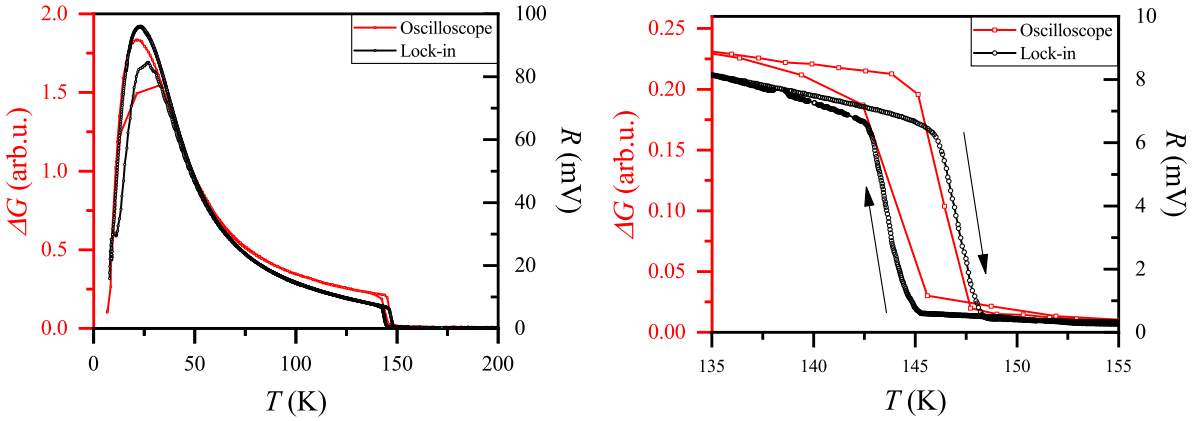

Figure 4.2: Comparison of the measurement conducted with a lock-in amplifier and an oscilloscope. The figure on the right side presents the ability of the two measurement processes to follow the hysteretic effects of phase transition.

I recorded decay curves as presented in Figure 4.3. for all presented samples with the help of the oscilloscope-based version of the measurement setup. I fitted the decay curves in an automated manner with single exponents. The appropriate fitting of the decay curves with a single exponent indicates that the recombination process is dominated by one recombination channel. The characteristic time of the decay process (τ_c) is determined from the exponential fit, and the photoconductivity (ΔG) is represented by the amplitude of the decay curves.

All presented measurements were conducted on samples synthesized by Dr. Márton Kollár and Dr. Endre Horváth. The sample manufacturing process is presented in the Methods section.

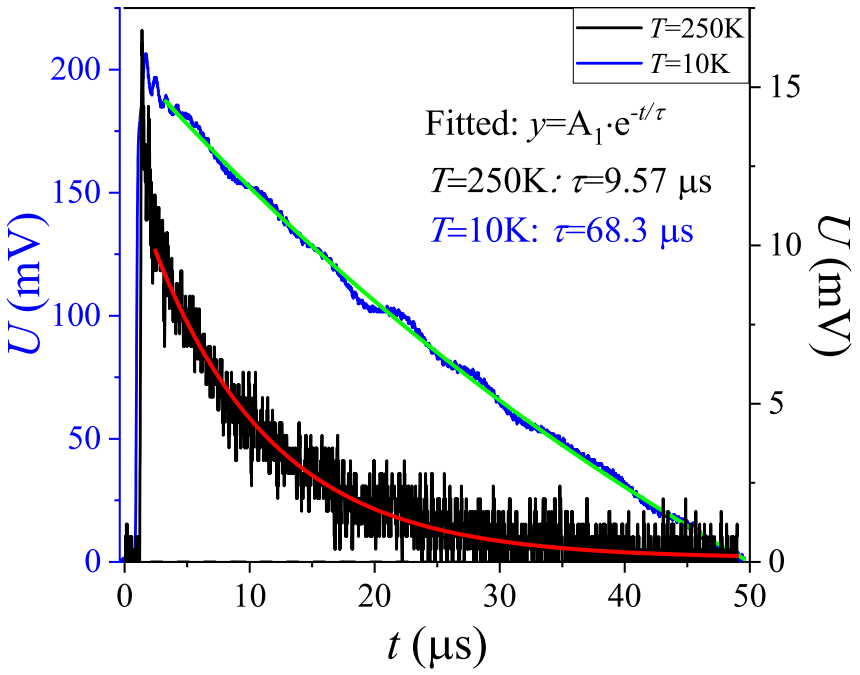

Figure 4.3: The recombination dynamics of photoexcited charge carriers observed through the decay of microwave reflection as a function of time. The red and black curves represent the recorded signals, and the red and green curves are the fitted single exponents. The large digital noise is the result of the relatively poor vertical resolution of the used oscilloscope.

4.2 Temperature dependent charge-carrier lifetime in methylammonium lead halides

The temperature-dependent charge-carrier recombination time and photoconductivity values obtained from microwave photoconductivity decay measurements are presented in Figure 4.4. down to 4 K. All presented measurement sequences were recorded during the heating of the samples. In the temperature range of the measurements, all three parent MHPs undergo a phase transition from orthorhombic to tetragonal, the $MAPbBr_3$ undergoes an additional phase transition between two phases that are tetragonal, while the $MAPbCl_3$ and $MAPbBr_3$ undergo a tetragonal to cubic phase transition as well.

The degrees of freedom of the methylammonium cation change drastically as the temperature is decreased[75–78]. At high temperatures the methylammonium cation may be in any orientation around the halide atom it is connected to. In the tetragonal phase, the methylammonium cation obtains preferred orientations in the lattice but is still moving between these orientations. In the orthorhombic phase, the methylammonium cations become fully ordered, they may be in one of two allowed orientations. Depending on the orientation of these cations either ferroelectric or antiferroelectric domains may emerge[69, 81–84]. Such a ferroelectric ordering of the methylammonium cations may lead to the emergence of a built-in electric field, in the presence of antiferroelectric domains the built-in electric field would not emerge in the

same manner. A built-in electric field helps the separation of excited charge carriers leading to the increase of charge-carrier lifetime and photoconductivity[69, 80, 81].

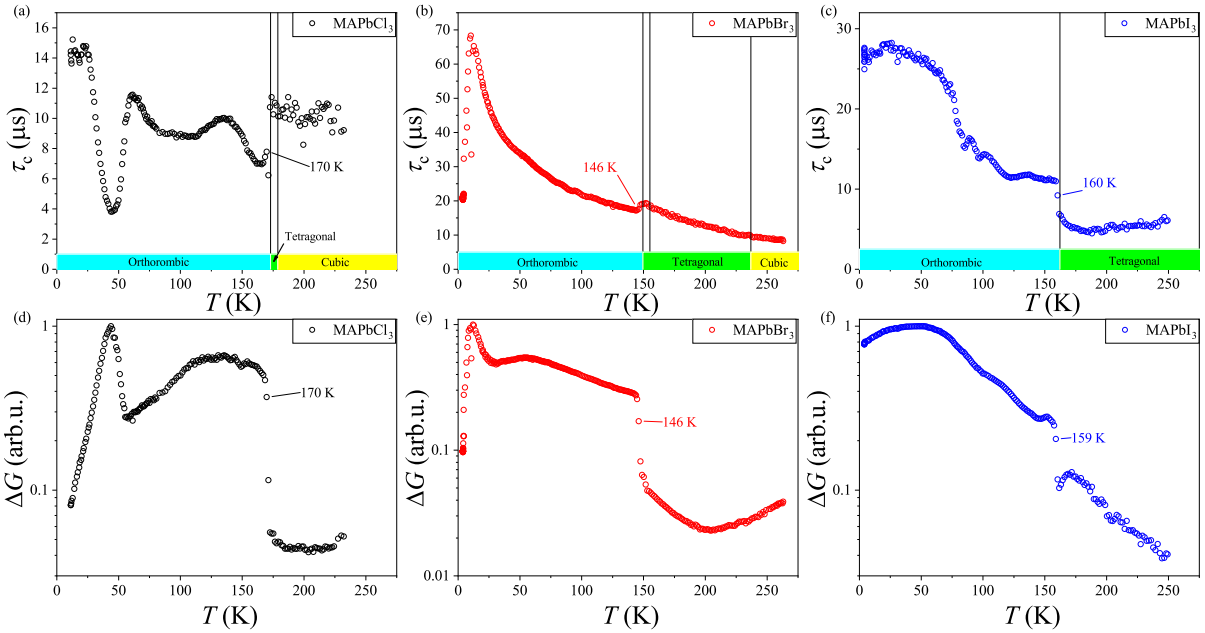

Figure 4.4: charge-carrier lifetime (a-c) and photoconductance (d-f) as a function of temperature for $MAPbI_3$, $MAPbBr_3$, and $MAPbCl_3$ crystals. All investigated samples show maximal values in photoconductivity and ultralong charge-carrier recombination times at low temperatures. The maximal observed recombination time is over 68 μs for $MAPbBr_3$. The vertical lines represent the temperature of phase transitions. All samples show significant changes in both parameters at the orthorhombic to tetragonal phase transition.

According to my observations, the tetragonal to cubic phase transition has no effect on the photoconductivity and charge-carrier recombination time. The orthorhombic to tetragonal phase transition however is found to have a noticeable effect on recombination time and a substantial effect on photoconductivity. The change in photoconductivity at the phase transition from the orthorhombic to the tetragonal phase is a factor of ~ 2.5 for $MAPbI_3$, ~ 6 for $MAPbBr_3$, and ~ 10 for $MAPbCl_3$ crystals. The observed photoconductivity is higher in the orthorhombic phase for all samples than in the tetragonal or cubic phase.

A maximal value is observed in the orthorhombic phase for the recombination time and photoconductivity as well in all parent MHPs. Below the temperature corresponding to the maximal values of ΔG a decreasing tendency is observed. The temperature corresponding to the maximal photoconductivity value shows a dependence on the halide content, the narrow peak shifts to a smaller temperature for $MAPbBr_3$ compared to $MAPbCl_3$. In the case of the $MAPbI_3$ crystal, such a narrow peak is not observed, a broad peak can be seen similarly to the ones observed for the other two parent MHPs. There might however be a similar narrow peak in the photoconductivity of $MAPbI_3$ below the temperature range reachable in this measurement. The presence of such a peak would mean a decreasing tendency in the temperature of the maximal conductivity value as the atomic size of halogens in the material increases. The observed decrease of photoconductivity below the temperature corresponding to the maximal value may be explained by the emergence of antiferroelectric domains in the material. Such regimes would cancel out the

effect of the built-in electric field caused by the ferroelectric ordering. The possible presence of antiferroelectric domains has been predicted[82] but I know of no proof for their existence.

The investigated perovskites show maximal recombination time values in the orthorhombic phase. The three samples possess ultralong recombination time values at cryogenic conditions with the highest recorded recombination time approaching 70 μs for the $MAPbBr_3$ sample. These maximal recombination time values as well as the temperature values corresponding to the maximal ΔG and τ_c values are presented in Table 4.1. The recombination times I present are longer than the previously reported values[145, 181–186] , with the longest in $MAPbI_3$ being 15 μs[181].

	T_{max} (K)	τ_c (μs)	$T_{\Delta G}$ K
$MAPbCl_3$	13	15.2	44
$MAPbBr_3$	10	68.3	12
$MAPbI_3$	26	28.2	48

Table 4.1: Temperature where the maximal recombination time is observed, T_{max}, temperature where the maximal photoconductivity is observed, $T_{\Delta G}$, and the maximal recombination time observed for the three MHPs at the aforementioned temperature, τ_c.

The observation, that the phase transition from tetragonal to cubic phase has no visible effect on charge-carrier lifetime or photoconductivity, supports the previous discussion that the MA ordering causes the change in photovoltaic properties in the orthorhombic phase. The gradual increase in τ_c in the orthorhombic phase with decreasing temperature for the $MAPbBr_3$ and $MAPbI_3$ crystals may be caused by the continuous change in the ordering of MA cations. This loss of movement is drastically different at the two phase transitions since in the orthorhombic phase only two possible orientations remain, leading to a substantial difference in effect on the recombination process and photovoltaic properties.

A small drop is also noticeable at the orthorhombic-tetragonal phase transition for the $MAPbCl_3$ and $MAPbBr_3$ sample. This could be caused by the presence of both phases at the phase transition in the form of domains of material possessing different phase properties. The charge carriers present in the material at this temperature range would encounter an increased amount of domain boundaries resulting in a lower time without the scattering of said charge carriers. The increased number of scattering events leads to the decrease of recombination time. The domains disappear if the temperature is increased or decreased away from the phase transition as the whole crystal obtains the same crystal system. The presence of a small number of domains possessing the tetragonal phase in the temperature range of the orthorhombic phase was reported before[72, 73]. This effect is not present however in the $MAPbI_3$ sample. This may indicate that the reason behind this effect is not the aforementioned possibility but another underlying process that I did not identify.

Due to the first-order nature of the phase transition from orthorhombic to tetragonal phase, a hysteretic effect is observable around the transition temperature. This is caused by the simultaneous presence of the tetragonal and orthorhombic phases in the material in a small temperature region around the phase transition. This effect is presented in Figure 4.5. on the amorphous $MAPbBr_3$ sample detailed in Chapter 4.5. The presented measurement was realized with two different detection techniques utilizing an oscilloscope and a lock-in amplifier. The effect was previously observed by Osherov *et al.*[71]. This observation of the hysteretic effect proves that

around the temperature corresponding to the phase transition domains emerge with different phase properties.

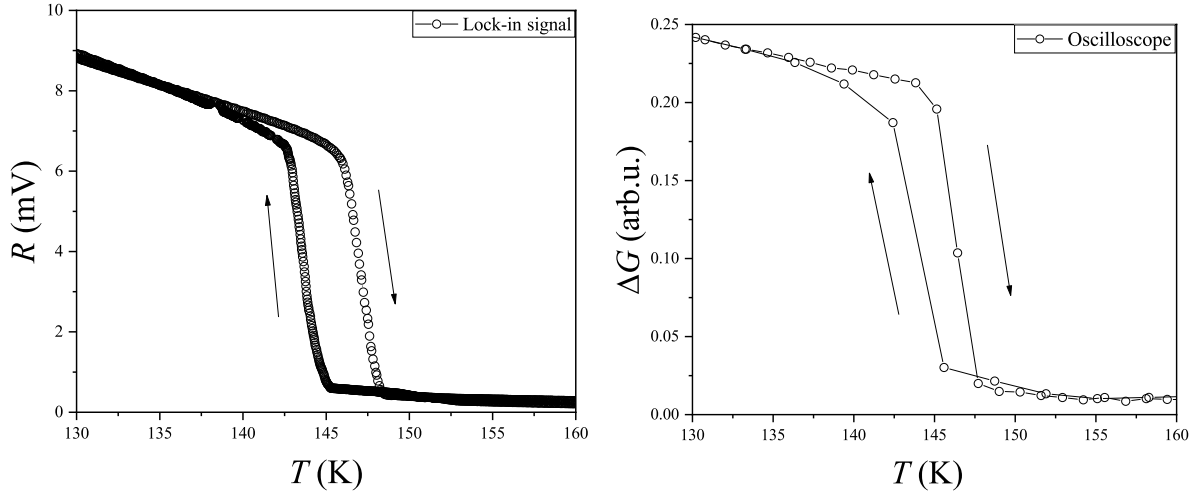

Figure 4.5: Comparison of hysteretic effect around the phase transition measured with a lock-in amplifier (left panel) and an oscilloscope (right panel).

4.3 Reproducibility of the measurements

The reproducibility of any measurement is of utmost importance. For this purpose, I conducted a measurement after the quenched measurement presented in Chapter 4.4 detailing the quenched measurements that consisted of the slow cooling, heating, and repeated cooling of the sample. The temperature dependence of photoconductivity and charge-carrier lifetime for this measurement is presented in Figure 4.6. The results show that the measurement reproduces properly for consecutive measurements. This is only true for slow cooling and heating runs, more precisely the proper reproducibility is present if the slope of the temperature sweep is the same in the consecutive measurements. A quick cooling can cause an increase in the number of domains, or even a difference in the set temperature and the actual temperature of the material.

4.4 Quenching the crystal structure

With the help of temperature-dependent measurements, the connection between structure and the dynamics of photoexcited charge carriers can be observed. By changing the slope of the temperature sweep additional information could be revealed of the phase transitions and their effect on carrier properties. An extreme case for temperature-dependent measurements is the quenching of the material. Quenching is used in a wide area of research and manufacturing and may have a desired or undesired effect. Multiple processes are referred to as quenching. The sudden termination of the superconductivity of part of a superconducting magnet leading to rapid heating and its possible damage is called the quenching of a magnet. The process of decreasing the luminescent intensity of a material is called quenching in luminescent spectroscopy. The mechanism of quenching in this chapter is the definition used in material science.

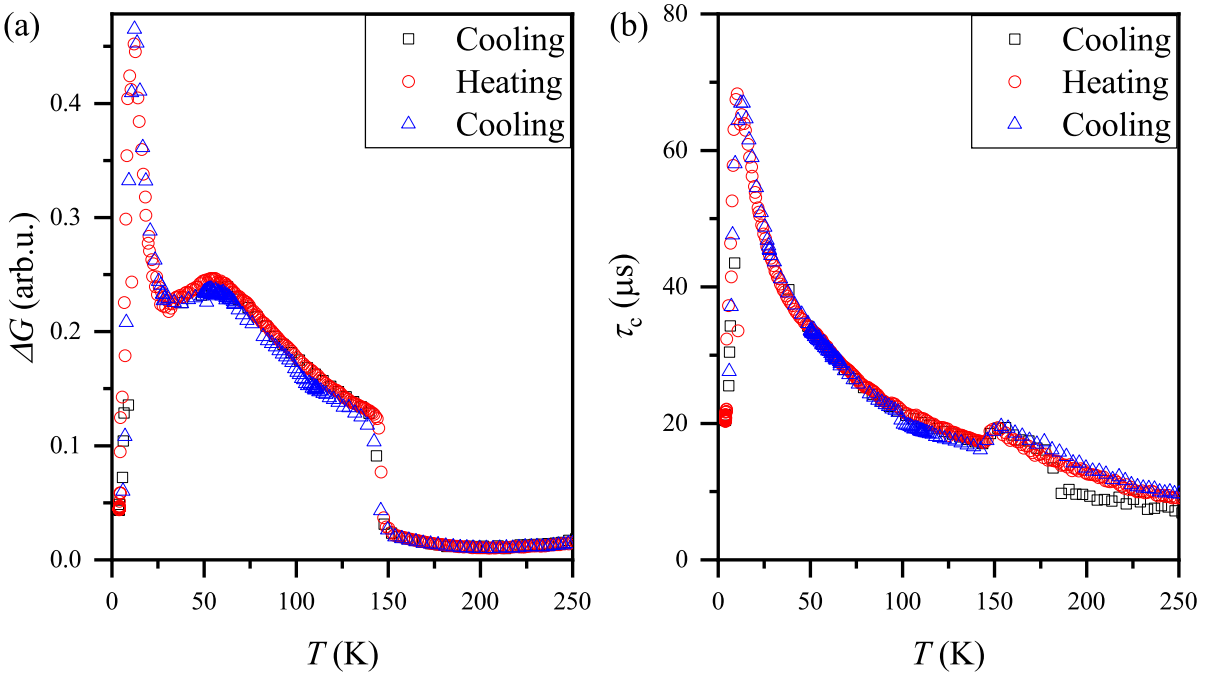

Figure 4.6: Reproducibility of photoconductivity and lifetime for three measurement runs.

Quenching is the rapid cooling of the material resulting in a smaller time window for phase transitions to occur, leading for example to smaller grain sizes. The creation of hardened steel instruments such as swords is achieved through this process by blacksmiths.

The quenching of the material I present herein is realized by quickly cooling the sample to cryogenic conditions through the means of submerging it into liquid helium. This is enabled by the special construction of the cavity-based measurement: this commercial unit is equipped with an easy access cryostat which allows its precooling and placing of a sample within 2-3 seconds directly inside the helium flow. The sample under investigation is a $MAPbBr_3$ single crystal that is cooled through two phase transition in a small timeframe: cubic to tetragonal and tetragonal to orthorhombic. This process may lead to small domains with the same phase property and an increased amount of grain boundaries.

I present the temperature-dependent charge-carrier lifetime and photoconductivity values in Figure 4.7. The measurement was recorded during the heating of the material for consistent measurements. First, the sample was placed in a cavity filled with liquid helium thus achieving fast cooling. After this, the sample was heated up slowly while the photoconductivity decay curves were recorded, followed by the slow cooling and subsequent slow heating of the sample. Since the sample was not removed from the cavity between the two measurements the ΔG values were not normalized.

The charge-carrier lifetime in the quenched sample is significantly lower than in the slowly cooled sample. The maximal lifetime value is more than twice as long in the slowly cooled sample compared to the quenched sample. I propose that this effect is caused by the presence of smaller domains with the ferroelectric ordering of MA cations. If the domains, in which the charge separation is realized by the built-in electric field are smaller, the charge-carrier lifetime is smaller as well. This means that an increased amount of domains in the quenched sample leads to a decreased domain size. The charge carriers excited inside the domain are propelled

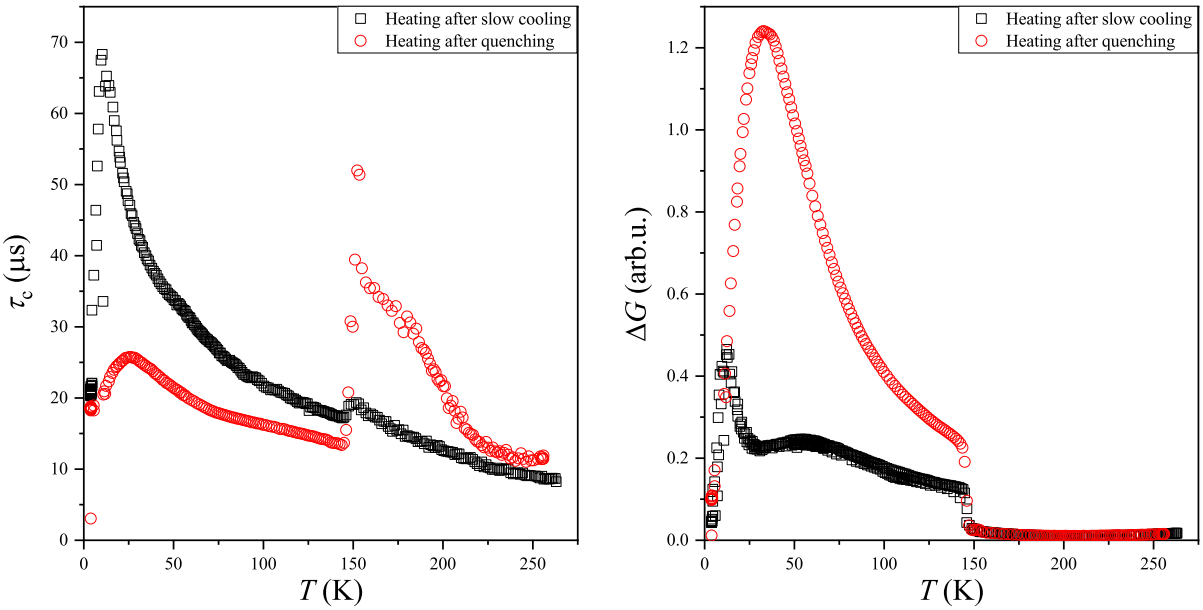

Figure 4.7: Charge-carrier lifetime (left panel) and photoconductivity (right panel) of a $MAPbBr_3$ single crystal as a function of increasing temperature after being cooled slowly and quickly. The charge-carrier recombination time is significantly shorter in the orthorhombic phase in the case of a quenched sample than for the same sample cooled slowly. The trend is the opposite for the photoconductivity, as the photoconductivity observed in the case of the quenched sample is approximately thrice the maximal value of the slowly cooled sample.

apart by the built-in electric field but recombine at the domain boundaries where the opposite charge carriers are propelled from neighboring domains.

The lifetime shows an increased change at the phase transition in the case of the quenched sample compared to the slowly cooled sample and converged towards the lifetime values of the slowly cooled samples as the temperature increased. This effect could be related to the presence of orthorhombic and tetragonal phases at the phase transition and their increased amount of variation and presence due to the small domain size caused by the quenching of the sample. An alternative explanation could be the trapping of charge carriers due to trap states emerging as a result of the quick cooling. It may even be possible that both these effects play a role as trap states may emerge at the boundaries of crystallographic regions, domains, defects, and the increased amount of domains caused by the quenched state of the sample and the parallel presence of tetragonal and orthorhombic phases during the phase transition could cause an increase in charge carrier trapping. With the current amount of information, I can not determine which, if any, of the two possible solutions is the real reason behind the jump in charge-carrier recombination time.

The photoconductivity of the quenched sample is higher in the orthorhombic phase and the same in the tetragonal and cubic phases as the slowly cooled sample. I believe the increased photoconductivity is caused by the presence of smaller domains with ferroelectric ordering. The lower symmetry of the material increases the photoconductivity.

4.5 Effect of Morphology

Different sample preparation methods result in different sample morphology. This morphology may influence the charge-carrier recombination time and photoconductivity. The grain or domain boundaries can act as recombination centers and/or scatter the charge carriers decreasing their lifetime. The size of grains and domains limits the size of the domains with uniform MA cation orientation in the orthorhombic phase if a ferroelectric ordering is achieved.

4.5.1 $MAPbBr_3$

I present the temperature-dependent charge-carrier lifetime and photoconductivity of $MAPbBr_3$ samples in Figure 4.8. The samples were made with differing preparation processes resulting in cubic, irregular, and needle-shaped crystals.

The correlation between the maximal observed recombination time in the orthorhombic phase and the crystallinity is clear in the $\tau_c(T)$ graphs. The highest observed recombination time is recorded for the cube-shaped sample followed by the irregular sample created with the acid-based growth, the needle-shaped samples present the lowest maximal lifetime value. In the orthorhombic phase for the cube-shaped and the irregular sample, the possibility of huge domains of ordered MA cations emerging in the sample is far greater than in the case of the sample consisting of needles. However, the change in the recombination time of charge carriers for the sample consisting of needles is significantly smaller than for the other morphologies. The needle-shaped sample exhibits charge-carrier lifetimes around 20 μs in the whole temperature range. The small change in the lifetime of the sample built up from needles leads to the fact, that in the tetragonal phase, the cube-shaped and irregular sample shows lower lifetime values than the needles. The temperature-dependent lifetime values follow approximately the same tendency for the cube-shaped sample and the irregular sample created with acid-based growth with the cube-shaped sample exhibiting higher recombination times in the whole temperature range. This points towards the cube-shaped sample possessing a higher crystallinity than the irregular sample.

The photoconductivity values are normalized at the same temperature in the tetragonal phase. This way it is possible to compare the photoconductivity values, but it must be stressed that the values are not absolute, the signal is connected to the amount of material in the cavity and the results are only usable to compare tendencies as a function of temperature. The observed change in photoconductivity is similar for the cubic and irregular samples and significantly different in the case of the sample consisting of needles. I believe that the reason behind this is the difference in morphology. The cube-shaped and irregular sample have huge grains and smaller amount of barriers between grains and domains than in the case of the sample consisting of needles. The jump at the phase transition is almost twice for the acid-based growth and close to four times for the cube-shaped compared to the sample consisting of needles.

The orthorhombic to tetragonal phase transition temperature is the same for the cube-shaped sample and the sample created by acid-based growth, both being around ~ 146 K. The sample that consists of needles however shows a slight shift towards lower temperatures, the temperature where the phase transition occurs is at ~ 135 K.

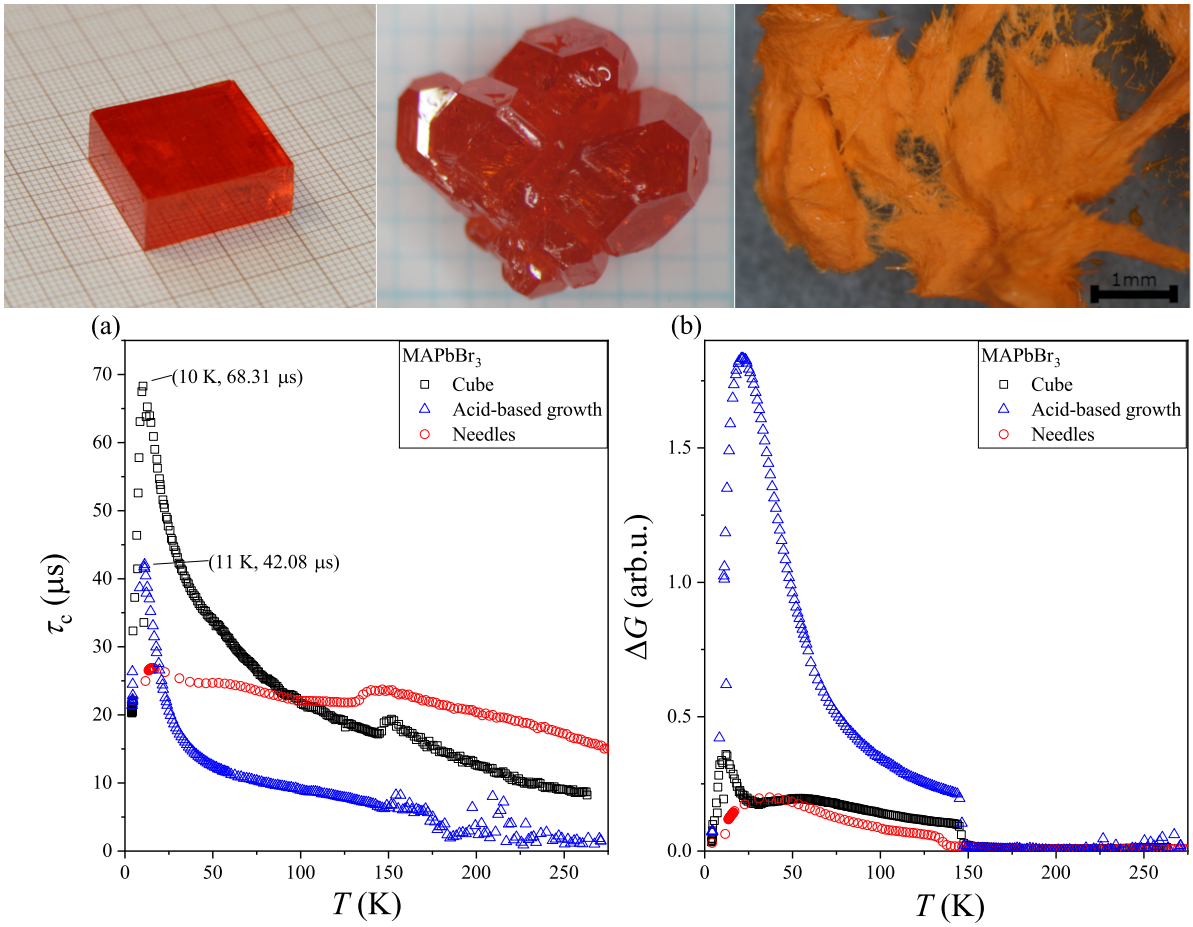

Figure 4.8: Charge-carrier recombination dynamics of three $MAPbBr_3$ samples with varying crystalline morphology. The top panel shows photographs of the three crystals. From left to right: the cubic, amorf (acid-based growth), and needle-shaped samples. Subfigure (a) presents the charge-carrier recombination time, and (b) presents the change in photoconductivity as a function of temperature.

4.5.2 $MAPbI_3$

I present the temperature-dependent charge-carrier lifetime and photoconductivity of $MAPbI_3$ samples in Figure 4.9. The samples were made with differing sample preparation processes resulting in an irregular crystal, a needle-shaped crystal, and a crystal consisting of wires.

The general tendencies are similar to the effects observed for the $MAPbBr_3$ crystals. The charge-carrier lifetime is highest for the irregular sample that possesses the best crystallinity, with the samples consisting of wires and needles presenting lower lifetimes. The samples with worse crystallinity show smaller changes in the recombination time in the temperature range and this subsequently results in a higher lifetime in the tetragonal phase than for the single crystal sample. Interestingly the sample consisting of needles has an increase in lifetime at the orthorhombic to tetragonal phase transition while the other two show a decreasing tendency. This is similar to the effect observed for $MAPbBr_3$ and $MAPbCl_3$ crystals.

The change of photoconductivity as a function of temperature is scaled for the three samples

to fall in line at 200 K in the tetragonal phase. This way - while the results are not comparable since the values are not absolute - the tendencies can be compared. The jump in photoconductivity is also interesting in the case of the sample consisting of needle-shaped crystals, as this is the only sample in our study that had an increase in photoconductivity at the orthorhombic to tetragonal phase transition.

The temperature of the orthorhombic to tetragonal phase transition falls in line for the single crystal and the sample consisting of needles at $\sim$ 159 K, but the phase transition shifts towards smaller temperatures at $\sim$ 142 K for the sample consisting of wires.

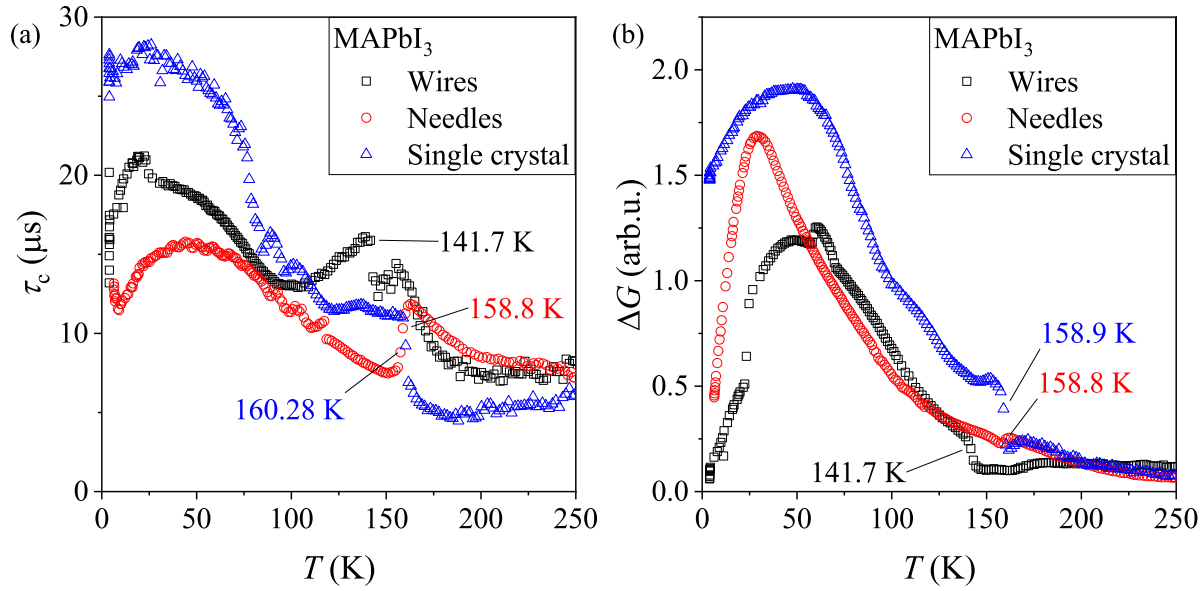

Figure 4.9: Charge-carrier recombination dynamics of three $MAPbI_3$ samples with varying crystalline morphology. Subfigure (a) presents the charge-carrier recombination time, and (b) presents the change in photoconductivity as a function of temperature.

4.6 Conclusions

In conclusion, the observations of the quenched and morphology-dependent measurements support the same observations. The creation of disorder with the help of sample quenching and the decrease of crystallinity lowers the charge-carrier lifetime in methylammonium lead halide perovskite samples. The reason behind this effect is the increase of grain boundaries that can act as recombination centers and can scatter charge carriers thus lowering the recombination time, while also limiting the size of the emerging ferroelectric domains created by the ordering of MA cations at low temperatures. Interestingly increased photoconductivity was observed in the quenched sample and the acid-based growth of an irregular $MAPbBr_3$ sample while the lower crystallinity did not induce such an effect. This may indicate, that a small increase in disorder leads to an increased photoconductivity, while further increase in this manner results in the decrease of photoconductivity.

These results support the observations for the temperature-dependent charge-carrier lifetime and photoconductivity in methylammonium lead halide single crystals. I presented ultralong lifetime values at low temperatures and increased photoconductivity in the orthorhombic

phase in all parent MHPs. I connected these results with the emergence of ferroelectric domains caused by the ordering of MA cations. The observed charge-carrier lifetime values are longer than those found in previous reports of transient microwave photoconductivity decay in $MAPbX_3$ perovskites.

Chapter 5

Charge-Carrier Dynamics in Inorganic Perovskites: Cesium Lead Bromide

In this chapter, I present my research detailing the temperature-dependent charge-carrier recombination dynamics in the cesium lead bromide perovskite. The measurements were conducted with the help of a novel microwave photoconductivity decay measurement system. The system is equipped with a coplanar waveguide that acts as the antenna for both the emission of the probing signal and the detection of the reflected signal, while simultaneously being the cooling pad that the sample is placed on. The measurements were conducted in the $10-300$ K temperature range using a closed cycle, cryo-free cryostat system, thus eliminating the need for liquid helium at the compromise of reaching 10 K only. This single crystal exhibits ultralong charge-carrier recombination times at cryogenic temperatures. I present the power dependence of recombination dynamics at various temperature values and discuss the change in tendencies. I present the temperature-dependent recombination time of charge carriers with both pulsed and steady-state measurement methods. The results are supported by a simulation and a connected theory about charge carrier trapping in shallow traps and a carrier density-independent recombination process after detrapping. According to my findings, the observed ultralong charge-carrier recombination time is caused by the trapping of charge carriers in shallow traps that cause a small portion of generated charge carriers to exhibit ultralong recombination times at cryogenic conditions. The presented measurements were conducted with a microwave reflectometry setup assembled from commercially available components. The measurement is realized with a microwave mixer, and the detection of the reflected microwave signal is done with a high-speed oscilloscope. The cooling of the sample is achieved with a cryo-free cryostat that cools the sample through a cold finger.

The presented observations of the temperature-dependent charge-carrier recombination dynamics in $CsPbBr_3$ single crystals are published in Advanced Energy and Sustainability Research. [O2] The presented measurement setup based on a coplanar waveguide capable of measurements in a wide temperature range with temporal resolution and sensitivity that enables the observation of slow and quick recombination processes during the same measurement sequence is submitted to Review of Scientific Instruments. [O3]

5.1 CPW-based microwave photoconductivity measurement

I developed the microwave photoconductivity decay measurement system presented in Figure 5.1. to measure the temperature-dependent recombination dynamics of semiconductors in a non-destructive manner. The measurement system can detect the recombination process of charge carriers in the $10 - 300$ K range. Due to the high-speed oscilloscope and extensive averaging, it is possible to measure a recombination time domain of 3 orders of magnitude. I was able to measure the change in recombination dynamics in the cesium lead bromide perovskite during the recombination process. These dynamics ranged from the order of 100 nanoseconds in the initial phase of recombination to milliseconds at the end of the decay process. This does not allow for the measurement of the quick decay process dominated by radiative recombination at the beginning of recombination which usually falls below the resolution of the presented setup. This shows that the measurement of transient photoluminescence is a complementary measurement that sheds light on processes not recorded with this measurement.

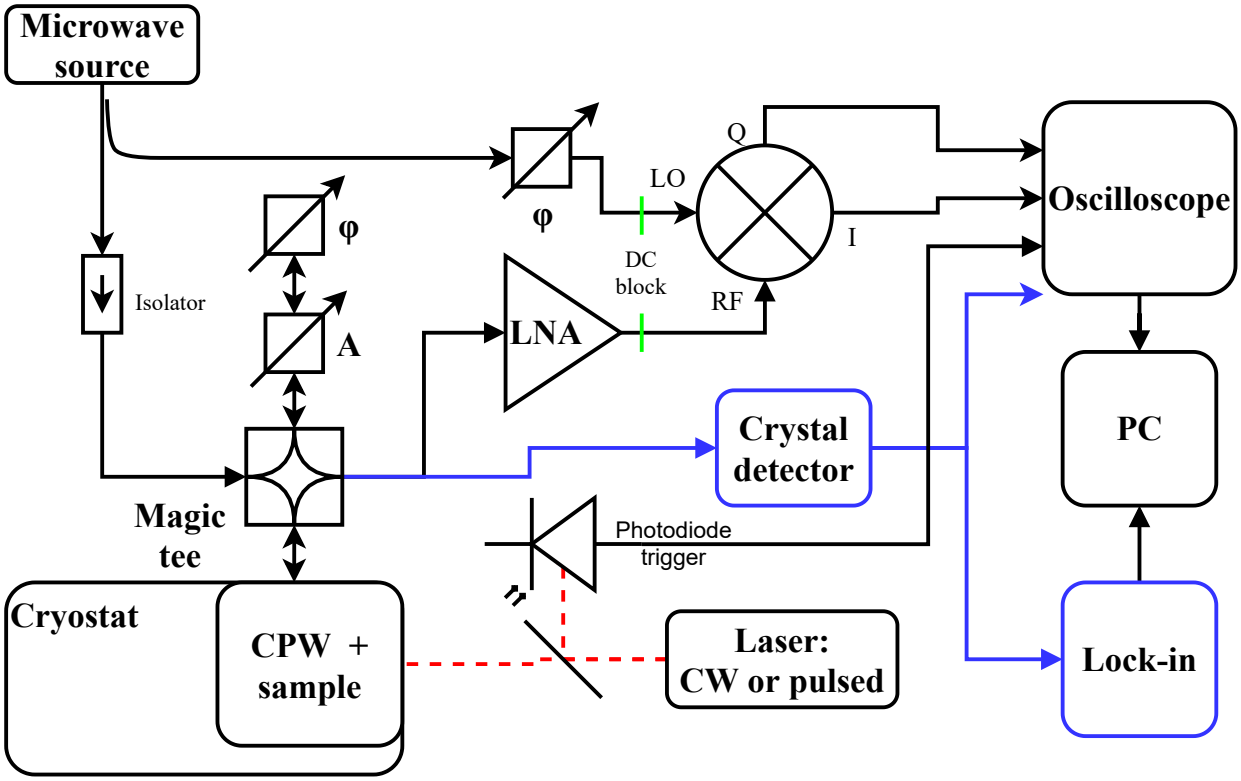

Figure 5.1: Block diagram of the realized measurement system. The device can be operated with CW and pulsed lasers as well and the signal may be recorded with a lock-in amplifier or an oscilloscope.

The basic principle of operation for the measurement system is the detection of the change in reflected microwaves from the probed sample. The probing electromagnetic signal is created with a microwave source that has stable frequency and amplitude. It is possible to tune the frequency of the probing electromagnetic signal in a wide range, this way the penetration depth into the sample of interest can be changed. During the presented measurements the probing radiation was set to 10 GHz. The output signal of the source is split into two, one part going

towards a reference arm while the other part is sent to the sample through an isolator.

A Magic tee is located after the isolator with the purpose of canceling the unwanted, DC reflection coming from the sample in the dark. To do this the signal from the input of the Magic tee is split in two equal parts and sent towards the sample and reference arm. The reference arm is equipped with a phase (φ) and amplitude (A) shifter that can tune the aforementioned properties. The reflection coming from the reference arm from the sample is added together and forwarded toward either an IQ mixer or a crystal detector. By tuning the phase and amplitude of the signal coming from the reference arm the dark reflection of the sample arm can be canceled out by the means of interference as detailed in Chapter 3, leaving only the signal representing the change caused by photoexcitation. This is a useful possibility that prevents the unwanted saturation of the mixer or crystal detector, as a high enough input signal could potentially even damage the instruments.

The sample is placed upon a coplanar waveguide that acts simultaneously as the antenna that emits the probing radiation and receives the reflected radiation. The CPW also doubles as the cooling pad for the sample. The CPW has a metallic surface that is connected to the cold finger of a cryostat and the sample as well, this way realizing good thermal contact between the cold finger and the sample. Due to the good cooling capabilities of the cryostat, the measurement system realized this way is capable of temperature-dependent measurements in the $10-300$ K range.

There are two possible methods for the measurement of the reflected microwave signal in the system. One can either use an IQ mixer or a crystal detector. The IQ mixer is based on the mixing of a reference signal and the signal of interest creating the product of the two signals. The product of the two signals (in accordance with the trigonometric identity) contains components with a frequency equal to the sum and difference of the two input frequencies. By applying a low pass filter only the difference frequency remains, which is close to a DC signal. The I and Q ports of the IQ mixer are the in and out of phase parts of the signal, these can be connected to the inputs of the oscilloscope or the lock-in amplifier. The RF and LO inputs of the mixer are galvanically isolated from the rest of the circuit with DC blocks. This is to prevent ground looping and is realized with the help of plastic sheets placed between SMA-WR90 connectors facing each other and connected with plastic screws.

The crystal detector rectifies the probing signal, allowing for the measurement of signal amplitude while the information locked into the phase of the signal is lost in the process. The crystal detector used in the measurement system works in the 10 MHz $-$ 18 GHz frequency range. The signal obtained with the help of a crystal detector can be measured with an oscilloscope or - in the case of proper optical excitation - with the help of a lock-in amplifier.

With a high-speed oscilloscope, the dynamics of the decay process can be observed through a time-resolved measurement. The decay curves can be fitted with one or more exponential functions. This way the characteristic time of recombination processes is extracted from the time traces. With the help of a lock-in amplifier, the measured signal level will represent the steady state equilibrium determined by the recombination time and generation rate, and the signal level will be proportional to the product of these values. The theoretical background of the time-resolved and steady-state photoconductivity measurement is presented in the chapter detailing the Theoretical Background of the presented samples and methods.

The photoexcitation of the sample is done with a laser that can be either pulsed or continuous wave, depending on the type of measurement the user has in mind. The wavelength of

excitation can be changed easily between 532 nm and 1064 nm but other wavelengths can be easily incorporated as well.

5.2 The microwave photoconductivity decay measurement of $CsPbBr_3$ single crystals

The temperature-dependent charge-carrier recombination time measurements were conducted with the previously described instrument. A 532 nm Q-switched pulsed laser with a pulse width of 10 ns was used for optical excitation with a repetition rate of 200 Hz. For such a pulsed excitation, an illumination of one Sun corresponds to approximately 500 μJ/cm^2.

The measurement of $CsPbBr_3$ single crystals started with the measurement of one small sample of approximately 2 mm $\times$ 2 mm $\times$ 2 mm. During the very first temperature-dependent measurement when I started measuring the material I observed a long recombination time at cryogenic temperatures. Two such relaxation curves are shown in Figure 5.2.

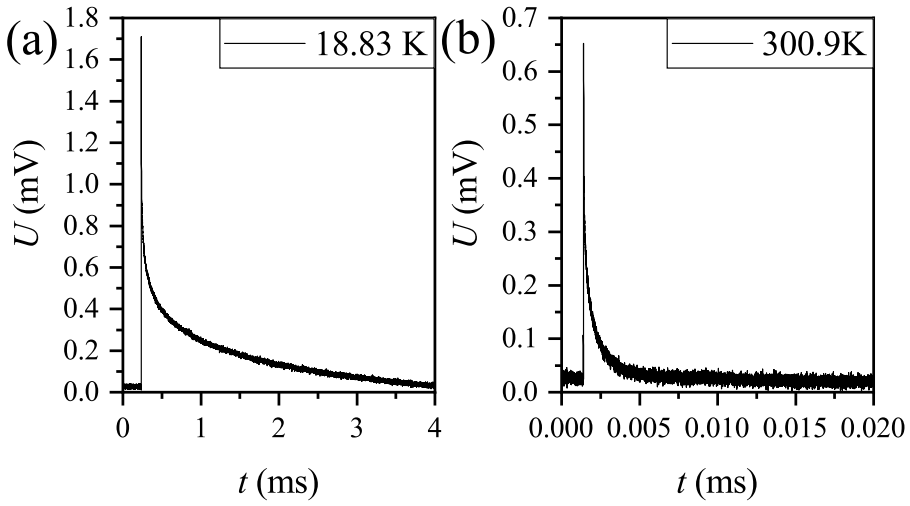

Figure 5.2: First observation of the ultralong recombination time of $CsPbBr_3$ at cryogenic conditions. The relaxations were recorded at 18.83 K in the case of subfigure (a), and 300.9 K in the case of subfigure (b). Note the very different time scales in the two experiments.

The long recombination process present in the $CsPbBr_3$ single crystals was easily observable at low temperatures but as the temperature was increased, the signal level at which this was observable decreased. I developed and optimized the CPW-based microwave photoconductivity decay measurement setup with a low-noise amplifier, an IQ mixer, a balanced bridge, and the high averaging of the data exactly for such measurements where the huge dynamic range of the system is utilized, the recombination process is observable over three orders of magnitude.

The μPCD technique is an ideal method for the measurement of the characteristic time of recombination processes. Still, it cannot differentiate between the measured processes since it can only measure the change of charge carrier concentration in the material and this does not carry any information about the process that changes the carrier concentration. Due to this, transient photoluminescence is a complementary measurement method. By analyzing the decay curve obtained from transient photoluminescent measurements one receives the characteristic time

of radiative recombination. Figure 5.3. shows the transient photoluminescence of a $CsPbBr_3$ single crystal. The measurement was conducted by Hidetsugu Shiozawa at room temperature, the excitation used during the measurement was 405 nm. The results of the fitting of a double exponent are included beside the transient. The luminescent decay time is below 100 ns, leading to the conclusion that the ultralong recombination time observed with the μPCD technique originates from non-radiative recombination processes, namely the Auger and/or SRH recombination process, or the trapping and detrapping of charge carriers.

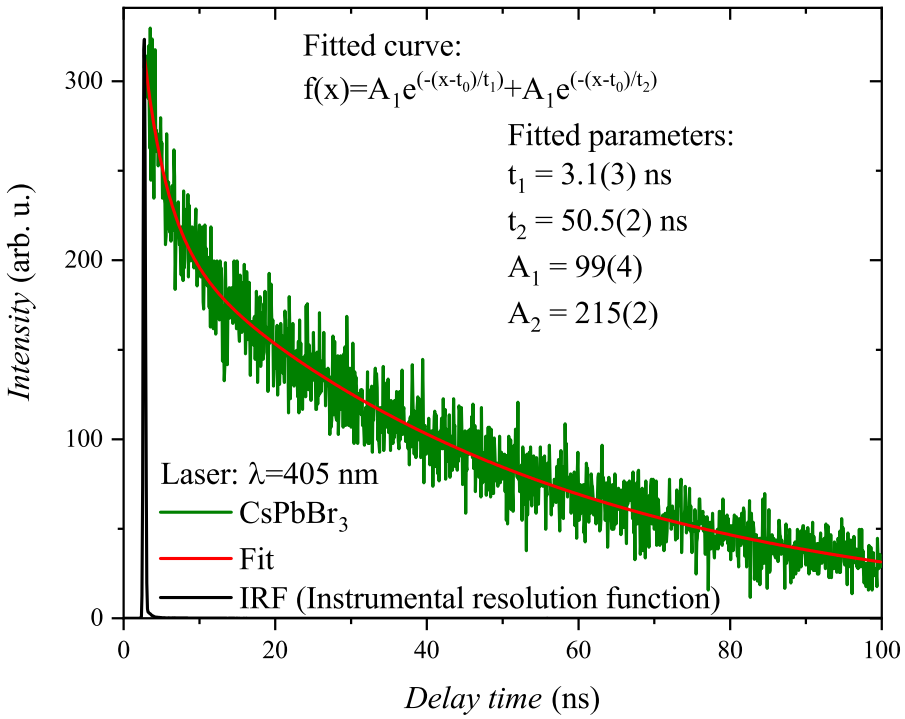

Figure 5.3: Transient photoluminescence measurement of the $CsPbBr_3$ single crystal at room temperature. The measurement was done by Hidetsugu Shiozawa.

5.3 Temperature-dependent microwave reflection in dark conditions

Given that we observe ultralong (beyond 1 ms) recombination dynamics in the reflected microwave signals one possibility could be that it arises from a heating effect of a pulses. Herein, I show my experiments intended to investigate whether this effect could be at play. To rule out the possibility that the measured signal originates from the change in sample temperature I investigated the temperature-dependent microwave reflection of the sample without illumination. The temperature-dependent microwave reflection of the system with and without the sample is presented in Figure 5.6. The measurement was conducted with the reference arm of the Magic tee fully closed. The measurements reveal the non-monotonous nature of the reflection as a function of temperature. Since the signal level connected to the ultralong recombination time is significantly greater than the change in the dark reflection of the sample, it is deduced that the change in sample temperature does not cause the observed recombination time. If it was a

heating effect that would imply that the sample is heated by a few tens of kelvins during each pulse and quickly cooled down afterward. By comparing the decay curves and the obtained recombination time values with the microwave reflection in dark one can also conclude, that the heating of the sample as an explanation for the observed effect would have to be present at specific temperature ranges and with different heating tendencies. If the long recombination time came from the heating of the sample, the tendencies of the recombination dynamics should follow the non-monotonous and nonlinear change of microwave reflection as a function of temperature, which is clearly not the case herein.

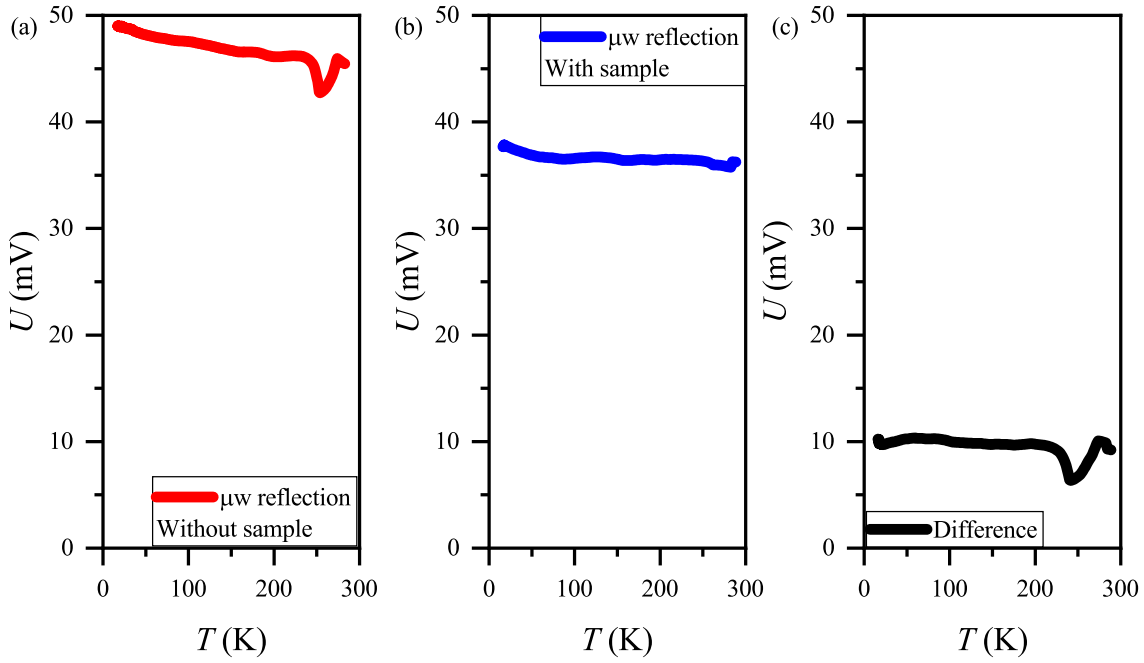

Figure 5.4: The temperature-dependent microwave reflection of the CPW in the dark is presented without a sample in subfigure (a), with the $CsPbBr_3$ sample in subfigure (b), and the difference of these temperature-dependent reflection tendencies in subfigure (c).

According to the presented results placing the sample on the CPW induces an approximately 10 mV change in the microwave reflection, and the temperature-dependent change of microwave reflection in the presence of the sample is below 3 mV in the temperature range of the measurements. By reproducing the same tendencies of charge-carrier recombination dynamics in different-sized samples and samples cleaved from a bigger crystal I further demonstrated, that the observed effect is not caused by sample heating, but rather it is caused by the relaxation process of photoexcited charge carriers.

5.4 Evaluation of the charge-carrier recombination dynamics

I measured the microwave photoconductivity decay curves of $CsPbBr_3$ single crystals in a wide temperature range between 20 K and room temperature. Examples of the measurements

are presented in subfigures (a) and (c) of Figure 5.5. At the beginning of the recombination process, a quick decay is observable at all temperatures. The characteristic time of this quick decay process is measured to be below 1 μs. The derivative of the decay curve changes continuously. One can observe a maximal recombination time value of over 1 ms at cryogenic conditions and about 100 μs at room temperature. While this ultralong charge carrier recombination process may be caused by the quality of the measured crystals, I believe this to be rather due to the outstanding capabilities of the developed system that allows for the observation of the recombination process even at low signal levels. I believe the capabilities of the system allowed the observation of such a large recombination time orders of magnitude longer than most previous reports [97, 141, 187]. The room temperature recombination time reported herein is more than three times longer than the longest recombination time of 33.6 μs found in the literature.

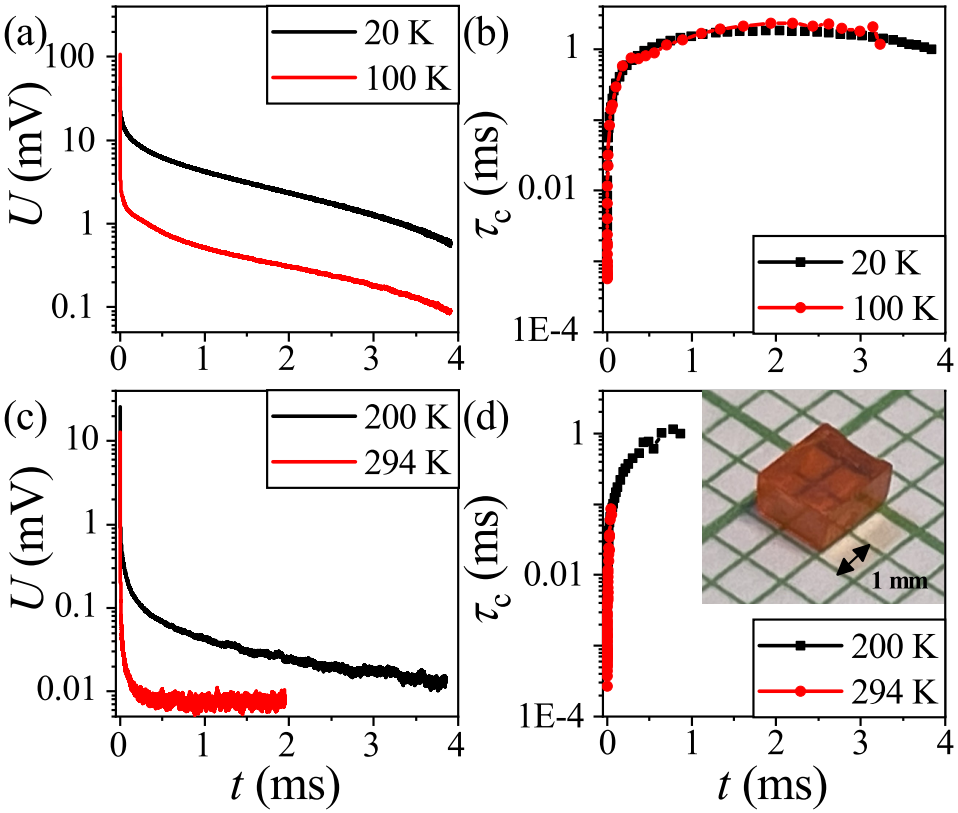

Figure 5.5: The reflected microwave voltage as a function of time during the relaxation process at four different temperatures between 20 K and room temperature are presented in subfigures (a) and (c). The recombination time values as a function of time obtained through the analysis presented in the text for the same relaxation processes are shown in subfigures (b) and (d). The inset in subfigure (d) shows the measured single crystal sample.

Since the recombination time changes significantly during the recombination process, the fitting of the data with a few exponents would not be representative of the decay process. In principle the evaluation of the reported recombination times is done with the numerical derivative of the recorded signal. However, due to the noise of the signal, the obtained values would not be accurate, and the noise level would be relatively high. To solve this problem a fitting method that starts with the calculation of noise and maximal signal level is used. After these are

obtained, the signal is segmented into bins. The number of bins is typically between 50 and 200. The values in a single bin are averaged together, resulting in a single data point per bin. This method essentially results in the adaptive smoothing of the measurement data for a noiseless evaluation process. The data points obtained this way are then used to calculate the numerical derivative of the signal, resulting in the recombination time values. It is possible to use different binning methods to reach the best signal-to-noise ratio during the evaluation process. The possibilities include not only the linear distribution of data points along the x-axis but a distribution along the y-axis that results in fewer points in the quick recombination region where the signal is not as noisy as at the end of the decay curve where the averaging of more data points leads to a more reliable evaluation process. Another method would be the logarithmic binning of data points along one axis, which could increase the averaging at the region of the slow process, even further increasing the signal-to-noise ratio. The recombination time values obtained with this process as a function of time are shown in subfigure (b) and (c) of Figure 5.5. The binning of these measurements with a logarithmic distribution along the y-axis resulted in a 60 ns bin size in the beginning and a 80 μs bin size at the end of the relaxation.

The method of binning the data points and utilizing a numerical derivative-based calculation for the evaluation of charge-carrier recombination time during the recombination process was proposed and implemented by Dávid Krisztián.

5.5 Temperature dependent recombination dynamics in the $CsPbBr_3$ perovskites

The temperature-dependent charge-carrier recombination dynamics are presented in Figure 5.6. Subfigure (a) shows the recombination time of charge carriers as a function of the detected signal level. The reflected microwave signal is proportional, under appropriate assumptions, to the charge carrier density in the material. The recombination process starts with a quick decay, that lengthens from this point. In the case of low-temperature processes, a plateau is present after an initial quick recombination. This plateau is above the 1 ms recombination time value. At higher temperatures, this constant, long recombination process is not observable. To make sure, that the effect was not a measurement error, I measured multiple samples to see the recombination dynamics at different temperatures.

The recombination time as a function of the signal level at different temperatures for two other samples is presented in Figure 5.7. The other two samples were sized 2x2x1 mm and 7x7x3 mm. The recombination dynamics at different temperatures for the two samples show very similar tendencies as the one presented in 5.6. (a).

The maximal value of the decay process is presented in subfigure (b) of Figure 5.6. This value indicates the change in conductivity caused by optical excitation as a function of temperature. The curve has a maximal value around $45 - 55$ K and a small change around 220 K. The presence of the maximal value at low temperatures and the small change around 220 K reproduced for several runs, multiple samples, and different excitation levels. The material has no known phase transition in the temperature range of the presented investigation, it is in the orthorhombic phase below 361 K[94].

The maximal value in the amplitude around 50 K may be caused either by an increase in photoconductance or photogeneration efficiency. I am aware of no changes to the structure or

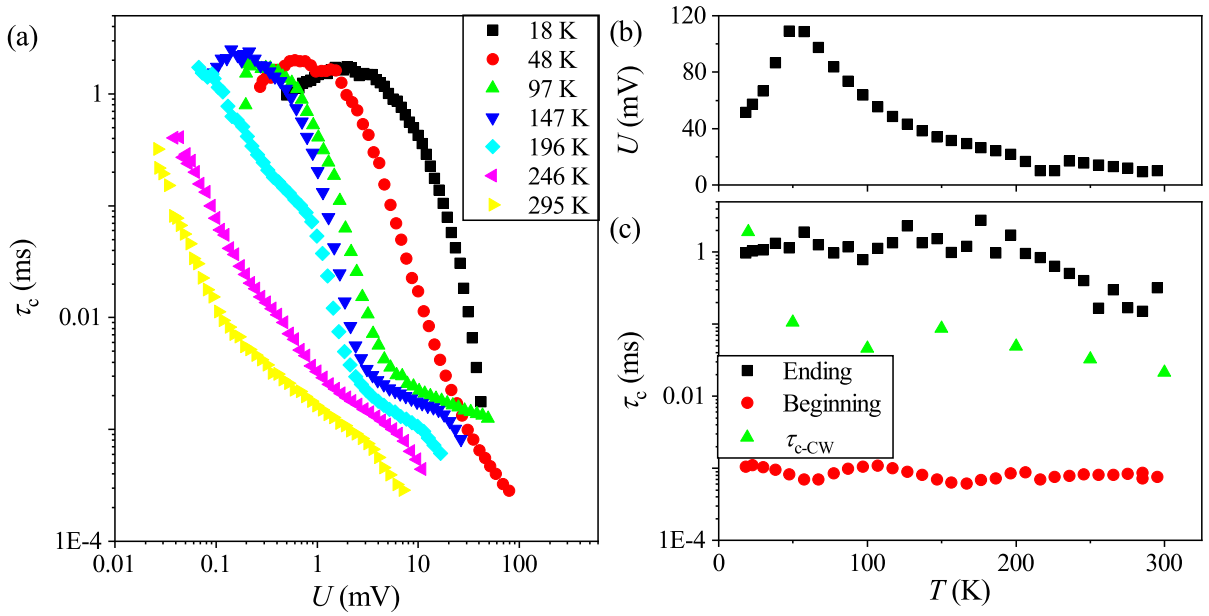

Figure 5.6: Subfigure (a) presents the charge-carrier recombination time as a function of reflected microwave signal of a $CsPbBr_3$ single crystal at 7 temperature values between 18 K and room temperature. The maximal value of the reflected signal is presented in subfigure (b). The recombination time measured at the beginning and end of the recombination process as well as the recombination time obtained from the steady state measurement is shown in subfigure (c). All measurements were conducted at an average irradiance of approximately 399 μJ/cm^2.

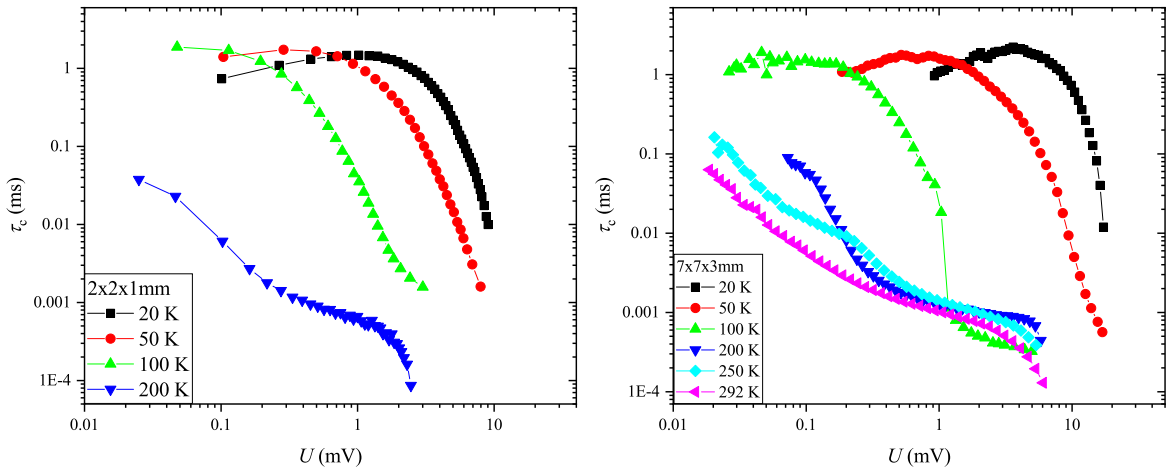

Figure 5.7: Charge-carrier recombination time as a function of reflected microwave voltage at different temperature settings for two $CsPbBr_3$ samples.

electronic properties of the material in the temperature range that could cause such a maximal value. The recombination time shows no noticeable change around the same temperature, pointing to the observation that there are no phase transitions of any kind at the temperature range in question. The origin of the effect around 220 K is also unknown, nevertheless there are reports of anomalous behavior in this temperature range in the literature. The thermal emission from trap levels[64] that is believed to be caused by Pb-Br antisites in the material[95] is around this

temperature value. Another observation found in the literature is the anomalous behavior of the dielectric function around 220 K[188]. These reports and the reproducibility of the change suggest, that there is a yet unknown physical explanation for the effect around 220 K.

The beginning and ending charge-carrier recombination times are presented in subfigure (c) of Figure 5.6. as well as the recombination time values obtained from a measurement conducted with continuous wave excitation. The beginning and ending recombination times are obtained by taking the first and last recombination time values from the evaluation process. The ending recombination time is not evidently the longest recombination time obtained during the evaluation process as shown by the low-temperature decay dynamics presented in subfigure (a) of Figure 5.6. At the end of the recombination process, one can observe recombination times around 1 ms from the lowest temperatures up until around 200 K, at which temperature the recombination time starts to decrease as the temperature increases. The beginning of the recombination process does not display a change similar to the end of the process, there is a small fluctuation of the recombination time value around 1 μs. The recombination time at the beginning of the recombination process is about an order of magnitude higher than the value measured by the TRPL technique at room temperature.

It should be noted that while the long recombination time process is observable even at room temperature thanks to the measurement system, the signal level where these recombination times are present drops significantly from 20 K to room temperature. This means that the charge carrier concentration at which level these recombination times are observed drops significantly. An explanation for this could be the change in the equilibrium occupation of trap states as a function of temperature. The occupation of shallow traps decreases as the temperature increases. In Figure 5.8. another measurement run is presented on the same sample with significantly higher resolution in the temperature sweep and lower averaging of the measured photoconductivity decay curves. The change in averaging leads to a decrease in signal-to-noise ratio causing the measured recombination time at the end of the relaxation process to disappear in the noise of the measurement. The change in recombination dynamics is observed in the same regime, the long recombination component decreases above 200 K, but the slope of the decrease is different. By the end of the process, the measured recombination time at the beginning and end of the process is almost the same. This result emphasizes the importance of sensitivity during the measurement of cesium lead bromides, as the long recombination process at high temperatures is only noticeable with the proper dynamic range of the measurement system and a suitable analysis method.

The photoresponse of semiconductors can be evaluated with the help of continuous wave excitation as well. In real-life situations the solar cell materials do not generate power with the help of pulsed excitation but with the continuous wave excitation of the sun. The CW measurements are presented in subfigure (c) of Figure 5.6. The measurements were conducted at approximately one Sun irradiance. The steady-state measurement of recombination time requires the calibration of the measurement system, since the steady-state charge carrier density is the product of generation rate and recombination time in the steady state, $\Delta n_{\mathrm{CW}} = G_{\mathrm{CW}} \cdot \tau_{\mathrm{c,CW}}$. The $\tau_{\mathrm{c,CW}}$ value is related to the effective recombination time at the steady-state charge carrier concentration, Δn_{CW}, and is the proportionality factor between the generation rate and the carrier concentration. Since the generation rate is unknown without the precise measurement of temperature-dependent optical absorption and the connection between charge carrier density and reflected microwave voltage is not calibrated the comparison of the CW and pulsed

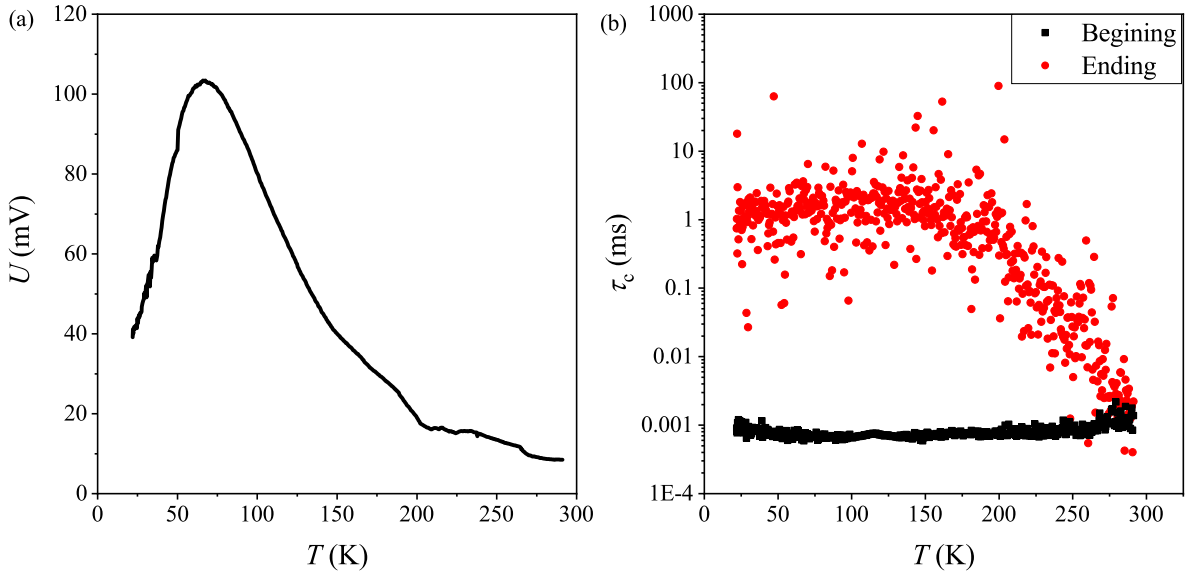

Figure 5.8: Measurement of the maximal value of the decay curve in subfigure (a) and charge-carrier recombination time at the beginning and end of the recombination process in subfigure (b) as a function of temperature with a higher resolution in the temperature sweep. The averaging of TRMCD curves was lowered to decrease the time needed for the measurement. The subpar signal-to-noise ratio leads to higher standard deviation for the τ_c values and the inability to measure the end of the recombination process above 200 K.

measurement needs an overlapping value. This is provided by the matching of average power between CW and pulsed measurements. If the power of the exciting lasers is the same, then the connection between generation rates, pulse width, and frequency of the pulsed laser is:

$$G_{\text{pulse}} = \frac{1}{t_{\text{pulse}} f_{\text{pulse}}} \cdot G_{\text{CW}}, \tag{5.1}$$

Since we know the pulse width to be $t_{\text{pulse}} \approx 10$ ns with a repetition rate of $f_{\text{pulse}} = 200$ Hz we only need the generation rate during pulsed and CW measurements. As explained in the Theoretical Background Chapter, the charge carrier concentration following pulsed excitation is $\Delta n_{\text{pulse}} = G_{\text{pulse}} t_{\text{pulse}}$ if the pulse width is significantly shorter than the recombination time of charge carriers, since then the recombination during excitation is negligible. By substituting into Equation 5.1, one obtains the connection between charge carrier densities:

$$\frac{\Delta n_{\text{CW}}}{\Delta n_{\text{pulse}}} = f_{\text{pulse}} \cdot \tau_{\text{c,CW}}, \tag{5.2}$$

If the measurement is conducted in the regime where the connection between the charge carrier density of the two measurements is linear with the microwave reflection, meaning $U_{\text{pulse}} \propto \Delta n$ is proportional with the same proportionality in the two measurements, then the following will be true:

$$\frac{U_{\text{CW}}}{U_{\text{pulse}}} = f_{\text{pulse}} \cdot \tau_{\text{c,CW}}, \tag{5.3}$$

where U_{pulse} is the maximal measured voltage value of the TRMCD measurement and U_{CW} is the reflected microwave voltage recorded during the steady-state measurement. By simply expressing the $\tau_{\text{c,CW}}$ value from this equation one can easily compare the effective recombination time values of the CW measurement with the recombination time of the pulsed measurements.

The steady-state recombination times obtained from this evaluation method fall between the minimal and maximal recombination times of the TRMCD measurements. $\tau_{\text{c,CW}}$ is over 1 ms at 20 K, decreases from this value as the temperature is increased to approximately 100 μs, and starts to decrease slightly at 200 K following the trend of the pulsed measurement. The fact that the effective recombination time values obtained through the continuous wave measurement fall between the first and last recombination time values of the pulsed measurements supports the observations of the pulsed measurement, as the $\tau_{\text{c,CW}}$ values would be vastly different if the pulsed measurements were the recordings of a measurement artifact.

5.6 Trapping of charge carriers: model, simulation, and the explanation for ultralong charge-carrier recombination times

The investigation of recombination dynamics as a function of excitation is a general way of probing the recombination time of charge carriers as a function of carrier density. The radiative, Auger, and SRH recombination processes have distinct dependences of charge carrier density that change between two functions depending on whether the system is in the low or high injection limit, as presented in the Theoretical Background Chapter. If the material possesses no significant charge carrier trapping effect caused by shallow traps, the connection between carrier density and recombination time is the same at all excitation levels. This means, that the measurement of photoconductivity decay with different excitation values probes different sections of the same $\tau_{\text{c}}(\Delta n)$ function.

I conducted the excitation-dependent measurement of charge-carrier recombination dynamics at six different temperatures as presented in Figure 5.9. The results show, that the recombination dynamics do not fall on the same curve for the increasing excitation values but shift towards higher reflected microwave signals, except for the highest excitations used during the study. The general tendencies of the $\tau_{\text{c}}(U)$ curves observed during the measurement are approximately the same at the given temperatures but change from temperature to temperature, as seen in the previous section in Figure 5.6. The excitation-dependent results support the theory, that the cause for the observed ultralong charge-carrier recombination time is the capture and emission of charge carriers in shallow traps.

In Figure 5.9. the curves do not shift to higher charge carrier density values for excitation above the one Sun illumination. This could be either because of the nonlinearity of the connection between the charge carrier density and the detected microwave voltage, or because of a saturation effect caused by the filling of trap states. If the effect is caused by the saturation of trap states an estimation can be made for the trap state density in the sample. If a sample volume of $V = 0.004$ cm^3 absorbes a pulse energy of ≈ 73.8 μJ and we assume a quantum efficiency of 100%, the excited charge carrier density is $\Delta n \approx 10^{16}$ 1/cm^3. The trap density values found in the literature [64] are similar to the estimated trap density obtained from this calculation.

To recreate the effect shown in Figure 5.9. I created a simulation that includes shallow

trap states. By reproducing the experimental results with the simulation of the charge carrier recombination processes I intend to uncover the mechanisms behind the observed ultralong recombination time.

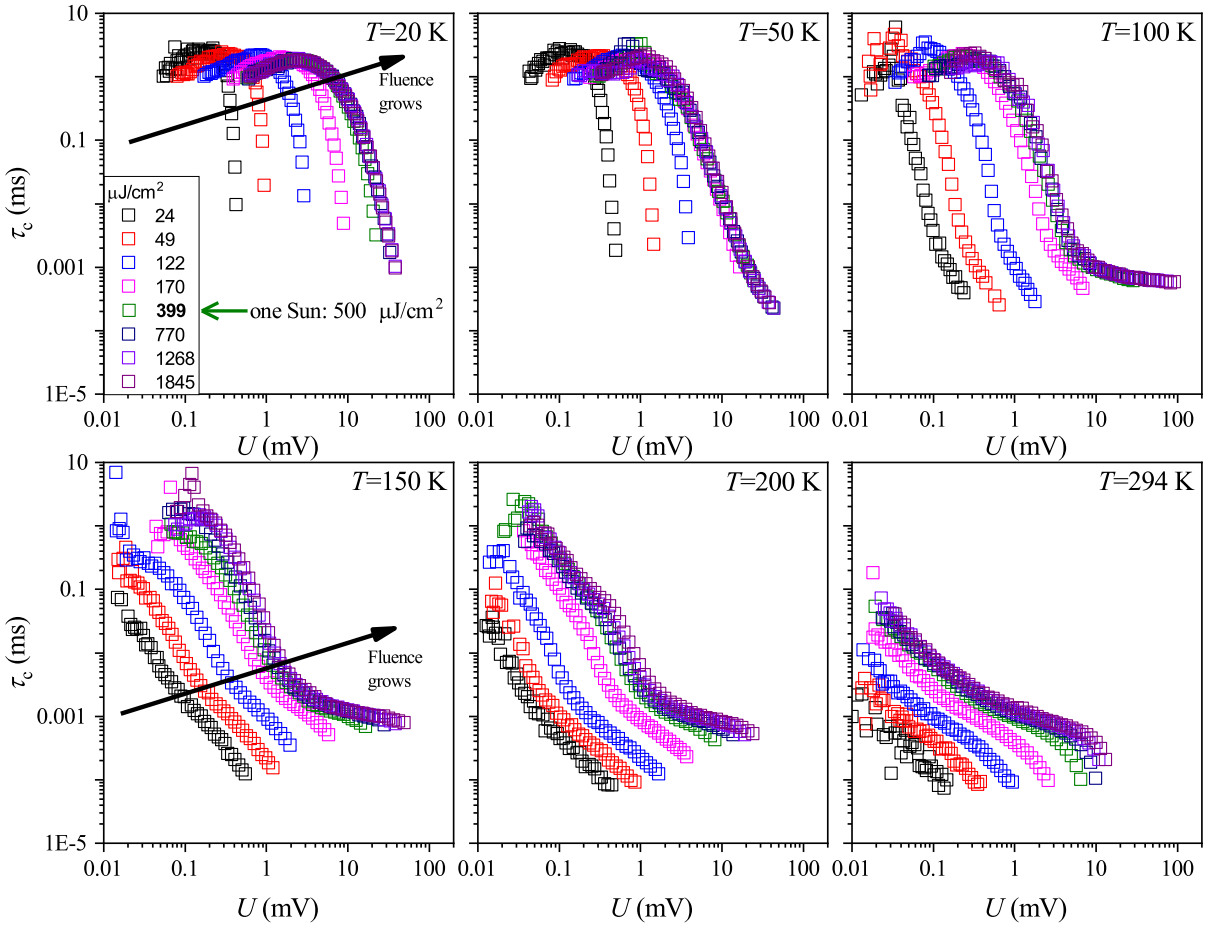

Figure 5.9: Charge-carrier recombination time of the $CsPbBr_3$ single crystal at 6 different temperatures with various excitation levels. The recombination time values are shown as a function of reflected microwave voltage. An arrow on the graphs corresponding to 20 K and 150 K temperatures shows the increasing fluence of the excitation settings.

The band diagram used during the simulations is presented in Figure 5.10. The model includes a shallow and a deep trap state. Shallow traps are generally close to either the conduction or valence band, and can only capture and emit one type of charge carrier. The capture and emission rate of these states is dependent on the temperature of the system. Deep traps are located further away from the conduction and valence band. These are the states responsible for the SRH process. These states can capture and emit both electrons and holes. A detailed description of the SRH process is given in the Theoretical Background Chapter. The annotations on the bandgap for the processes represent the emission and capture of charge carriers. The emission is denoted with "E", and capture is represented by "C". The subscript indicates whether a hole or an electron is captured or emitted, denoted by "h" and "e" in the lower index. After indicating the carrier type, the process is also noted as "trap" and "SRH". In the following, I present two simulations, that include one or both of these processes.

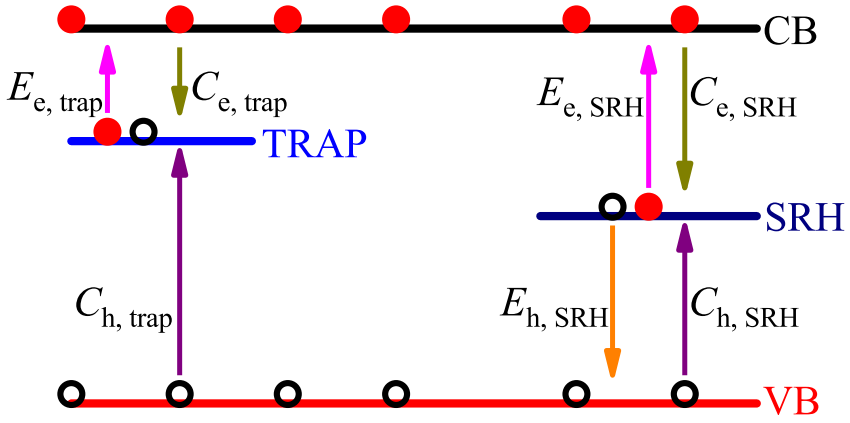

Figure 5.10: Band model of $CsPbBr_3$ with the escape and capture processes noted in the figure. The band model used here consists of a trap and an SRH state besides the valence and conduction band.

I simulated the recombination process with different starting excited charge carrier density values to simulate the excitation dependence of the recombination process presented in Figure 5.9. The first model I used to simulate the recombination process only included one trap state with density n_{T}, that can capture electrons from the conduction band with a capture rate $C_{\text{e,trap}}$, emit them into the conduction band with an emission rate $E_{\text{e,trap}}$, and it can capture holes with a capture rate of $C_{\text{h,trap}}$. This model only contains one recombination channel, the subsequent capture of an electron, and a hole in the same trap state. The simulated recombination dynamics of this model as a function of excited charge carrier density for 4 different starting excitation values is presented in subfigure (a) of Figure 5.11. The process is simulated with the help of a set of rate equations that are as follows based on the rate equations presented in the literature[189]:

$$\begin{aligned}
\frac{\mathrm{d}n}{\mathrm{d}t} &= -C_{\text{e,trap}}\,(N_{\text{T}}-n_{\text{T}})\,n + E_{\text{e,trap}}n_{\text{T}},\\
\frac{\mathrm{d}n_{\text{T}}}{\mathrm{d}t} &= +C_{\text{e,trap}}\,(N_{\text{T}}-n_{\text{T}})\,n - E_{\text{e,trap}}n_{\text{T}} - C_{\text{h,trap}}n_{\text{T}}p,\\
\frac{\mathrm{d}p}{\mathrm{d}t} &= -C_{\text{h,trap}}n_{\text{T}}p.
\end{aligned} \tag{5.4}$$

It should be noted, that the charge neutrality dictates $p = n + n_{\text{T}} + n_{\text{SRH}}$ and that the dimensions of the capture and emission rates are different. The presented model ignores the radiative and Auger recombination processes. The rate equations present the trapping and emission of electrons, but the model can be easily modified to represent the capture of holes.

The emission and capture rates were fixed for the simulation as $C_{\text{e,trap}} = 10^6$, $C_{\text{h,trap}} = 10^3$, and $E_{\text{e,trap}} = 0$. This means that the emission of electrons does not occur, the electrons are trapped in the trap state until the capture of a hole from the valence band when the charge carriers recombine. During the simulation the recombination times are calculated with the help of the rate equations, the simulation was done for 4 different initial charge carrier density values, 3 below the trap concentration and one above it. The $\tau_{\text{c}}(n)$ curves that are presented in subfigure (a) of Figure 5.11. show a shift towards higher concentrations as the initial value increases but

do not show the constant recombination dynamics as seen in the power-dependent measurements. The trapping of charge carriers causes the shift. Since the capture rate of one charge carrier is orders of magnitude above the other, for the three curves with initial carrier density below the trap density the electrons are quickly captured during an initial process that is followed by a process with different slopes where the capture of holes determines the recombination time. This also means that the initial decrease in free charge carrier density is not mainly caused by the recombination process but by the capture of electrons. The $n(t=0)=2$ simulation has an additional region in the recombination process. This is caused by a region in the recombination process when the trap states are already filled but there are still free electrons and holes. These results shed light on some of the effects but do not reproduce the constant τ_c values caused by the trapping of charge carriers. To reproduce this effect I expanded the simulation with further processes.

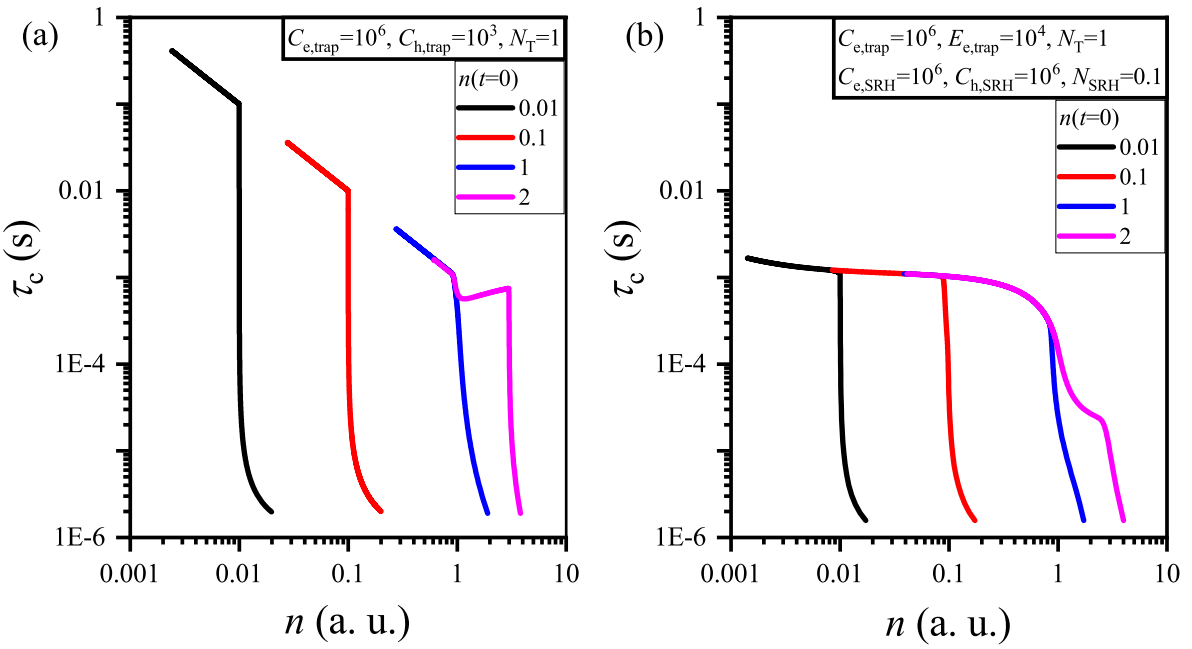

Figure 5.11: Subfigure (a) shows the recombination dynamics with only one recombination process. The process is a trap state that can capture electrons and holes with different capture rates. The recombination process happens when a trap state captures charge carriers of both types. (b) shows the carrier recombination time as a function of carrier concentration with a shallow and a deep-level trap included in the model. It should be noted, that the x-axis represents the density of free electrons and holes, while the $n(t=0)$ initial excitation represents the excitation of electron-hole pairs. This means that $n(t=0)=1$ excites 1 a.u. electrons and 1 a.u. holes that lead to an initial value of $n=2$ in the x-axis.

The second presented model includes two trap states, a deep and a shallow trap. This simulation presents the recombination process, where charge carriers can be trapped inside a shallow trap and they can be emitted back into their original band. The recombination channel is the deep level trap that realizes a Shockley-Read-Hall recombination process. The SRH process is mainly independent of charge carrier density in a wide range, changing between two recombination time values for the low-level injection and high-level injection limit[132]. The observed constant recombination time values are reminiscent of this process mainly independent of the

carrier density. To achieve this, one has to include a second trap state into the rate equations presented in Equation 5.4, and the rate equations become the one presented in Equation 5.5.

In this simulation the trapping of charge carriers limits the recombination process, as in the beginning of relaxation the charge carriers may be trapped in the shallow trap and recombined through the deep trap, but once all charge carriers of one kind are trapped or recombined the recombination process is limited by the depopulation of charge carriers from the trap states. In this simulation, the capture of electrons into the shallow trap state is $C_{\mathrm{e,trap}} = 10^6$, their emission from the trap state is $E_{\mathrm{e,trap}} = 10^4$, the capture of holes in the trap state is zero, the capture rates of charge carriers into the SRH state are $C_{\mathrm{e,SRH}} = 10^6$ and $C_{\mathrm{h,SRH}} = 10^6$, and the emission from the SRH state is set to zero. I found that the constant τ_{c} tendencies only emerge if $N_{\mathrm{SRH}} \ll N_{\mathrm{trap}}$, therefore, the concentration of the shallow trap state is $N_{\mathrm{T}} = 1$, and the concentration of the SRH or deep level state is $N_{\mathrm{SRH}} = 0.1$.

$$
\begin{aligned}
\frac{\mathrm{d}n}{\mathrm{d}t} &= -C_{\mathrm{e,trap}}\left(N_{\mathrm{T}} - n_{\mathrm{T}}\right)n + E_{\mathrm{e,trap}}n_{\mathrm{T}} + E_{\mathrm{e,SRH}}n_{\mathrm{SRH}} - C_{\mathrm{e,SRH}}\left(N_{\mathrm{SRH}} - n_{\mathrm{SRH}}\right)n,\\
\frac{\mathrm{d}n_{\mathrm{T}}}{\mathrm{d}t} &= +C_{\mathrm{e,trap}}\left(N_{\mathrm{T}} - n_{\mathrm{T}}\right)n - E_{\mathrm{e,trap}}n_{\mathrm{T}},\\
\frac{\mathrm{d}n_{\mathrm{SRH}}}{\mathrm{d}t} &= +C_{\mathrm{e,SRH}}\left(N_{\mathrm{SRH}} - n_{\mathrm{SRH}}\right)n - E_{\mathrm{e,SRH}}n_{\mathrm{SRH}} - C_{\mathrm{h,SRH}}n_{\mathrm{SRH}}p + E_{\mathrm{h,SRH}}n_{\mathrm{SRH}},\\
\frac{\mathrm{d}p}{\mathrm{d}t} &= +E_{\mathrm{h,SRH}}\left(N_{\mathrm{SRH}} - n_{\mathrm{SRH}}\right) - C_{\mathrm{h,SRH}}n_{\mathrm{SRH}}p.
\end{aligned}
\tag{5.5}
$$

The quick saturation and following constant tendencies of the recombination process are present in the second simulation, presented in subfigure (b) of Figure 5.11. The $n(t=0) \leq 1$ excitation values reproduce the low-temperature tendencies of the recombination process, while the $n(t=0) = 2$ excitation is similar to the decay curves measured at $T = 200$ K with an additional region. This additional region in the recombination dynamics is caused by the same effect as for the simpler simulations. The first region is the simultaneous recombination through the SRH centers and the trapping of charge carriers, followed by a region where the trap states are filled, while there are still free charge carriers in both the valence and conduction bands. In this second region, the recombination of charge carriers through the SRH centers is present as well as the detrapping of charge carriers from shallow traps. After the free charge carriers in the conduction band are all trapped or recombined, the process comprises the detrapping and subsequent recombination of charge carriers through the SRH centers. In the first region, the trapping of charge carriers and the SRH process are both dominant, in the second process the SRH process is dominant while in the third region, the recombination process is limited by the detrapping of charge carriers.

The time-dependent change of free and trapped electrons and holes are shown in Figure 5.12. The simulation shows the trapping of one kind of charge carrier in the shallow traps and the subsequent slow recombination process through the deep level traps limited by the emission of charge carriers from the shallow traps. The simulation is made with the $n(t=0) = 0.1$ condition.

The presented simulations shed light on the recombination process observed in the material at cryogenic conditions. After excitation, one kind of charge carrier gets trapped in shallow traps while the other remains free. The recombination process is limited by the detrapping of charge carriers. As the temperature changes, the capture and emission rates of the shallow trap

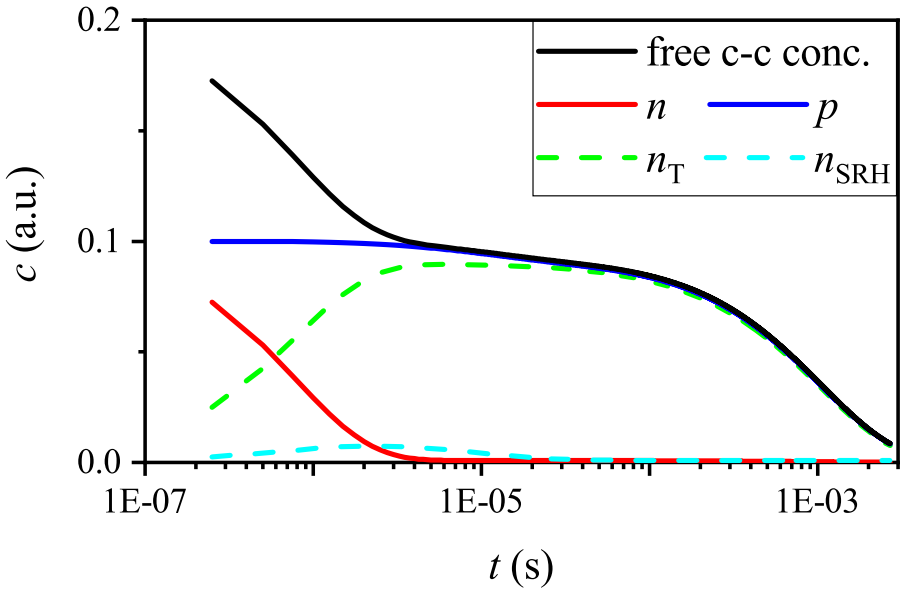

Figure 5.12: Charge carrier concentration values for electrons and holes in individual charge states obtained during the simulation.

change, leading to a change in the charge-carrier recombination dynamics. The inclusion of temperature dependence into the charge carrier recombination simulation is beyond the scope of the current stage of my research, my only goal was to understand the mechanism behind the recombination processes at low-temperature values and form a theory based on this about the power and temperature dependence in recombination dynamics.

5.7 Conclusions

In this chapter, I presented a microwave photoconductivity decay measurement setup capable of measurements in the $10-300$ K range for the inorganic $CsPbBr_3$ perovskite. The measurement system is built to measure the huge dynamic range needed for the measurement of quick and slow recombination processes in the same material. To achieve this, the system is equipped with a low-noise amplifier, a balanced microwave bridge, and an interferometer-based cancellation of the DC reflection coming from the sample in the dark. The system is capable of detection with an IQ mixer and a crystal detector and the measurement could either be done with a high speed oscilloscope or a lock-in amplifier. The optical excitation can be changed easily between multiple wavelengths and the option of a CW excitation is also realized. I demonstrated the outstanding properties of the system and conducted the measurement of $CsPbBr_3$ samples with the help of it.

I investigated the temperature-dependent recombination dynamics of $CsPbBr_3$ single crystals with microwave photoconductivity decay and steady-state photoconductivity measurements. I observed ultralong charge-carrier recombination times at cryogenic conditions. I ruled out the effect of heating and compared the results with transient photoluminescence measurements. I supported the ultralong recombination time with measurements of steady-state photoconductivity in the same temperature regime. I investigated the change in recombination

time during the recombination process and found evidence of charge carrier trapping at low temperatures. I analyzed the temperature-dependent and power-dependent tendencies of the recombination time as a function of reflected microwave voltage with the help of a simulation. Based on the experimental and simulated results, I observed the trapping of charge carriers in shallow traps. The ultralong charge-carrier recombination time is caused by the detrapping of charge carriers limiting the recombination processes.

Chapter 6

Persistent Photoconductivity in Wide Bandgap Semiconductors

In this chapter, I present the observation of persistent photoconductivity in the amorphous Indium Gallium Zinc Oxide and α-Ga_2O_3. The materials under investigation are all thin films. The measurements were conducted with the help of the PDL-1000 instrument equipped with an ultraviolet LED for optical excitation. The measurement methods presented herein allow for the comparison of electrical properties in the materials showing strong persistent photoconductivity. These materials are hard to reliably compare and measure due to the strong and long-lasting photo-response they exhibit. I present a method based on the photoexcitation of thin films and subsequent observation of the relaxation of material properties that allows for the simultaneous evaluation of relaxation dynamics and the comparison of samples with highly excitation-dependent charge carrier mobility, density, and conductivity.

I present the long-term stability and reproducibility of the measurement process of Indium Gallium Zinc Oxide samples exhibiting the persistent photoconductivity effect. I demonstrate the measurement of mobility values as a function of charge carrier density extracted from the measurement sequence. I present the capabilities of the measurement by investigating a sample series with varying manufacturing parameters reproducing the expected tendencies of mobility and carrier density based on the literature. I observed the effect of persistent photoconductivity in a α-Ga_2O_3 thin film sample and conducted the same sequence of illumination and relaxation in the dark.

The presented measurement of Indium Gallium Zink Oxide thin films and the observation of persistent photoconductivity enabled by the PDL-1000 are published in Materials Today: proceedings. [O4]

The presented measurements on the observation of persistent photoconductivity in α-Ga_2O_3 thin films and the measurement of charge carrier mobility as a function of carrier density were demonstrated in the form of a poster at the E-MRS 2023 Fall meeting.

6.1 Observation of persistent photoconductivity

The measurement of materials exhibiting the persistent photoconductivity effect could be problematic due to the long-lasting change caused by photoexcitation. The persistent photoconductivity is a known effect in metal-oxide semiconductors caused by the presence of oxygen

vacancy sites that may trap positive charge carriers thus limiting the recombination of charge carriers. If the contacting of the sample for the measurements is not done in the dark and the material is photoexcited, the persistent photoconductivity may cause long-lasting changes in material properties. This leads to the problematic comparison of samples. One solution to this would be to wait for the relaxation of sample properties in the dark, however, this is not a realistic solution in the case of some samples, since the relaxation process can take days, in some cases the change was small but still present after a week in the dark. The solution I found to this problem is the controlled uniform excitation of multiple samples and the comparison of sample properties at the same generation rate in the steady state. To this end, I added an appropriate optical illumination to the PDL-1000 Hall measurement system and conducted the measurement of controlled excitation and relaxation processes.

With this method, the sample properties can be compared and the characteristic time of relaxation can be observed as well. Another positive aspect of the measurement process is the possible parallel observation of the charge carrier density-dependent mobility. During the excitation process, both parameters are recorded, and the change in charge carrier mobility as a function of carrier density during the excitation and relaxation process can be analyzed. It should be noted, that the mobility and charge carrier density values obtained during illumination are the averaged values from the time window of the measurement. This means that the measurement time of the Hall measurement will be the limiting factor for the resolution of time-dependent effects.

6.2 Amorphous Indium Gallium Zinc Oxide

When I first started the measurement of a sample series consisting of multiple amorphous Indium Gallium Zinc Oxide (a-IGZO) samples created with differing thickness, oxygen concentration and passivation properties the reproducibility of the measurement was not according to my expectations. The reason behind this was the persistent photoconductivity[114–116] of the samples that caused the results to be vastly different depending on the amount of time it took for the contacting and placement of the sample inside the instrument. This leads to the measurement protocol which consists of a measurement sequence of constant illumination followed by relaxation in the dark. The emerging steady-state properties after prolonged illumination and their relaxation dynamics in the dark can be compared.

Subfigure (a) of Figure 6.1. shows the dynamics of the sheet resistance during and after illumination with a fitting of single exponents. Based on the change in the observed timeframe it is easily deductable, that a single Hall measurement is not sufficient for the measurement and comparison of such samples. If we take a random point of a curve similar to the one presented in subfigure (a) of Figure 6.1. from two different samples the state in which the results represent will vary significantly. This is of course an illuminated measurement, the difference would not be so extreme, but the results would nonetheless change between measurements. To demonstrate this, subfigure (b-d) in Figure 6.1. shows the reproducibility of measurements on samples from the same sample series. The samples with different symbol colors and shapes are the different batches, the x-axis of the graphs signifies the three samples in each sample batch. The difference in carrier concentration and sheet resistance is on the scale of orders of magnitude. The simple dark measurement is thus not a suitable measurement for the comparison of different manufacturing processes.

As can be seen in subfigure (a) of Figure 6.1., the characteristic time of saturation during excitation is significantly lower than the relaxation time after illumination. This leads to the conclusion that it is easier, faster, and more relevant to compare the saturated values of samples under the same excitation conditions than values recorded after relaxation that could take days to reach in the dark. It also shows that the relaxation time of photoinduced change is a piece of interesting information, it could be of utmost importance for the time-sensitive operation of instruments based on a given material.

When a measurement is conducted under illumination for a prolonged time it is important to monitor whether any damage is done to the thin film. One reason for this is that the reproducibility of the measurement is an important factor, another reason is that if a measurement runs for multiple days the degradation of a sample may be mistaken to be part of an observed relaxation process. To this end, I investigated the reproducibility and power dependence of the signal. Since I did not want to destroy the sample series before the comparison could be accomplished due to any unforeseen degradation effects, these repeatability and power dependence measurements were conducted on an unrelated IGZO sample that was not part of the sample series.

The power-dependent carrier density, sheet resistance, and mobility values are shown in Figure 6.2. as a function of time. I illuminated the same sample with different intensities and observed the saturation of the carrier density, sheet resistance, and mobility. According to the presented results the saturation occurs between 40% and 60% of the maximal excitation value.

The repeatability of measurements consisting of excitation-relaxation cycles is presented in Figure 6.3. on the same sample as the measurement shown in Figure 6.2. The three measurements were conducted with the same intensity, 95% of the maximal illumination. The high excitation value was chosen so all degradation processes are observed and to ensure the saturation of the sample parameters during the excitation process. In the third run, the sample was illuminated for a shorter time since the saturated levels were already reached. The presented results show that the achieved maximal mobility value is basically unchanged. This implies that there was no significant degradation in the quality of the thin film during the three excitation runs of approximately 1000 minutes of cumulative excitation. The carrier density and sheet resistance graphs show similar relaxation processes for the three subsequent runs in the dark after the excitation is done but the values reached during excitation differ from run to run and there is a small decreasing tendency in these parameters during the excitation process after a maximal excitation is reached. The change is approximately 10% between subsequent runs. Based on this decrease in carrier density and increase in sheet resistance there might be a small change in the sample that does not influence the charge carrier mobility of the thin film sample but causes a small but noticeable change in the resistance and the excitation of charge carriers. Compared to the orders of magnitude the carrier concentration and sheet resistance values change this small difference is not substantial but should be noted.

One can also make a figure using the previously acquired data about the charge carrier density-dependent mobility. Since during the Hall measurement we obtain both information, it is an easy and quick additional thing to do. The charge carrier mobility as a function of charge carrier density is shown in Figure 6.4. The data is extracted from the results presented in Figure 6.3. The tendencies observable in this measurement are according to reports found in the literature[190], the mobility increases as a function of carrier density. The reason behind this is that the carrier transport in amorphous IGZO thin films follows the percolation conduction

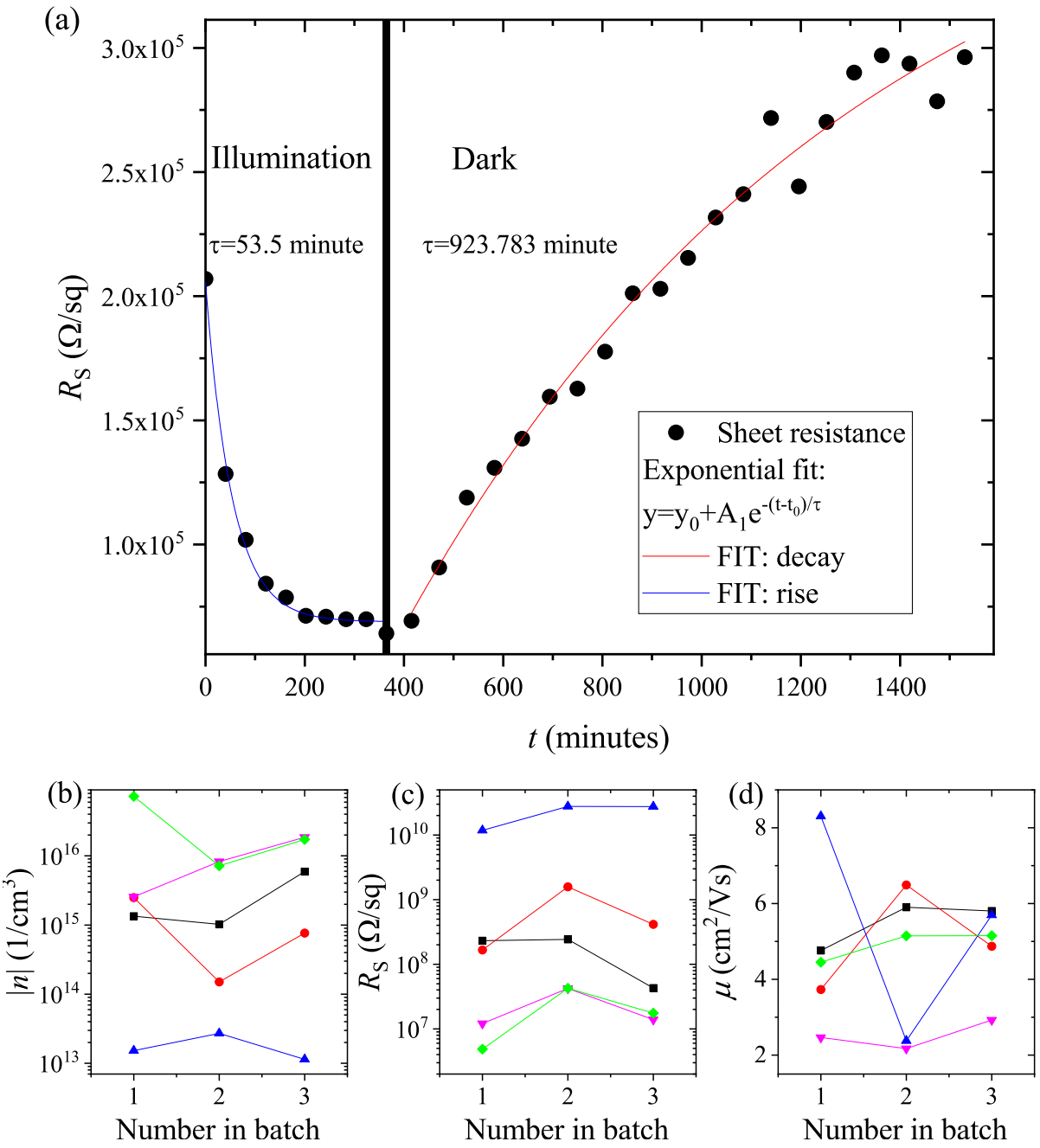

Figure 6.1: Dynamics of sheet resistance during and after illumination is presented in subfigure (a). The time domain before the black vertical division presents illuminated measurements, this region is followed by the relaxation of sample properties in the dark. The fitted curves are single exponents. Subfigures (b, c, d) show the variation in measured parameters caused by the different excitation of the samples between taking them out of the containment and placing them in the measurement unit.

mechanism over the distribution of potential barriers around the conduction band edge by the random nature of the amorphous material[190–193].

To test the accuracy of an excited measurement until a saturated value is reached followed by

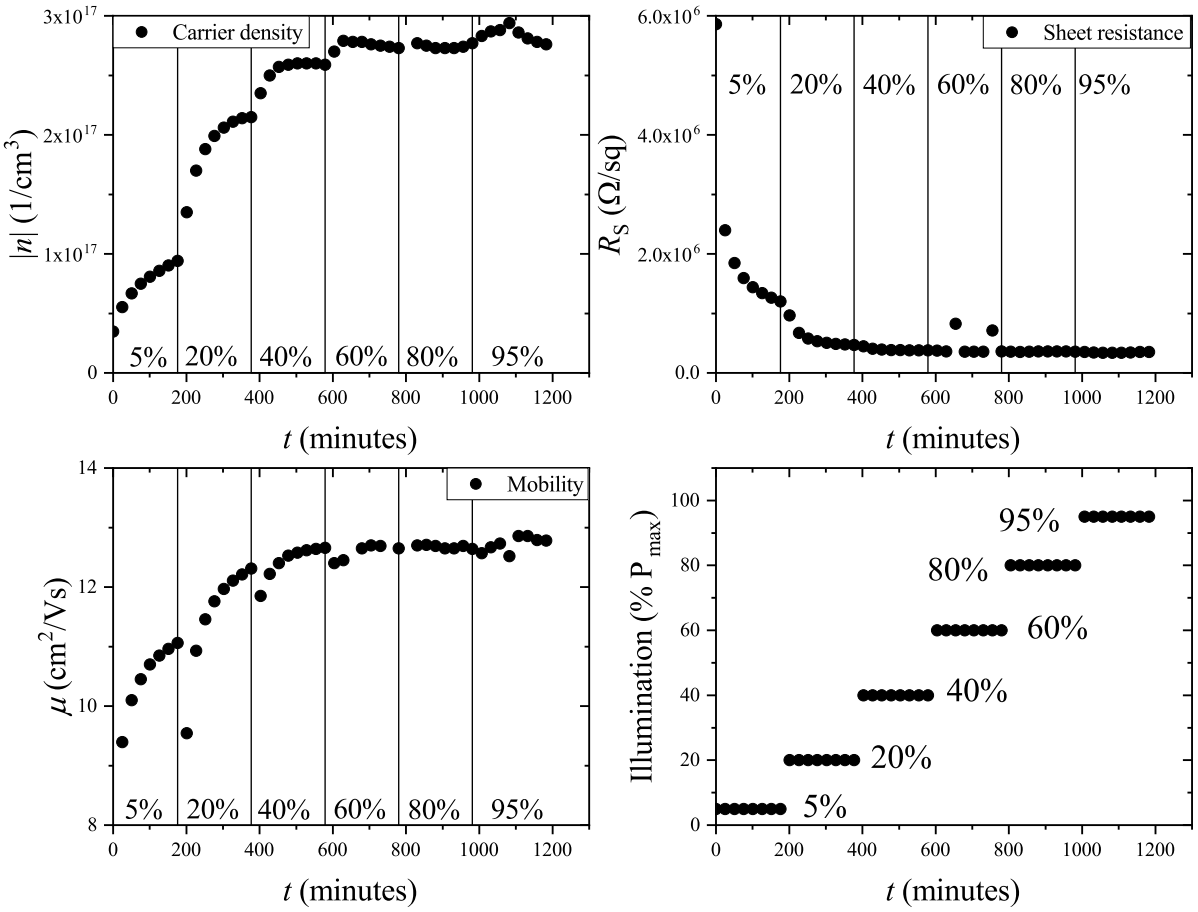

Figure 6.2: Illumination-dependent charge carrier concentration, sheet resistance, and mobility recorded on the same sample simultaneously. The vertical divisions in the figure separated the illumination levels.

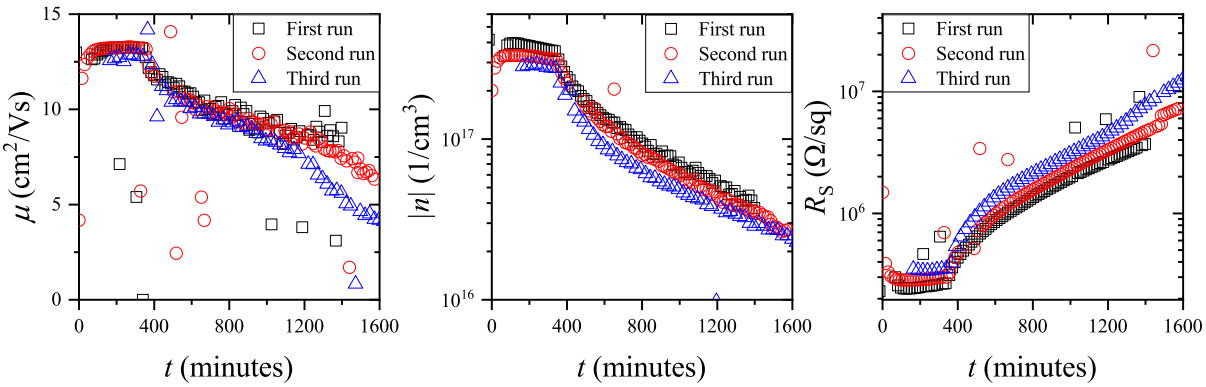

Figure 6.3: Reproducibility of the measurement observed for several runs. The charge carrier mobility is shown on the left, carrier concentration in the middle, and sheet resistance on the right. All presented measurements were recorded as a function of time with the same illumination before the relaxation process.

a relaxation in the dark, a sample series was measured which contained samples with differing

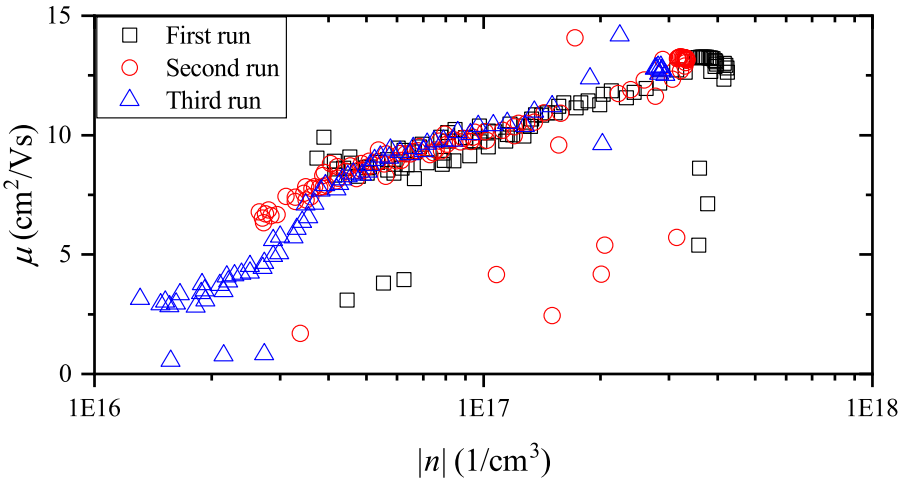

Figure 6.4: The mobility of charge carriers recorded in the three runs presented as a function of charge carrier density.

sample preparation parameters resulting in three observable tendencies. The summary of these samples is given in Table 6.1. This sample series makes it possible to measure the effect of thin film thickness, oxygen concentration during the preparation process, and the presence of a passivation layer on the charge carrier density, mobility, and conductivity of the samples.

Sample ID	a	b	c	d	e
thickness	40.5 nm	82.4 nm	41.3 nm	42.5 nm	41.6 nm
Oxygen ratio	10%	10%	10%	5%	15%
Insulator layer	Yes	Yes	No	Yes	Yes

Table 6.1: Sample parameters for the six compared thin films

The change in mobility and charge carrier concentration is presented in Figure 6.5, and the change in conductivity is presented in Figure 6.6. The summarized results from the evaluation process are presented in Table 6.2. The mobility, carrier density, and sheet resistance values are the saturated values, and the saturation and relaxation time are obtained by fitting a single exponent on the saturation and relaxation of the sample conductivity. It should be noted that the charge carrier concentration is presented as an absolute value since the evaluation process gives the concentration for *n*-type materials as a negative value.

The charge carrier density changes by orders of magnitude in the observed timeframe while the change in mobility is around a factor of two. It should be noted, that the carrier density and conductivity values are not saturated during excitation for samples "b" and "d". This poses no problem in this current comparison since the tendencies of sample manufacturing are well represented with the non-saturated value of these two samples as well. Nonetheless, care should be taken to reach saturation during measurements for the proper comparison of samples. This small error is present because during the measurements only the mobility values were monitored to check the saturation of the measurement, but the conductivity should be the value that saturates.

The presented results show that for samples "b", "c", and "d" the measurement results have relatively low noise, while for samples "a" and "e" the noise is more substantial. This is most

probably caused by the not-perfect contacting of the sample which may lead to a decrease in the signal-to-noise ratio during the measurement of the Hall voltage. This is less prominent on the graph presenting the charge carrier concentration than on the graph presenting the charge carrier mobility due to the logarithmic scale of the former. The feature in the time-dependent signal of sample "c" could be a temperature-dependent effect. Another reason for an increase in the noise of the results is the increasing resistivity. In the case of all samples, the measurement of the mobility and carrier density becomes harder as the time spent in the dark increases. The inaccuracy caused by the increase in resistance could be compensated at high resistances by increasing the measurement time, but the measurement conditions were set for the values during illumination.

Sample	$\mu\ \left(\frac{\text{cm}^2}{\text{Vs}}\right)$	$R_S\ (\Omega/\square)$	Carrier density $\left(\frac{1}{\text{cm}^3}\right)$	$\tau_{\text{sat.}}$ (minute)	$\tau_{\text{relax.}}$ (minute)
a - reference	5.2	$1.7 \cdot 10^7$	$1.9 \cdot 10^{16}$	152	178.1
b - 2x thickness	4.7	$9.8 \cdot 10^5$	$1.6 \cdot 10^{17}$	428.3	2008.5
c - no SiOx layer	8.9	$3.5 \cdot 10^5$	$5.1 \cdot 10^{17}$	47.3	218.7
d - 0.5x O%	7.2	$2.8 \cdot 10^6$	$7.3 \cdot 10^{16}$	113.9	378.2
e - 1.5x O%	3.4	$2.5 \cdot 10^7$	$1.8 \cdot 10^{16}$	305.5	90.2

Table 6.2: The saturated values of mobility, sheet resistance, carrier density, and the characteristic time of saturation and relaxation.

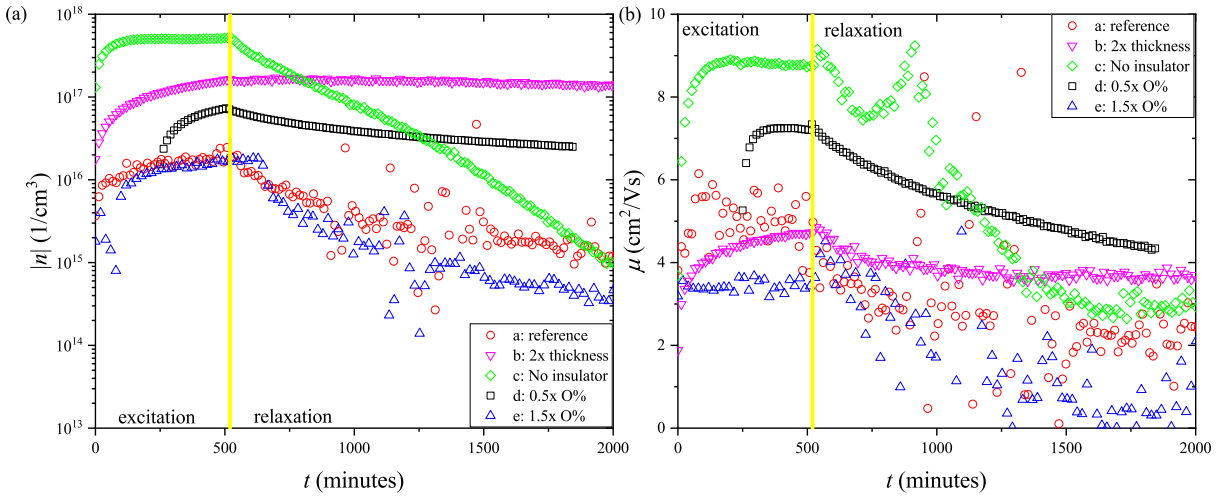

Figure 6.5: Charge carrier density (a) and mobility (b) values as a function of time after excitation for five different sample variations. The vertical yellow line presents the division between illuminated and dark conditions.

The effect of oxygen concentration during sample preparation can be observed through three samples with 5, 10, and 15% oxygen concentration beside argon during film growth. According to the results presented in Figures 6.5. and 6.6., lowering the oxygen content during fabrication leads to higher charge carrier mobility, carrier density, and conductivity. By changing the oxygen content from 15 to 5%, the mobility more than doubled and the difference in sheet resistance was over tenfold. Additionally, the characteristic time of change caused by persistent photoconductivity during excitation was lower, and the relaxation was longer when less

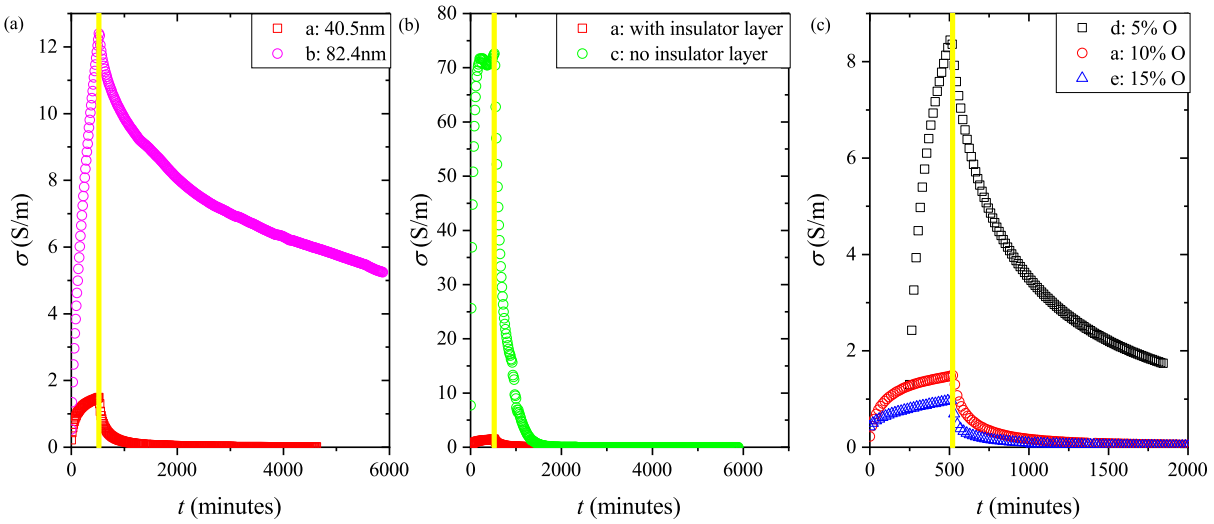

Figure 6.6: Comparison of the change in conductivity for three different parameters: sample thickness (a), presence of an insulator layer (b), and oxygen content during sample preparation (c). All presented graphs include the rise during excitation and relaxation in the dark of conductivity.

oxygen was used during sample creation. The observed change in mobility, carrier density, and conductivity fall in line with the reported tendencies in the literature regarding the oxygen content during fabrication [123]. The reason behind this effect is the increased oxygen content in the thin film if the oxygen concentration is increased during the sample preparation, which translates to a lower concentration of oxygen vacancy sites [125, 194].

The sample series contained a sample with a thickness of 40.5 nm and another with the same oxygen content during fabrication that is 82.4 nm thick. According to the measurements conducted on the samples, the charge carrier concentration in the saturated state is about an order of magnitude higher, and the sheet resistance is about an order of magnitude lower in the case of the thicker thin film sample. In the meantime, the measured mobility is only slightly smaller for the thicker sample. These results indicate that the quality of the thin film is approximately the same since the mobility of the charge carriers would be vastly different if the film quality was different. This is due to the scattering effect of boundaries in polycrystalline materials leading to the lowering of the measured charge carrier mobility. The results also indicate an increase of oxygen vacancy concentration as a result of the increased sample thickness. The thickness of the thin film influences the electrical properties of the sample differently depending on the sample preparation procedure[192, 195, 196]. The thickness dependence presented here falls in line with results found in the literature for some effects. The presented results fall in line with the bulk oxygen vacancy concentration decreasing with the decreasing thickness of the thin film[125]. The sample with increased thickness shows the longest saturation and relaxation time. This could mean that the oxygen vacancies further away from the sample surface release the captured charge carriers in a significantly larger timescale than the vacancy centers near the sample surface.

The sample without an insulation layer shows the highest conductivity, mobility, and charge carrier density in the sample series. The saturation time is also the quickest of all the samples, with the relaxation time showing a small increase from the reference sample with a SiOx layer.

The inclusion of a SiOx layer can cause a change in the sample in multiple manners. The interface between the thin film and the insulation layer may cause changes in the electrical properties. The process of depositing an insulator layer may damage the sample surface. The temperature, duration, and number of steps of the annealing process needed after the sputtering of the atoms of the passivation layer on the thin film also influence the quality of the thin film [197, 198]. Based on the obtained results and according to the mentioned possible explanations I believe that the inclusion of the passivation layer caused a degradation of the thin layers resulting in smaller mobility and conductivity values.

6.3 α-Ga_2O_3

I investigated the persistent photoconductivity effect in α-Ga_2O_3 samples. This is a variation of Gallium Oxide that has a corundum structure. The α variant is metastable and has the highest bandgap of all the Gallium Oxide variants. The persistent photoconductivity is caused by the oxygen vacancies in the material. Similarly to the previously investigated IGZO samples, the oxygen vacancies in the material can trap charge carriers, leading to a prolonged change in electrical properties.

The measurement was realized with the help of the PDL-1000 system. I used an ultraviolet wide spectrum LED with a central wavelength of $\lambda = 266$ nm for the excitation of the sample. I conducted measurements of the saturation and relaxation time of sheet resistance and of the excitation-dependent charge carrier density and mobility.

Figure 6.7. shows the change in the sheet resistance of the sample as a function of excitation. Subfigure (a) presents the change in sheet resistance as the excitation power is increased and decreased through multiple runs. The x-axis shows the current applied to the LED, since the exact excitation reaching the sample is not calibrated. There is a significant difference between the curves recorded while increasing and decreasing the excitation. At the end of the illuminated measurement in the dark, the sheet resistance is approximately 20% lower, than at the beginning of the measurement sequence. Subfigure (b) presents the saturation and relaxation of sheet resistance under continuous wave excitation. The saturation time is an order of magnitude lower, only $\tau_{\text{sat.}} = 5.5$ minutes, the relaxation time is $\tau_{\text{relax.}} = 65.79$ minutes. It is important to note, that the relaxation is only partial by the 2 hours mark observed in the Figure. The difference between the dark value and the value reached by the 2 hour mark is approximately 10%. This shows, that there is still a longer relaxation happening even after this initial relaxation process.

The mobility of charge carriers is presented as a function of charge carrier density in Figure 6.8. The measurement was conducted by increasing and then decreasing the optical illumination. My observations show that the mobility decreases for higher excitation levels which result in higher charge carrier density values. The decreasing mobility of charge carriers as the carrier density increases is according to results found in the literature for β Gallium Oxide[111]. However, in the case of α-Ga_2O_3 both the decreasing and increasing of charge carrier mobility with increasing doping density are reported in the literature[199]. The decrease of mobility as a function of carrier density may be due to the scattering of charge carriers on ionized impurities.[200] Since the optical excitation of the material may generate ionized impurities this might be the reason behind this observed effect. However, the transport properties of α Gallium Oxide are still under investigation and need further study to fully understand.

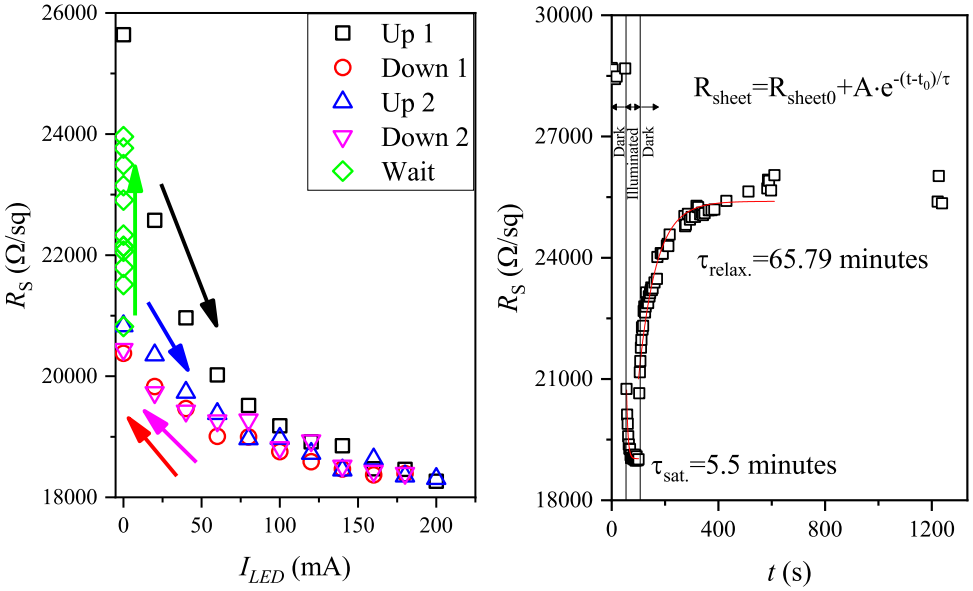

Figure 6.7: Effect of persistent photoconductivity on the Ga_2O_3 sample during and after optical excitation with the help of an ultraviolet LED. The excitation-dependent change is presented in subfigure (a). The subfigure shows the sheet resistance as the illumination is increased and decreased. The time dependence of sheet resistance is presented in (b) during illumination and after excitation in the dark.

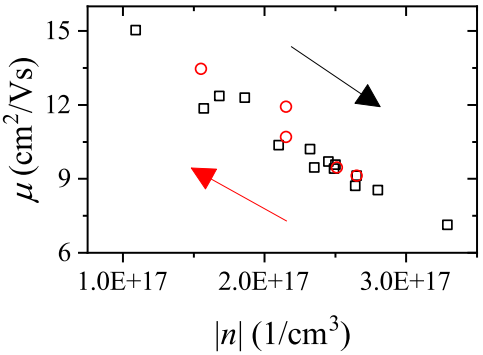

Figure 6.8: Mobility of charge carriers as a function of charge carrier density. The measurement was conducted by increasing and decreasing the optical excitation.

6.4 Conclusions

I created a measurement protocol that can reliably measure and compare samples that exhibit the persistent photoconductivity effect. The measurement protocol consists of the photoexcitation of the sample followed by relaxation in the dark. The saturated values during excitation and the saturation and relaxation time can be compared for a sample series when the measurement conditions are not changed.

I demonstrated the potential of the measurement with the help of reproducibility measurements as well as with the presentation of the mobility of charge carriers as a function of charge carrier density obtained from an excitation-relaxation cycle. I further demonstrated the measurement protocol by measuring a sample sequence consisting of Indium Gallium Zinc Oxide

samples with varying thickness, oxygen concentration during manufacturing, and the presence of a passivation layer. With the help of the sample series, I showed that the results obtained through the presented method are reliable and that the observed tendencies fall in line with the information found in the literature regarding the investigated manufacturing changes.

I investigated the persistent photoconductivity effect in an α Gallium Oxide sample. I presented the effect of saturation and relaxation in a similar manner as for the amorphous Indium Gallium Zinc Oxide samples and obtained the mobility of charge carriers as a function of charge carrier density. The $\mu(\Delta n)$ values fall in line with the expectations based on the information found in the literature.

Chapter 7

Summary and Thesis Points

This thesis focuses on the photoinduced change in the electrical properties of novel semiconductors. I present the importance of research focused on perovskites and wide bandgap semiconductors in Chapter 1. The study of these materials is of outmost importance for the scientific community and industry alike. Deeper knowledge and understanding of the processes and properties governing the charge carrier dynamics of these materials is the key for their widespread application. The development of devices based on novel semiconductors cannot be realized without research of the materials. My research is focused on the investigation of photoexcited charge carriers in novel semiconductors and their temperature dependent recombination dynamics.

I present the theoretical background of the investigated materials and the methods used during the measurement in Chapter 2. First the properties of semiconductors is presented with detail given to perovskites and wide bandgap materials. Next the charge-carrier generation and recombination dynamics are detailed in semiconductors. This is followed by the explanation of the detection of photoexcited charge carriers and the detailed explanation of the microwave photoconductivity measurement method. The Chapter ends with the presentation of transport properties of charge carriers in semiconductors.

I present the measurement methods and sample preparation in Chapter 3. I introduce the cavity-based and coplanar waveguide-based microwave photoconductivity decay measurement systems. I present the properties of the PDL-1000 Hall effect measurement system used for the Hall effect and sheet resistance measurements.

Chapters 4 through 6 are a detailed presentation of the results and a discussion of their explanation. These are summarized in the following Thesis Points:

1. I developed a cavity-based microwave photoconductivity decay measurement setup capable of measurements in the $4-300$ K temperature range. With the assembled instrument, I investigated the temperature-dependent recombination dynamics of photoexcited charge carriers in methylammonium lead halide perovskites. I carried out the temperature-dependent measurements in a range where structural phase transitions were previously reported in the materials. I conducted multiple measurements during which I found substantial changes in charge-carrier recombination dynamics and photo response at the orthorhombic to tetragonal phase transition while the tetragonal to cubic phase transition shows no such change. The changes could be identified due to the structural transformation. I presented ultralong charge-carrier recombination times in the orthorhombic

phase for all three perovskites with the longest being over 68 μs in the $MAPbBr_3$ single crystal.[O1]

2. I observed the effect of charge-carrier scattering on grain boundaries in $CH_3NH_3PbBr_3$ perovskite crystals with varying morphology and quenching state. To do this, I observed the difference in temperature-dependent charge-carrier dynamics of a slowly cooled and quickly cooled sample allowed by the realized measurement system, thus creating quenched and normal phases in the same sample. To further investigate this effect I compared the temperature-dependent charge carrier dynamics of three $CH_3NH_3PbBr_3$ crystals created with different sample preparation methods leading to differences in the sample morphology. The observations demonstrate that grain boundaries caused by either morphology or quenching lead to a decrease in charge-carrier lifetime due to the increase in carrier scattering events and the possible increase in recombination centers.[O1]

3. I developed a temperature-dependent microwave photoconductivity decay measurement system based on a coplanar waveguide capable of fast detection with high sensitivity. The measurement system is developed to be able to measure the fast and slow recombination processes during a single measurement covering a time domain range of 3 orders of magnitude. I investigated the temperature-dependent recombination dynamics of photoexcited charge carriers in cesium lead bromide single crystals with the developed measurement system. I carried out photoconductivity decay measurements in a wide temperature range and observed recombination times over 1 ms at cryogenic conditions. [O2] [O3]

4. I investigated the power dependence of the charge-carrier recombination dynamics and made simulations of charge-carrier recombination processes to prove the effect of charge-carrier trapping and the microwave reflection of the measurement system to rule out heating effects. I presented results that suggest that the long charge-carrier recombination time is caused by the trapping of one kind of charge carrier in shallow traps leading to ultralong recombination times. A simulation was developed to recreate the measured charge carrier recombination dynamics in a system with a shallow and deep-level trap in the bandgap. [O2]

5. I developed a measurement sequence for the characterization and comparison of thin films that possess the persistent photoconductance phenomena. With the measurement sequence, I compared the change of charge carrier density, mobility, and sheet resistance during and after excitation with the help of a sample series consisting of five samples. The samples provided a pool of manufacturing changes that allowed for the observation of effects related to sample thickness, oxygen concentration during fabrication, and the passivation of the sample surface. With the help of this measurement, I reliably reproduced the tendencies reported in the literature and showed a method that can compare samples with properties that vary substantially between measurements without the proper precautions. I conducted these measurements with the help of the PDL-1000 system made by Semilab. During my PhD studies, I contributed to the development of the hardware and software of the PDL-1000 system. [O4]

List of Publications

[O1] A. Bojtor, S. Kollarics, B. G. Márkus, A. Sienkiewicz, M. Kollár, L. Forró, and F. Simon, "Ultralong Charge Carrier Recombination Time in Methylammonium Lead Halide Perovskites," *ACS Photonics*, vol. 9, no. 10, pp. 3341–3350, 2022.

[O2] A. Bojtor, D. Krisztián, F. Korsós, S. Kollarics, G. Paráda, T. Pinel, M. Kollár, E. Horváth, X. Mettan, H. Shiozawa, B. G. Márkus, L. Forró, and F. Simon, "Millisecond-Scale Charge-Carrier Recombination Dynamics in the $CsPbBr_3$ Perovskite," *Advanced Energy and Sustainability Research*, p. 2400043, 2024.

[O3] A. Bojtor *et al.*, "Time-resolved Photoconductivity Decay Measurements with Broadband Radiofrequency Detection and Excitation Energy," *In preparation*, 2024.

[O4] A. Bojtor, G. Paráda, P. Tüttő, H. Korka, K. Szőke, and F. Korsós, "Investigation of Persistent Photoconductance and Related Electron Mobility in Thin IGZO Layers With the PDL Hall Technique," *Materials Today: Proceedings*, vol. 93, pp. 9–15, 2023, international Conferences & Exhibition on Nanotechnologies, Organic Electronics & Nanomedicine – Nanotexnology (NANOTEX 2022).

Other publications not included as thesis points

1. S. Kollarics, A. Bojtor, K. Koltai, B. G. Márkus, K. Holczer, J. Volk, G. Klujber, M. Szieberth, and F. Simon *Optical–Microwave Pump–Probe Studies of Electronic Properties in Novel Materials* Phys. Status Solidi B, vol. 257, no. 12, p. 2000298, 2020.

2. S. Kollarics, F. Simon, A. Bojtor, K. Koltai, G. Klujber, M. Szieberth, B. Márkus, D. Beke, K. Kamarás, A. Gali, D. Amirari, R. Berry, S. Boucher, D. Gavryushkin, G. Jeschke, J. Cleveland, S. Takahashi, P. Szirmai, L. Forró, E. Emmanouilidou, R. Singh, and K. Holczer *Ultrahigh nitrogen-vacancy center concentration in diamond* Carbon, vol. 188, pp. 393–400, 2022

3. G. Paráda, F. Korsós, A. Bojtor, J.-W. G. Bos, E. Don, J. W. Bowers, M. Togay *Exploiting bi-modulated magnetic field and drive current modulation to achieve high-sensitivity Hall measurements on thermoelectric samples* MRS Advances 7, 608–613 (2022)

4. B. Gyüre-Garami, B. Blum, O. Sági, A. Bojtor, S. Kollarics, G. Csősz, B. G. Márkus, J. Volk, F. Simon *Ultrafast sensing of photoconductivity decay using microwave resonators* J. Appl. Phys. 126, 235702 (2019)

5. J. Palotás, M. Negyedi, S. Kollarics, A. Bojtor, P. Rohringer, T. Pichler, F. Simon *Incidence of Quantum Confinement on Dark Triplet Excitons in Carbon Nanotubes* ACS Nano 14 (9), 11254-11261 (2020)

6. S. Kollarics, J. Palotás, A. Bojtor, B. G. Márkus, P. Rohringer, T. Pichler, F. Simon *Improved Laser Based Photoluminescence on Single-Walled Carbon Nanotubes* Phys. Status Solidi B 256, 1900235 (2019)

List of Abbreviations

μPCD - microwave photoconductivity decay
a-IGZO - amorphous indium gallium zinc oxid
CBCPW - Conductor-backed coplanar waveguide
CPW - Coplanar waveguide
CW - Continuous Wave
DMSO - Dymethyl sulfoxid
IGZO - Indium gallium zinc oxid
IRF - Instrumental resolution function
LED - Light emitting diode
LNA - Low-noise amplifier
LO - Local oscillator
PDL - Parallel Dipole Line
PPC - Persistent photoconductivity
RF - Radio frequency
SRH - Shockley-Read-Hall
TRMCD - transient microwave photoconductivity decay
TRPL - transient photoluminescence
A - signal amplitude
ΔG - Change in photoconductivity
μ - charge carrier mobility
n - charge carrier density
Δn - excess charge carrier density
R_S - Sheet resistance
φ - signal phase
τ_c - charge carrier lifetime

Bibliography

[1] J.-P. Correa-Baena, M. Saliba, T. Buonassisi, M. Graetzel, A. Abate, W. Tress, and A. Hagfeldt, "Promises and challenges of perovskite solar cells," *Science*, vol. 358, no. 6364, pp. 739–744, 2017.

[2] J. Huang, Y. Yuan, Y. Shao, and Y. Yan, "Understanding the physical properties of hybrid perovskites for photovoltaic applications," *Nat. Rev. Mater.*, vol. 2, p. 17042, 2017.

[3] K. Lin, J. Xing, L. N. Quan, F. P. G. de Arquer, X. Gong, J. Lu, L. Xie, W. Zhao, D. Zhang, C. Yan, W. Li, X. Liu, Y. Lu, J. Kirman, E. H. Sargent, Q. Xiong, and Z. Wei, "Perovskite light-emitting diodes with external quantum efficiency exceeding 20 per cent," *Nature*, vol. 562, no. 7726, pp. 245+, 2018.

[4] F. Zhang, H. Zhong, C. Chen, X.-g. Wu, X. Hu, H. Huang, J. Han, B. Zou, and Y. Dong, "Brightly Luminescent and Color-Tunable Colloidal $CH_3NH_3PbX_3$ (X = Br, I, Cl) Quantum Dots: Potential Alternatives for Display Technology," *ACS Nano*, vol. 9, no. 4, pp. 4533–4542, 2015.

[5] L. Protesescu, S. Yakunin, M. I. Bodnarchuk, F. Krieg, R. Caputo, C. H. Hendon, R. X. Yang, A. Walsh, and M. V. Kovalenko, "Nanocrystals of Cesium Lead Halide Perovskites ($CsPbX_3$, X = Cl, Br, and I): Novel Optoelectronic Materials Showing Bright Emission with Wide Color Gamut," *Nano Lett.*, vol. 15, no. 6, pp. 3692–3696, 2015.

[6] Y. Fu, H. Zhu, C. C. Stoumpos, Q. Ding, J. Wang, M. G. Kanatzidis, X. Zhu, and S. Jin, "Broad Wavelength Tunable Robust Lasing from Single-Crystal Nanowires of Cesium Lead Halide Perovskites ($CsPbX_3$, X = Cl, Br, I)," *ACS Nano*, vol. 10, no. 8, pp. 7963–7972, 2016.

[7] S. W. Eaton, M. Lai, N. A. Gibson, A. B. Wong, L. Dou, J. Ma, L.-W. Wang, S. R. Leone, and P. Yang, "Lasing in robust cesium lead halide perovskite nanowires," *Proc. Natl. Acad. Sci.*, vol. 113, no. 8, pp. 1993–1998, 2016.

[8] N.-G. Park and K. Zhu, "Scalable fabrication and coating methods for perovskite solar cells and solar modules," *Nat. Rev. Mater.*, vol. 5, pp. 333–350, 2020.

[9] F. Fu, T. Feurer, T. Weiss, S. Pisoni, E. Avancini, C. Andres, S. Buecheler, and A. Tiwari, "High-efficiency inverted semi-transparent planar perovskite solar cells in substrate configuration," *Nat. Energy*, vol. 2, p. 16190, 2016.

[10] Y. Haruta, T. Ikenoue, M. Miyake, and T. Hirato, "One-Step Coating of Full-Coverage $CsPbBr_3$ Thin Films via Mist Deposition for All-Inorganic Perovskite Solar Cells," *ACS Appl. Energy Mater.*, vol. 3, no. 12, pp. 11 523–11 528, 2020.

[11] K. P. Bhandari and R. J. Ellingson, "An Overview of Hybrid Organic–Inorganic Metal Halide Perovskite Solar Cells," in *A Comprehensive Guide to Solar Energy Systems*, T. M. Letcher and V. M. Fthenakis, Eds. Academic Press, 2018, pp. 233 – 254.

[12] A. Singha, A. Paul, S. Koul, V. Sharma, S. Mallick, K. R. Balasubramaniam, and D. Kabra, "Stable and Efficient Large-Area 4T Si/perovskite Tandem Photovoltaics with Sputtered Transparent Contact," *Sol. RRL*, vol. 7, no. 12, p. 2300117, 2023. [Online]. Available: https://onlinelibrary.wiley.com/doi/abs/10.1002/solr.202300117

[13] A. W. Y. Ho-Baillie, H. G. J. Sullivan, T. A. Bannerman, H. P. Talathi, J. Bing, S. Tang, A. Xu, D. Bhattacharyya, I. H. Cairns, and D. R. McKenzie, "Deployment Opportunities for Space Photovoltaics and the Prospects for Perovskite Solar Cells," *Adv. Mater. Technol.*, vol. 7, no. 3, p. 2101059, 2022.

[14] D. Pérez-del Rey, C. Dreessen, A. M. Igual-Muñoz, L. van den Hengel, M. C. Gélvez-Rueda, T. J. Savenije, F. C. Grozema, C. Zimmermann, and H. J. Bolink, "Perovskite Solar Cells: Stable under Space Conditions," *Sol. RRL*, vol. 4, no. 12, p. 2000447, 2020.

[15] K. Mantulnikovs, A. Glushkova, P. Matus, L. Ćirić, M. Kollár, L. Forró, E. Horváth, and A. Sienkiewicz, "Morphology and Photoluminescence of $CH_3NH_3PbI_3$ Deposits on Nonplanar, Strongly Curved Substrates," *ACS Photonics*, vol. 5, no. 4, pp. 1476–1485, 2018.

[16] J. Shamsi, P. Rastogi, V. Caligiuri, A. L. Abdelhady, D. Spirito, L. Manna, and R. Krahne, "Bright-Emitting Perovskite Films by Large-Scale Synthesis and Photoinduced Solid-State Transformation of $CsPbBr_3$ Nanoplatelets," *ACS Nano*, vol. 11, no. 10, pp. 10 206–10 213, 2017.

[17] J. Ding, S. Du, Z. Zuo, Y. Zhao, H. Cui, and X. Zhan, "High Detectivity and Rapid Response in Perovskite $CsPbBr_3$ Single-Crystal Photodetector," *J. Phys. Chem. C*, vol. 121, no. 9, pp. 4917–4923, 2017.

[18] L. Clinckemalie, D. Valli, M. B. J. Roeffaers, J. Hofkens, B. Pradhan, and E. Debroye, "Challenges and Opportunities for $CsPbBr_3$ Perovskites in Low- and High-Energy Radiation Detection," *ACS Energy Lett.*, vol. 6, no. 4, pp. 1290–1314, 2021.

[19] S. Yakunin, D. N. Dirin, Y. Shynkarenko, V. Morad, I. Cherniukh, O. Nazarenko, D. Kreil, T. Nauser, and M. V. Kovalenko, "Detection of gamma photons using solution-grown single crystals of hybrid lead halide perovskites," *Nat. Photon.*, vol. 10, no. 9, pp. 585–589, Sep 2016. [Online]. Available: https://doi.org/10.1038/nphoton.2016.139

[20] P. Andričević, G. Náfrádi, M. Kollár, B. Náfrádi, S. Lilley, C. Kinane, P. Frajtag, A. Sienkiewicz, A. Pautz, E. Horváth, and L. Forró, "Hybrid halide perovskite neutron detectors," *Sci. Rep.*, vol. 11, no. 1, p. 17159, Aug 2021. [Online]. Available: https://doi.org/10.1038/s41598-021-95586-3

[21] K. Nomura, H. Ohta, K. Ueda, T. Kamiya, M. Hirano, and H. Hosono, "Thin-film transistor fabricated in single-crystalline transparent oxide semiconductor," *Science*, vol. 300, no. 5623, pp. 1269–1272, 2003.

[22] K. Nomura, H. Ohta, A. Takagi, T. Kamiya, M. Hirano, and H. Hosono, "Room-temperature fabrication of transparent flexible thin-film transistors using amorphous oxide semiconductors," *Nature*, vol. 432, no. 7016, pp. 488–492, 2004.

[23] N. S. Jamwal and A. Kiani, "Gallium Oxide Nanostructures: A Review of Synthesis, Properties and Applications," *Nanomaterials*, vol. 12, no. 12, 2022. [Online]. Available: https://www.mdpi.com/2079-4991/12/12/2061

[24] H.-H. Hsieh, H.-H. Lu, H.-C. Ting, C.-S. Chuang, C.-Y. Chen, and Y. Lin, "Development of IGZO TFTs and their applications to next-generation flat-panel displays," *J. Inf. Disp.*, vol. 11, no. 4, pp. 160–164, 2010.

[25] J.-h. Lee, D.-h. Kim, D.-j. Yang, S.-y. Hong, K.-s. Yoon, P.-s. Hong, C.-o. Jeong, H.-S. Park, S. Y. Kim, S. K. Lim *et al.*, "42.2: World's largest (15-inch) XGA AMLCD panel using IGZO oxide TFT," in *SID Symposium Digest of Technical Papers*, vol. 39, no. 1. Wiley Online Library, 2008, pp. 625–628.

[26] H.-N. Lee, J. Kyung, S. K. Kang, D. Y. Kim, M.-C. Sung, S.-J. Kim, C. N. Kim, H. G. Kim, and S.-t. Kim, "68.2: 3.5 inch QCIF+ AM-OLED panel based on oxide TFT backplane," in *SID Symposium Digest of Technical Papers*, vol. 38, no. 1. Wiley Online Library, 2007, pp. 1826–1829.

[27] K. Miura, T. Ueda, S. Nakano, N. Saito, Y. Hara, K. Sugi, T. Sakano, H. Yamaguchi, I. Amemiya, K. Akimoto *et al.*, "4.1: Low-Temperature-Processed IGZO TFTs for Flexible AMOLED with Integrated Gate Driver Circuits," in *SID Symposium Digest of Technical Papers*, vol. 42, no. 1. Wiley Online Library, 2011, pp. 21–24.

[28] S. Nakano, N. Saito, K. Miura, T. Sakano, T. Ueda, K. Sugi, H. Yamaguchi, I. Amemiya, M. Hiramatsu, and A. Ishida, "Highly reliable a-IGZO TFTs on a plastic substrate for flexible AMOLED displays," *J. Soc. Inf. Disp.*, vol. 20, no. 9, pp. 493–498, 2012.

[29] J.-S. Park, T.-W. Kim, D. Stryakhilev, J.-S. Lee, S.-G. An, Y.-S. Pyo, D.-B. Lee, Y. G. Mo, D.-U. Jin, and H. K. Chung, "Flexible full color organic light-emitting diode display on polyimide plastic substrate driven by amorphous indium gallium zinc oxide thin-film transistors," *Appl. Phys. Lett.*, vol. 95, no. 1, 2009.

[30] M. Higashiwaki, A. Kuramata, H. Murakami, and Y. Kumagai, "State-of-the-art technologies of gallium oxide power devices," *J. Phys. D: Appl. Phys.*, vol. 50, no. 33, p. 333002, 2017.

[31] Z. Liu, T. Yamazaki, Y. Shen, T. Kikuta, N. Nakatani, and Y. Li, "O_2 and CO sensing of Ga_2O_3 multiple nanowire gas sensors," *Sens. Actuators, B*, vol. 129, no. 2, pp. 666–670, 2008.

[32] J. Zhu, Z. Xu, S. Ha, D. Li, K. Zhang, H. Zhang, and J. Feng, "Gallium oxide for gas sensor applications: A comprehensive review," *Materials*, vol. 15, no. 20, p. 7339, 2022.

[33] X. Chen, F. Ren, S. Gu, and J. Ye, "Review of gallium-oxide-based solar-blind ultraviolet photodetectors," *Photonics Res.*, vol. 7, no. 4, pp. 381–415, 2019.

[34] N. Kumar, J. Kumar, and S. Panda, "Low temperature annealed amorphous indium gallium zinc oxide (a-IGZO) as a pH sensitive layer for applications in field effect based sensors," *AIP Adv.*, vol. 5, no. 6, 2015.

[35] H. Tang, Y. Li, R. Sokolovskij, L. Sacco, H. Zheng, H. Ye, H. Yu, X. Fan, H. Tian, T.-L. Ren *et al.*, "Ultra-high sensitive NO_2 gas sensor based on tunable polarity transport in CVD-WS_2/IGZO pN heterojunction," *ACS Appl. Mater. Interfaces*, vol. 11, no. 43, pp. 40 850–40 859, 2019.

[36] Y.-H. Tai, H.-L. Chiu, and L.-S. Chou, "Active matrix touch sensor detecting time-constant change implemented by dual-gate IGZO TFTs," *Solid-State Electron.*, vol. 72, pp. 67–72, 2012.

[37] D. J. Yang, G. C. Whitfield, N. G. Cho, P.-S. Cho, I.-D. Kim, H. M. Saltsburg, and H. L. Tuller, "Amorphous $InGaZnO_4$ films: Gas sensor response and stability," *Sens. Actuators, B*, vol. 171, pp. 1166–1171, 2012.

[38] H. Jeong, C. S. Kong, S. W. Chang, K. S. Park, S. G. Lee, Y. M. Ha, and J. Jang, "Temperature sensor made of amorphous indium–gallium–zinc oxide TFTs," *IEEE Electron Device Lett.*, vol. 34, no. 12, pp. 1569–1571, 2013.

[39] N. W. Ashcroft and N. D. Mermin, *Solid state physics*. Cengage, 1976. [Online]. Available: https://cir.nii.ac.jp/crid/1130580826900829452

[40] J. Sólyom, *Fundamentals of the physics of solids II: Electronic Properties*. Springer, 2008.

[41] J. S. Manser, J. A. Christians, and P. V. Kamat, "Intriguing Optoelectronic Properties of Metal Halide Perovskites," *Chem. Rev.*, vol. 116, no. 21, pp. 12 956–13 008, 2016.

[42] P. V. Kamat, J. Bisquert, and J. Buriak, "Lead-Free Perovskite Solar Cells," *ACS Energy Lett.*, vol. 2, no. 4, pp. 904–905, 2017. [Online]. Available: https://doi.org/10.1021/acsenergylett.7b00246

[43] A. Dey, J. Ye, A. De, E. Debroye, S. K. Ha, E. Bladt, A. S. Kshirsagar, Z. Wang, J. Yin, Y. Wang, L. N. Quan, F. Yan, M. Gao, X. Li, J. Shamsi, T. Debnath, M. Cao, M. A. Scheel, S. Kumar, J. A. Steele, M. Gerhard, L. Chouhan, K. Xu, X.-g. Wu, Y. Li, Y. Zhang, A. Dutta, C. Han, I. Vincon, A. L. Rogach, A. Nag, A. Samanta, B. A. Korgel, C.-J. Shih, D. R. Gamelin, D. H. Son, H. Zeng, H. Zhong, H. Sun, H. V. Demir, I. G. Scheblykin, I. Mora-Seró, J. K. Stolarczyk, J. Z. Zhang, J. Feldmann, J. Hofkens, J. M. Luther, J. Pérez-Prieto, L. Li, L. Manna, M. I. Bodnarchuk, M. V. Kovalenko, M. B. J. Roeffaers, N. Pradhan, O. F. Mohammed, O. M. Bakr, P. Yang, P. Müller-Buschbaum, P. V. Kamat, Q. Bao, Q. Zhang, R. Krahne, R. E. Galian, S. D. Stranks, S. Bals, V. Biju, W. A. Tisdale, Y. Yan, R. L. Z. Hoye, and L. Polavarapu, "State of the Art and Prospects for Halide Perovskite Nanocrystals," *ACS Nano*, vol. 15, no. 7, pp. 10 775–10 981, 2021.

[44] K. S. Schanze, P. V. Kamat, P. Yang, and J. Bisquert, "Progress in Perovskite Photocatalysis," *ACS Energy Lett.*, vol. 5, no. 8, pp. 2602–2604, 2020. [Online]. Available: https://doi.org/10.1021/acsenergylett.0c01480

[45] J. Tian, Q. Xue, Q. Yao, N. Li, C. J. Brabec, and H.-L. Yip, "Inorganic Halide Perovskite Solar Cells: Progress and Challenges," *Adv. Energy Mater.*, vol. 10, no. 23, 2020.

[46] S. A. Bretschneider, J. Weickert, J. A. Dorman, and L. Schmidt-Mende, "Research update: Physical and electrical characteristics of lead halide perovskites for solar cell applications," *APL Mater.*, vol. 2, no. 4, p. 040701, 2014.

[47] Y. Deng, Q. Wang, Y. Yuan, and J. Huang, "Vividly colorful hybrid perovskite solar cells by doctor-blade coating with perovskite photonic nanostructures," *Mater. Horiz.*, vol. 2, pp. 578–583, 2015.

[48] B. Náfrádi, G. Náfrádi, L. Forró, and E. Horváth, "Methylammonium lead iodide for efficient x-ray energy conversion," *J. Phys. Chem. C*, vol. 119, no. 45, pp. 25 204–25 208, 2015.

[49] Z.-K. Tan, R. S. Moghaddam, M. L. Lai, P. Docampo, R. Higler, F. Deschler, M. Price, A. Sadhanala, L. M. Pazos, D. Credgington, F. Hanusch, T. Bein, H. J. Snaith, and R. H. Friend, "Bright light-emitting diodes based on organometal halide perovskite," *Nat. Nanotechnol.*, vol. 9, pp. 687–692, 2014.

[50] S. K. Lukas Schmidt-Mende, Azhar Fakharuddin, *Organic and Hybrid Solar Cells*, 2nd ed. De Gruyter, 2022. [Online]. Available: http://gen.lib.rus.ec/book/index.php?md5=88F4BEBF5F1CB5FFDD0CA16229552EE2

[51] C. Eames, J. M. Frost, P. R. Barnes, B. C. O'regan, A. Walsh, and M. S. Islam, "Ionic transport in hybrid lead iodide perovskite solar cells," *Nat. Commun.*, vol. 6, no. 1, p. 7497, 2015.

[52] B. Conings, J. Drijkoningen, N. Gauquelin, A. Babayigit, J. D'Haen, L. D'Olieslaeger, A. Ethirajan, J. Verbeeck, J. Manca, E. Mosconi *et al.*, "Intrinsic thermal instability of methylammonium lead trihalide perovskite," *Adv. Energy Mater.*, vol. 5, no. 15, p. 1500477, 2015.

[53] G. Divitini, S. Cacovich, F. Matteocci, L. Cinà, A. Di Carlo, and C. Ducati, "In situ observation of heat-induced degradation of perovskite solar cells," *Nat. Energy*, vol. 1, no. 2, p. 15012, 2016.

[54] N. Aristidou, C. Eames, I. Sanchez-Molina, X. Bu, J. Kosco, M. S. Islam, and S. A. Haque, "Fast oxygen diffusion and iodide defects mediate oxygen-induced degradation of perovskite solar cells," *Nat. Commun.*, vol. 8, no. 1, p. 15218, 2017.

[55] N. Aristidou, I. Sanchez-Molina, T. Chotchuangchutchaval, M. Brown, L. Martinez, T. Rath, and S. A. Haque, "The role of oxygen in the degradation of methylammonium lead trihalide perovskite photoactive layers," *Angew. Chem.*, vol. 127, no. 28, pp. 8326–8330, 2015.

[56] A. Arakcheeva, D. Chernyshov, M. Spina, L. Forró, and E. Horváth, "$CH_3NH_3PbI_3$: precise structural consequences of water absorption at ambient conditions," *Acta Crystallogr., Sect. B*, vol. 72, no. 5, pp. 716–722, 2016.

[57] Y. Zhao, J. Wei, H. Li, Y. Yan, W. Zhou, D. Yu, and Q. Zhao, "A polymer scaffold for self-healing perovskite solar cells," *Nat. Commun.*, vol. 7, no. 1, p. 10228, 2016.

[58] G. Abdelmageed, L. Jewell, K. Hellier, L. Seymour, B. Luo, F. Bridges, J. Z. Zhang, and S. Carter, "Mechanisms for light induced degradation in $MAPbI_3$ perovskite thin films and solar cells," *Appl. Phys. Lett.*, vol. 109, no. 23, 2016.

[59] A. Senocrate, T. Acartürk, G. Y. Kim, R. Merkle, U. Starke, M. Grätzel, and J. Maier, "Interaction of oxygen with halide perovskites," *J. Mater. Chem. A*, vol. 6, pp. 10 847–10 855, 2018.

[60] J. Liang, C. Wang, Y. Wang, Z. Xu, Z. Lu, Y. Ma, H. Zhu, Y. Hu, C. Xiao, X. Yi *et al.*, "All-inorganic perovskite solar cells," *J. Am. Chem. Soc.*, vol. 138, no. 49, pp. 15 829–15 832, 2016.

[61] Y. Han, S. Meyer, Y. Dkhissi, K. Weber, J. M. Pringle, U. Bach, L. Spiccia, and Y.-B. Cheng, "Degradation observations of encapsulated planar $CH_3NH_3PbI_3$ perovskite solar cells at high temperatures and humidity," *J. Mater. Chem. A*, vol. 3, no. 15, pp. 8139–8147, 2015.

[62] Q. Jiang, Y. Zhao, X. Zhang, X. Yang, Y. Chen, Z. Chu, Q. Ye, X. Li, Z. Yin, and J. You, "Surface passivation of perovskite film for efficient solar cells," *Nat. Photonics*, vol. 13, no. 7, pp. 460–466, 2019.

[63] W.-J. Yin, T. Shi, and Y. Yan, "Unusual defect physics in $CH_3NH_3PbI_3$ perovskite solar cell absorber," *Appl. Phys. Lett.*, vol. 104, no. 6, 2014.

[64] M. Zhang, Z. Zheng, Q. Fu, P. Guo, S. Zhang, C. Chen, H. Chen, M. Wang, W. Luo, and Y. Tian, "Determination of Defect Levels in Melt-Grown All-Inorganic Perovskite $CsPbBr_3$ Crystals by Thermally Stimulated Current Spectra," *J. Phys. Chem. C*, vol. 122, no. 19, pp. 10 309–10 315, 2018.

[65] K. X. Steirer, P. Schulz, G. Teeter, V. Stevanovic, M. Yang, K. Zhu, and J. J. Berry, "Defect tolerance in methylammonium lead triiodide perovskite," *ACS Energy Lett.*, vol. 1, no. 2, pp. 360–366, 2016.

[66] E. Mosconi, P. Umari, and F. De Angelis, "Electronic and optical properties of $MAPbX_3$ perovskites (X= I, Br, Cl): a unified DFT and GW theoretical analysis," *Phys. Chem. Chem. Phys.*, vol. 18, no. 39, pp. 27 158–27 164, 2016.

[67] Y. Liu, Z. Yang, D. Cui, X. Ren, J. Sun, X. Liu, J. Zhang, Q. Wei, H. Fan, F. Yu, X. Zhang, C. Zhao, and S. F. Liu, "Two-Inch-Sized Perovskite $CH_3NH_3PbX_3$ (X = Cl, Br, I) Crystals: Growth and Characterization," *Adv. Mater.*, vol. 27, no. 35, pp. 5176–5183, 2015.

[68] J.-S. Park, S. Choi, Y. Yan, Y. Yang, J. M. Luther, S.-H. Wei, P. Parilla, and K. Zhu, "Electronic Structure and Optical Properties of α-$CH_3NH_3PbBr_3$ Perovskite Single Crystal," *J. Phys. Chem. Lett.*, vol. 6, no. 21, pp. 4304–4308, 2015.

[69] C. Quarti, E. Mosconi, and F. De Angelis, "Interplay of Orientational Order and Electronic Structure in Methylammonium Lead Iodide: Implications for Solar Cell Operation," *Chem. Mater.*, vol. 26, no. 22, pp. 6557–6569, 2014.

[70] A. Poglitsch and D. Weber, "Dynamic disorder in methylammoniumtrihalogenoplumbates (ii) observed by millimeter-wave spectroscopy," *J. Chem. Phys.*, vol. 87, no. 11, pp. 6373–6378, 1987.

[71] A. Osherov, E. M. Hutter, K. Galkowski, R. Brenes, D. K. Maude, R. J. Nicholas, P. Plochocka, V. Bulović, T. J. Savenije, and S. D. Stranks, "The Impact of Phase Retention on the Structural and Optoelectronic Properties of Metal Halide Perovskites," *Adv. Mater.*, vol. 28, no. 48, pp. 10 757–10 763, 2016.

[72] D. Li, G. Wang, H.-C. Cheng, C.-Y. Chen, H. Wu, Y. Liu, Y. Huang, and X. Duan, "Size-dependent phase transition in methylammonium lead iodide perovskite microplate crystals," *Nat. Commun.*, vol. 7, no. 1, p. 11330, 2016.

[73] C. Wehrenfennig, M. Liu, H. J. Snaith, M. B. Johnston, and L. M. Herz, "Charge carrier recombination channels in the low-temperature phase of organic-inorganic lead halide perovskite thin films," *APL Mater.*, vol. 2, no. 8, p. 081513, 2014.

[74] M. Pitaro, E. K. Tekelenburg, S. Shao, and M. A. Loi, "Tin Halide Perovskites: From Fundamental Properties to Solar Cells," *Adv. Mater.*, vol. 34, no. 1, p. 2105844, 2022. [Online]. Available: https://onlinelibrary.wiley.com/doi/abs/10.1002/adma.202105844

[75] T. Chen, B. J. Foley, B. Ipek, M. Tyagi, J. R. D. Copley, C. M. Brown, J. J. Choi, and S.-H. Lee, "Rotational dynamics of organic cations in the $CH_3NH_3PbI_3$ perovskite," *Phys. Chem. Chem. Phys.*, vol. 17, pp. 31 278–31 286, 2015.

[76] G. M. Bernard, R. E. Wasylishen, C. I. Ratcliffe, V. Terskikh, Q. Wu, J. M. Buriak, and T. Hauger, "Methylammonium Cation Dynamics in Methylammonium Lead Halide Perovskites: A Solid-State NMR Perspective," *J. Phys. Chem. A*, vol. 122, no. 6, pp. 1560–1573, 2018.

[77] F. Brivio, J. M. Frost, J. M. Skelton, A. J. Jackson, O. J. Weber, M. T. Weller, A. R. Goñi, A. M. A. Leguy, P. R. F. Barnes, and A. Walsh, "Lattice dynamics and vibrational spectra of the orthorhombic, tetragonal, and cubic phases of methylammonium lead iodide," *Phys. Rev. B*, vol. 92, p. 144308, 2015.

[78] M. T. Weller, O. J. Weber, P. F. Henry, A. M. Di Pumpo, and T. C. Hansen, "Complete structure and cation orientation in the perovskite photovoltaic methylammonium lead iodide between 100 and 352 K," *Chem. Commun.*, vol. 51, pp. 4180–4183, 2015.

[79] R. Wasylishen, O. Knop, and J. Macdonald, "Cation rotation in methylammonium lead halides," *Solid State Commun.*, vol. 56, no. 7, pp. 581 – 582, 1985.

[80] M. C. Gélvez-Rueda, D. H. Cao, S. Patwardhan, N. Renaud, C. C. Stoumpos, G. C. Schatz, J. T. Hupp, O. K. Farha, T. J. Savenije, M. G. Kanatzidis, and F. C. Grozema, "Effect of Cation Rotation on Charge Dynamics in Hybrid Lead Halide Perovskites," *J. Phys. Chem. C*, vol. 120, no. 30, pp. 16 577–16 585, 2016.

[81] J. M. Frost, K. T. Butler, F. Brivio, C. H. Hendon, M. van Schilfgaarde, and A. Walsh, "Atomistic Origins of High-Performance in Hybrid Halide Perovskite Solar Cells," *Nano Lett.*, vol. 14, no. 5, pp. 2584–2590, 2014.

[82] A. M. A. Leguy, J. M. Frost, A. P. McMahon, V. G. Sakai, W. Kockelmann, C. Law, X. Li, F. Foglia, A. Walsh, B. C. O'Regan, J. Nelson, J. T. Cabral, and P. R. F. Barnes, "The dynamics of methylammonium ions in hybrid organic-inorganic perovskite solar cells," *Nat. Commun.*, vol. 6, p. 7124, 2015.

[83] H.-S. Kim, S. K. Kim, B. J. Kim, K.-S. Shin, M. K. Gupta, H. S. Jung, S.-W. Kim, and N.-G. Park, "Ferroelectric Polarization in $CH_3NH_3PbI_3$ Perovskite," *J. Phys. Chem. Lett.*, vol. 6, no. 9, pp. 1729–1735, 2015.

[84] Y. Kutes, L. Ye, Y. Zhou, S. Pang, B. D. Huey, and N. P. Padture, "Direct Observation of Ferroelectric Domains in Solution-Processed $CH_3NH_3PbI_3$ Perovskite Thin Films," *J. Phys. Chem. Lett.*, vol. 5, no. 19, pp. 3335–3339, 2014.

[85] C. K. MØLLER, "Crystal Structure and Photoconductivity of Cæsium Plumbohalides," *Nature*, vol. 182, no. 4647, pp. 1436–1436, Nov 1958. [Online]. Available: https://doi.org/10.1038/1821436a0

[86] J. Zhang, Q. Wang, X. Zhang, J. Jiang, Z. Gao, Z. Jin, and S. F. Liu, "High-performance transparent ultraviolet photodetectors based on inorganic perovskite CsPbCl 3 nanocrystals," *RSC Adv.*, vol. 7, no. 58, pp. 36 722–36 727, 2017.

[87] S. Dastidar, C. J. Hawley, A. D. Dillon, A. D. Gutierrez-Perez, J. E. Spanier, and A. T. Fafarman, "Quantitative Phase-Change Thermodynamics and Metastability of Perovskite-Phase Cesium Lead Iodide," *J. Phys. Chem. Lett.*, vol. 8, no. 6, pp. 1278–1282, 2017, pMID: 28256139. [Online]. Available: https://doi.org/10.1021/acs.jpclett.7b00134

[88] F. Gabelloni, F. Biccari, G. Andreotti, D. Balestri, S. Checcucci, A. Milanesi, N. Calisi, S. Caporali, and A. Vinattieri, "Recombination dynamics in $CsPbBr_3$ nanocrystals: role of surface states," *Opt. Mater. Express*, vol. 7, no. 12, pp. 4367–4373, 2017.

[89] Y. Yuan, M. Chen, S. Yang, X. Shen, Y. Liu, and D. Cao, "Exciton recombination mechanisms in solution grown single crystalline $CsPbBr_3$ perovskite," *J. Lumin.*, vol. 226, p. 117471, 2020.

[90] X. Lao, Z. Yang, Z. Su, Z. Wang, H. Ye, M. Wang, X. Yao, and S. Xu, "Luminescence and thermal behaviors of free and trapped excitons in cesium lead halide perovskite nanosheets," *Nanoscale*, vol. 10, pp. 9949–9956, 2018.

[91] M. Liao, B. Shan, and M. Li, "Role of Trap States in Excitation Wavelength-Dependent Photoluminescence of Strongly Quantum-Confined All-Inorganic $CsPbBr_3$ Perovskites

with Varying Dimensionalities," *J. Phys. Chem. C*, vol. 125, no. 38, pp. 21 062–21 069, 2021.

[92] Q. A. Akkerman, S. G. Motti, A. R. Srimath Kandada, E. Mosconi, V. D'Innocenzo, G. Bertoni, S. Marras, B. A. Kamino, L. Miranda, F. De Angelis, A. Petrozza, M. Prato, and L. Manna, "Solution Synthesis Approach to Colloidal Cesium Lead Halide Perovskite Nanoplatelets with Monolayer-Level Thickness Control," *J. Am. Chem. Soc.*, vol. 138, no. 3, pp. 1010–1016, 2016.

[93] Z. Liang, S. Zhao, Z. Xu, B. Qiao, P. Song, D. Gao, and X. Xu, "Shape-Controlled Synthesis of All-Inorganic $CsPbBr_3$ Perovskite Nanocrystals with Bright Blue Emission," *ACS Appl. Mater. Interfaces*, vol. 8, no. 42, pp. 28 824–28 830, 2016.

[94] S. Hirotsu, J. Harada, M. Iizumi, and K. Gesi, "Structural Phase Transitions in $CsPbBr_3$," *J. Phys. Soc. Jpn.*, vol. 37, no. 5, pp. 1393–1398, 1974.

[95] J. Kang and L.-W. Wang, "High Defect Tolerance in Lead Halide Perovskite $CsPbBr_3$," *J. Phys. Chem. Lett.*, vol. 8, no. 2, pp. 489–493, 2017.

[96] X. Liu, Z. Liu, J. Li, X. Tan, B. Sun, H. Fang, S. Xi, T. Shi, Z. Tang, and G. Liao, "Ultrafast, self-powered and charge-transport-layer-free photodetectors based on high-quality evaporated $CsPbBr_3$ perovskites for applications in optical communication," *J. Mater. Chem. C*, vol. 8, pp. 3337–3350, 2020. [Online]. Available: http://dx.doi.org/10.1039/C9TC06630F

[97] N. Lobo, T. Kawane, G. J. Matt, A. Osvet, S. Shrestha, L. Ievgen, C. J. Brabec, A. Kanak, P. Fochuk, and M. Kato, "Trapping effects and surface/interface recombination of carrier recombination in single- or poly-crystalline metal halide perovskites," *Jpn. J. Appl. Phys.*, vol. 61, no. 12, p. 125503, 2022.

[98] A. Bojtor, D. Krisztián, F. Korsós, S. Kollarics, G. Paráda, T. Pinel, M. Kollár, E. Horváth, X. Mettan, H. Shiozawa, B. G. Márkus, L. Forró, and F. Simon, "Millisecond-Scale Charge-Carrier Recombination Dynamics in the $CsPbBr_3$ Perovskite," *Adv. Energy Sustainability Res.*, p. 2400043.

[99] A. Al-Ashouri, E. Köhnen, B. Li, A. Magomedov, H. Hempel, P. Caprioglio, J. A. Márquez, A. B. Morales Vilches, E. Kasparavicius, J. A. Smith *et al.*, "Monolithic perovskite/silicon tandem solar cell with> 29% efficiency by enhanced hole extraction," *Science*, vol. 370, no. 6522, pp. 1300–1309, 2020.

[100] J. Werner, B. Niesen, and C. Ballif, "Perovskite/silicon tandem solar cells: marriage of convenience or true love story?–An overview," *Adv. Mater. Interfaces*, vol. 5, no. 1, p. 1700731, 2018.

[101] W. Ahmad, J. Khan, G. Niu, and J. Tang, "Inorganic $CsPbI_3$ Perovskite-Based Solar Cells: A Choice for a Tandem Device," *Sol. RRL*, vol. 1, no. 7, p. 1700048, 2017. [Online]. Available: https://onlinelibrary.wiley.com/doi/abs/10.1002/solr.201700048

[102] S. Yuvaraja, V. Khandelwal, X. Tang, and X. Li, "Wide bandgap semiconductor-based integrated circuits," *Chip*, vol. 2, no. 4, p. 100072, 2023. [Online]. Available: https://www.sciencedirect.com/science/article/pii/S2709472323000357

[103] B.-D. Yang, J.-M. Oh, H.-J. Kang, S.-H. Park, C.-S. Hwang, M. K. Ryu, and J.-E. Pi, "A Transparent Logic Circuit for RFID Tag in a-IGZO TFT Technology," *ETRI Journal*, vol. 35, no. 4, pp. 610–616, 2013. [Online]. Available: https://onlinelibrary.wiley.com/doi/abs/10.4218/etrij.13.1912.0004

[104] J. Glaab, J. Ruschel, N. Lobo Ploch, H. K. Cho, F. Mehnke, L. Sulmoni, M. Guttmann, T. Wernicke, M. Weyers, S. Einfeldt, and M. Kneissl, "Impact of operation parameters on the degradation of 233nm AlGaN-based far-UVC LEDs," *J. Appl. Phys.*, vol. 131, no. 1, p. 014501, 01 2022. [Online]. Available: https://doi.org/10.1063/5.0069590

[105] N. Kimizuka and T. Mohri, "Spinel, $YbFe_2O_4$, and $Yb_2Fe_3O_7$ types of structures for compounds in the In_2O_3 and Sc_2O_3 A_2O_3 BO systems [A: Fe, Ga, or Al; B: Mg, Mn, Fe, Ni, Cu, or Zn] at temperatures over 1000° C," *J. Solid State Chem.*, vol. 60, no. 3, pp. 382–384, 1985.

[106] C.-W. Chen, T.-C. Chang, P.-T. Liu, H.-Y. Lu, K.-C. Wang, C.-S. Huang, C.-C. Ling, and T.-Y. Tseng, "High-performance hydrogenated amorphous-Si TFT for AMLCD and AMOLED applications," *IEEE Electron Device Letters*, vol. 26, no. 10, pp. 731–733, 2005.

[107] T.-C. Chang, Y.-C. Tsao, P.-H. Chen, M.-C. Tai, S.-P. Huang, W.-C. Su, and G.-F. Chen, "Flexible low-temperature polycrystalline silicon thin-film transistors," *Mater. Today Adv.*, vol. 5, p. 100040, 2020. [Online]. Available: https://www.sciencedirect.com/science/article/pii/S2590049819301146

[108] J. Yu, K. Javaid, L. Liang, W. Wu, Y. Liang, A. Song, H. Zhang, W. Shi, T.-C. Chang, and H. Cao, "High-performance visible-blind ultraviolet photodetector based on IGZO TFT coupled with p–n heterojunction," *ACS Appl. Mater. Interfaces*, vol. 10, no. 9, pp. 8102–8109, 2018.

[109] T. Kamiya, K. Nomura, and H. Hosono, "Electronic structures above mobility edges in crystalline and amorphous In-Ga-Zn-O: Percolation conduction examined by analytical model," *J. Disp. Technol.*, vol. 5, no. 12, pp. 462–467, 2009.

[110] R. Roy, V. G. Hill, and E. F. Osborn, "Polymorphism of Ga_2O_3 and the System Ga_2O_3—H_2O," *J. Am. Chem. Soc.*, vol. 74, no. 3, pp. 719–722, 1952. [Online]. Available: https://doi.org/10.1021/ja01123a039

[111] M. Higashiwaki and S. Fujita, *Gallium Oxide: Materials Properties, Crystal Growth, and Devices*. Springer Nature, 2020, vol. 293.

[112] D. Shinohara and S. Fujita, "Heteroepitaxy of Corundum-Structured α-Ga_2O_3 Thin Films on α-Al_2O_3 Substrates by Ultrasonic Mist Chemical Vapor Deposition," *Jpn. J. Appl. Phys.*, vol. 47, no. 9R, p. 7311, sep 2008. [Online]. Available: https://dx.doi.org/10.1143/JJAP.47.7311

[113] Y. Oshima, E. G. Víllora, and K. Shimamura, "Halide vapor phase epitaxy of twin-free α-Ga_2O_3 on sapphire (0001) substrates," *Appl. Phys. Express*, vol. 8, no. 5, p. 055501, apr 2015. [Online]. Available: https://dx.doi.org/10.7567/APEX.8.055501

[114] S. Jeon, S.-E. Ahn, I. Song, C. J. Kim, U.-I. Chung, E. Lee, I. Yoo, A. Nathan, S. Lee, K. Ghaffarzadeh *et al.*, "Gated three-terminal device architecture to eliminate persistent photoconductivity in oxide semiconductor photosensor arrays," *Nat. Mater.*, vol. 11, no. 4, pp. 301–305, 2012.

[115] W.-J. Lee, B. Ryu, and K.-J. Chang, "Electronic structure of oxygen vacancy in crystalline $InGaO_3(ZnO)_m$," *Phys. B*, vol. 404, no. 23-24, pp. 4794–4796, 2009.

[116] M. Lee, K.-T. Kim, M. Lee, S. K. Park, and Y.-H. Kim, "A study on the persistent photoconductance and transient photo-response characteristics of photochemically activated and thermally annealed indium-gallium-zinc-oxide thin-film transistors," *Thin Solid Films*, vol. 660, pp. 749–753, 2018.

[117] S.-L. Gao, L.-P. Qiu, J. Zhang, W.-P. Han, S. Ramakrishna, and Y.-Z. Long, "Persistent Photoconductivity of Metal Oxide Semiconductors," *ACS Appl. Electron. Mater.*, vol. 6, no. 3, pp. 1542–1561, 2024. [Online]. Available: https://doi.org/10.1021/acsaelm.3c01549

[118] A. Bojtor, G. Paráda, P. Tüttő, H. Korka, K. Szőke, and F. Korsós, "Investigation of Persistent Photoconductance and Related Electron Mobility in Thin IGZO Layers With the PDL Hall Technique," *Mater. Today: Proc.*, vol. 93, pp. 9–15, 2023, international Conferences & Exhibition on Nanotechnologies, Organic Electronics & Nanomedicine – Nanotexnology (NANOTEX 2022).

[119] S. Cui, Z. Mei, Y. Zhang, H. Liang, and X. Du, "Room-Temperature Fabricated Amorphous Ga_2O_3 High-Response-Speed Solar-Blind Photodetector on Rigid and Flexible Substrates," *Adv. Opt. Mater.*, vol. 5, no. 19, p. 1700454, 2017. [Online]. Available: https://onlinelibrary.wiley.com/doi/abs/10.1002/adom.201700454

[120] H. Liang, S. Cui, R. Su, P. Guan, Y. He, L. Yang, L. Chen, Y. Zhang, Z. Mei, and X. Du, "Flexible X-ray Detectors Based on Amorphous Ga_2O_3 Thin Films," *ACS Photonics*, vol. 6, no. 2, pp. 351–359, 2019. [Online]. Available: https://doi.org/10.1021/acsphotonics.8b00769

[121] H. Zhou, L. Cong, J. Ma, B. Li, M. Chen, H. Xu, and Y. Liu, "High gain broadband photoconductor based on amorphous Ga_2O_3 and suppression of persistent photoconductivity," *J. Mater. Chem. C*, vol. 7, pp. 13 149–13 155, 2019. [Online]. Available: http://dx.doi.org/10.1039/C9TC05159G

[122] R. Zhu, H. Liang, S. Hu, Y. Wang, and Z. Mei, "Amorphous-Ga_2O_3 Optoelectronic Synapses with Ultra-low Energy Consumption," *Adv. Electron. Mater.*, vol. 8, no. 1, p. 2100741, 2022. [Online]. Available: https://onlinelibrary.wiley.com/doi/abs/10.1002/aelm.202100741

[123] J. T. Jang, D. Ko, S. Choi, H. Kang, J.-Y. Kim, H. R. Yu, G. Ahn, H. Jung, J. Rhee, H. Lee *et al.*, "Effects of structure and oxygen flow rate on the photo-response of amorphous IGZO-based photodetector devices," *Solid-State Electron.*, vol. 140, pp. 115–121, 2018.

[124] M. Mativenga, F. Haque, M. M. Billah, and J. G. Um, "Origin of light instability in amorphous IGZO thin-film transistors and its suppression," *Sci. Rep.*, vol. 11, no. 1, p. 14618, 2021.

[125] M. Mativenga, J. G. Um, and J. Jang, "Reduction of bias and light instability of mixed oxide thin-film transistors," *Appl. Sci.*, vol. 7, no. 9, p. 885, 2017.

[126] H.-K. Noh, K.-J. Chang, B. Ryu, and W.-J. Lee, "Electronic structure of oxygen-vacancy defects in amorphous In-Ga-Zn-O semiconductors," *Phys. Rev. B*, vol. 84, no. 11, p. 115205, 2011.

[127] M. D. H. Chowdhury, P. Migliorato, and J. Jang, "Light induced instabilities in amorphous indium–gallium–zinc–oxide thin-film transistors," *Appl. Phys. Lett.*, vol. 97, no. 17, 2010.

[128] S. Lany and A. Zunger, "Anion vacancies as a source of persistent photoconductivity in II-VI and chalcopyrite semiconductors," *Phys. Rev. B*, vol. 72, no. 3, p. 035215, 2005.

[129] W. Shockley and W. T. Read, "Statistics of the Recombinations of Holes and Electrons," *Phys. Rev.*, vol. 87, pp. 835–842, 1952.

[130] R. Hall, "Recombination processes in semiconductors," *Proc. Inst. Electr. Eng., Part B*, vol. 106, pp. 923–931(8), 1959.

[131] R. N. Hall, "Electron-hole recombination in germanium," *Phys. Rev.*, vol. 87, no. 2, p. 387, 1952.

[132] S. Rein, *Lifetime Spectroscopy*, 1st ed. Springer Berlin, Heidelberg, 2005.

[133] D. Schroder, *Semiconductor Material and Device Characterization*, ser. IEEE Press. Wiley, 2006. [Online]. Available: https://books.google.hu/books?id=OX2cHKJWCKgC

[134] A. Hangleiter and R. Häcker, "Enhancement of band-to-band Auger recombination by electron-hole correlations," *Phys. Rev. Lett.*, vol. 65, pp. 215–218, Jul 1990. [Online]. Available: https://link.aps.org/doi/10.1103/PhysRevLett.65.215

[135] K. Lauer, *Untersuchungen zur Ladungsträgerlebensdauer in kristallinem Silizium für Solarzellen*. Universitätsverlag Ilmenau, 2005.

[136] A. Sproul, "Dimensionless solution of the equation describing the effect of surface recombination on carrier decay in semiconductors," *J. Appl. Phys.*, vol. 76, no. 5, pp. 2851–2854, 1994.

[137] A. G. Aberle, "Surface passivation of crystalline silicon solar cells: a review," *Prog. Photovoltaics*, vol. 8, no. 5, pp. 473–487, 2000. [Online]. Available: https://onlinelibrary.wiley.com/doi/abs/10.1002/1099-159X%28200009/10%298%3A5%3C473%3A%3AAID-PIP337%3E3.0.CO%3B2-D

[138] L. Meng, T. Zeng, Y. Jin, Q. Xu, and X. Wang, "Surface-Modified Substrates for Quantum Dot Inks in Printed Electronics," *ACS Omega*, vol. 4, no. 2, pp. 4161–4168, 2019, pMID: 31459625. [Online]. Available: https://doi.org/10.1021/acsomega.9b00195

[139] Y. Zhang, T. Guo, H. Yang, R. Bose, L. Liu, J. Yin, Y. Han, O. M. Bakr, O. F. Mohammed, and A. V. Malko, "Emergence of multiple fluorophores in individual cesium lead bromide nanocrystals," *Nat. Commun.*, vol. 10, no. 1, p. 2930, 2019.

[140] X. Zhang, G. Pang, G. Xing, and R. Chen, "Temperature dependent optical characteristics of all-inorganic $CsPbBr_3$ nanocrystals film," *Mater. Today Phys.*, vol. 15, p. 100259, 2020.

[141] M. C. Gélvez-Rueda, M. B. Fridriksson, R. K. Dubey, W. F. Jager, W. van der Stam, and F. C. Grozema, "Overcoming the exciton binding energy in two-dimensional perovskite nanoplatelets by attachment of conjugated organic chromophores," *Nat. Commun.*, vol. 11, no. 1, p. 1901, 2020.

[142] Y. Li, Z. Jia, Y. Yang, F. Yao, Y. Liu, and Q. Lin, "Shallow traps-induced ultra-long lifetime of metal halide perovskites probed with light-biased time-resolved microwave conductivity," *Appl. Phys. Rev.*, vol. 10, no. 1, p. 011406, 01 2023. [Online]. Available: https://doi.org/10.1063/5.0129883

[143] T. J. Savenije, D. Guo, V. M. Caselli, and E. M. Hutter, "Quantifying Charge-Carrier Mobilities and Recombination Rates in Metal Halide Perovskites from Time-Resolved Microwave Photoconductivity Measurements," *Adv. Energy Mater.*, vol. 10, no. 26, p. 1903788, 2020. [Online]. Available: https://onlinelibrary.wiley.com/doi/abs/10.1002/aenm.201903788

[144] F. Yao and Q. Lin, "Charge Carrier Dynamics of Organic Cation-Treated Perovskites Probed with Time-Resolved Microwave Conductivity," *ACS Photonics*, vol. 9, no. 9, pp. 3165–3171, 2022. [Online]. Available: https://doi.org/10.1021/acsphotonics.2c01132

[145] Y. Bi, E. M. Hutter, Y. Fang, Q. Dong, J. Huang, and T. J. Savenije, "Charge Carrier Lifetimes Exceeding 15 μs in Methylammonium Lead Iodide Single Crystals," *J. Phys. Chem. Lett.*, vol. 7, no. 5, pp. 923–928, 2016.

[146] A. S. Chouhan, N. P. Jasti, S. Hadke, S. Raghavan, and S. Avasthi, "Large grained and high charge carrier lifetime $CH_3NH_3PbI_3$ thin- films: implications for perovskite solar cells," *Curr. Appl. Phys.*, vol. 17, no. 10, pp. 1335 – 1340, 2017.

[147] B. Gyüre-Garami, B. Blum, O. Sági, A. Bojtor, S. Kollarics, G. Csősz, B. G. Márkus, J. Volk, and F. Simon, "Ultrafast sensing of photoconductivity decay using microwave resonators," *J. Appl. Phys.*, vol. 126, no. 23, p. 235702, 2019.

[148] M. Kunst and G. Beck, "The study of charge carrier kinetics in semiconductors by microwave conductivity measurements," *J. Appl. Phys.*, vol. 60, no. 10, pp. 3558–3566, 1986.

[149] M. Kunst and G. Beck, "The study of charge carrier kinetics in semiconductors by microwave conductivity measurements. II." *J. Appl. Phys.*, vol. 63, no. 4, pp. 1093–1098, 1988.

[150] K. Lauer, A. Laades, H. Übensee, H. Metzner, and A. Lawerenz, "Detailed analysis of the microwave-detected photoconductance decay in crystalline silicon," *J. Appl. Phys.*, vol. 104, no. 10, 2008.

[151] A. Sanders and M. Kunst, "Characterization of silicon wafers by transient microwave photoconductivity measurements," *Solid-State Electron.*, vol. 34, no. 9, pp. 1007–1015, 1991. [Online]. Available: https://www.sciencedirect.com/science/article/pii/003811019190220S

[152] D. Pozar, *Microwave Engineering - Solutions Manual*. Wiley, 2011, vol. 4 ed.

[153] L. Chen, C. Ong, C. Neo, V. Varadan, and V. Varadan, *Microwave Electronics: Measurement and Materials Characterization*. Wiley, 2004. [Online]. Available: https://books.google.hu/books?id=1vmUdUXlBNIC

[154] J. C. Booth, D. H. Wu, and S. M. Anlage, "A broadband method for the measurement of the surface impedance of thin films at microwave frequencies," *Rev. Sci. Instrum.*, vol. 65, no. 6, pp. 2082–2090, 06 1994. [Online]. Available: https://doi.org/10.1063/1.1144816

[155] O. Klein, S. Donovan, M. Dressel, and G. Grüner, "Microwave cavity perturbation technique: Part I: Principles," *Int. J. Infrared Millimeter Waves*, vol. 14, no. 12, pp. 2423–2457, 1993.

[156] L. Landau, J. Bell, M. Kearsley, L. Pitaevskii, E. Lifshitz, and J. Sykes, *Electrodynamics of Continuous Media*, ser. Course Of Theoretical Physics. Elsevier Science, 2013.

[157] R. A. Sinton, A. Cuevas, and M. Stuckings, "Quasi-steady-state photoconductance, a new method for solar cell material and device characterization," in *Conference Record of the Twenty Fifth IEEE Photovoltaic Specialists Conference - 1996*, 1996, pp. 457–460.

[158] M. Goodarzi, R. Sinton, and D. Macdonald, "Quasi-steady-state photoconductance bulk lifetime measurements on silicon ingots with deeper photogeneration," *AIP Adv.*, vol. 9, no. 1, p. 015128, 2019.

[159] M. Wilson, A. Savtchouk, J. Lagowski, K. Kis-Szabo, F. Korsos, A. Toth, R. Kopecek, and V. Mihailetchi, "QSS-μPCD measurement of lifetime in silicon wafers: advantages and new applications," *Energy Procedia*, vol. 8, pp. 128–134, 2011.

[160] A. Bojtor, S. Kollarics, B. G. Márkus, A. Sienkiewicz, M. Kollár, L. Forró, and F. Simon, "Ultralong charge carrier recombination time in methylammonium lead halide perovskites," *ACS Photonics*, vol. 9, no. 10, pp. 3341–3350, 2022.

[161] S. Bowden and R. A. Sinton, "Determining lifetime in silicon blocks and wafers with accurate expressions for carrier density," *J. Appl. Phys.*, vol. 102, no. 12, 2007.

[162] J. Bisquert, F. Fabregat-Santiago, I. Mora-Seró, G. Garcia-Belmonte, and S. Giménez, "Electron Lifetime in Dye-Sensitized Solar Cells: Theory and Interpretation of Measurements," *J. Phys. Chem. C*, vol. 113, no. 40, pp. 17 278–17 290, 2009.

[163] L. J. van der Pauw, "A method of measuring specific resistivity and Hall effect of discs of arbitrary shape," *Philips Res. Rep*, vol. 13, no. 1, pp. 1–9, 1958.

[164] E. H. Hall, "On a New Action of the Magnet on Electric Currents," *Am. J. Math.*, vol. 2, no. 3, pp. 287–292, 1879. [Online]. Available: http://www.jstor.org/stable/2369245

[165] R. Smith, *Semiconductors*. Cambridge University Press, 1964. [Online]. Available: https://books.google.hu/books?id=__RjnQEACAAJ

[166] S. Kasap, "Hall effect in semiconductors."

[167] G. Ohm, *Die galvanische Kette, mathematisch bearbeitet*, ser. Landmarks of Science. Riemann, 1827. [Online]. Available: https://books.google.hu/books?id=wBtkAAAAcAAJ

[168] R. N. Simons, *Coplanar Waveguide Circuits Components & Systems*, 1st ed. Wiley-IEEE Press, 2001.

[169] F. Gustrau, *RF and Microwave Engineering: Fundamentals of Wireless Communications*, 1st ed. Wiley, 2012.

[170] MarkiMicrowave. Functional block diagram. [Online]. Available: https://markimicrowave.com/products/connectorized/iq-mixers/iq-0618lxp/datasheet/

[171] R. Janes, M. Edge, J. Robinson, N. S. Allen, and F. Thompson, "Microwave photodielectric and photoconductivity studies of commercial titanium dioxide pigments: the influence of transition metal dopants," *J. Mater. Sci.*, vol. 33, no. 12, pp. 3031–3036, 1998.

[172] T. J. Savenije, A. J. Ferguson, N. Kopidakis, and G. Rumbles, "Revealing the Dynamics of Charge Carriers in Polymer:Fullerene Blends Using Photoinduced Time-Resolved Microwave Conductivity," *J. Phys. Chem. C*, vol. 117, no. 46, pp. 24 085–24 103, 2013.

[173] T. J. Savenije, D. Guo, V. M. Caselli, and E. M. Hutter, "Quantifying Charge-Carrier Mobilities and Recombination Rates in Metal Halide Perovskites from Time-Resolved Microwave Photoconductivity Measurements," *Adv. Energy Mater.*, vol. 10, no. 26, p. 1903788, 2020.

[174] Semilab Zrt. Pdl-1000. [Online]. Available: https://semilab.com/category/products/ac-field-parallel-dipole-line-hall-measurement

[175] O. Gunawan, Y. Virgus, and K. F. Tai, "A parallel dipole line system," *Appl. Phys. Lett.*, vol. 106, no. 6, p. 062407, 02 2015. [Online]. Available: https://doi.org/10.1063/1.4907931

[176] B. Náfrádi, P. Szirmai, M. Spina, H. Lee, O. V. Yazyev, A. Arakcheeva, D. Chernyshov, M. Gibert, L. Forró, and E. Horváth, "Optically switched magnetism in photovoltaic perovskite CH_3NH_3(Mn:Pb)I_3," *Nat. Commun.*, vol. 7, p. 13406, 2016.

[177] M. I. Saidaminov, A. L. Abdelhady, G. Maculan, and O. M. Bakr, "Retrograde solubility of formamidinium and methylammonium lead halide perovskites enabling rapid single crystal growth," *Chem. Commun.*, vol. 51, pp. 17 658–17 661, 2015.

[178] M. I. Saidaminov, A. L. Abdelhady, B. Murali, E. Alarousu, V. M. Burlakov, W. Peng, I. Dursun, L. Wang, Y. He, G. Maculan, A. Goriely, T. Wu, O. F. Mohammed, and O. M. Bakr, "High-quality bulk hybrid perovskite single crystals within minutes by inverse temperature crystallization," *Nat. Commun.*, vol. 6, no. 1, p. 7586, 2015.

[179] D. N. Dirin, I. Cherniukh, S. Yakunin, Y. Shynkarenko, and M. V. Kovalenko, "Solution-Grown $CsPbBr_3$ Perovskite Single Crystals for Photon Detection," *Chem. Mater.*, vol. 28, no. 23, pp. 8470–8474, 2016.

[180] K. Mantulnikovs, P. Szirmai, M. Kollár, J. Stevens, P. Andričević, A. Glushkova, L. Rossi, P. Bugnon, E. Horváth, A. Sienkiewicz *et al.*, "Light-induced charge transfer at the $CH_3NH_3PbI_3/TiO_2$ interface—a low-temperature photo-electron paramagnetic resonance assay," *J. Phys. Photonics*, vol. 2, no. 1, p. 014007, 2020.

[181] O. E. Semonin, G. A. Elbaz, D. B. Straus, T. D. Hull, D. W. Paley, A. M. van der Zande, J. C. Hone, I. Kymissis, C. R. Kagan, X. Roy, and J. S. Owen, "Limits of Carrier Diffusion in n-Type and p-Type $CH_3NH_3PbI_3$ Perovskite Single Crystals," *J. Phys. Chem. Lett.*, vol. 7, no. 17, pp. 3510–3518, 2016.

[182] J. G. Labram, E. E. Perry, N. R. Venkatesan, and M. L. Chabinyc, "Steady-state microwave conductivity reveals mobility-lifetime product in methylammonium lead iodide," *Appl. Phys. Lett.*, vol. 113, no. 15, p. 153902, 2018.

[183] E. M. Hutter, G. E. Eperon, S. D. Stranks, and T. J. Savenije, "Charge Carriers in Planar and Meso-Structured Organic–Inorganic Perovskites: Mobilities, Lifetimes, and Concentrations of Trap States," *J. Phys. Chem. Lett.*, vol. 6, no. 15, pp. 3082–3090, 2015.

[184] S. Chattopadhyay, R. S. Kokenyesi, M. J. Hong, C. L. Watts, and J. G. Labram, "Resolving in-plane and out-of-plane mobility using time resolved microwave conductivity," *J. Mater. Chem. C*, vol. 8, pp. 10 761–10 766, 2020.

[185] E. M. Hutter, M. C. Gélvez-Rueda, A. Osherov, V. Bulović, F. C. Grozema, S. D. Stranks, and T. J. Savenije, "Direct-indirect character of the bandgap in methylammonium lead iodide perovskite," *Nat. Mater.*, vol. 16, no. 1, pp. 115–120, 2017.

[186] M. J. Hong, S. R. Svadlenak, K. A. Goulas, and J. G. Labram, "Thermal stability of mobility in methylammonium lead iodide," *J. Phys Mater.*, vol. 3, no. 1, p. 014003, 2019.

[187] C. C. Stoumpos, C. D. Malliakas, J. A. Peters, Z. Liu, M. Sebastian, J. Im, T. C. Chasapis, A. C. Wibowo, D. Y. Chung, A. J. Freeman, B. W. Wessels, and M. G. Kanatzidis, "Crystal Growth of the Perovskite Semiconductor $CsPbBr_3$: A New Material for High-Energy Radiation Detection," *Cryst. Growth Des.*, vol. 13, no. 7, pp. 2722–2727, 2013.

[188] v. Svirskas, S. Balčiūnas, M. Šimėnas, G. Usevičius, M. Kinka, M. Velička, D. Kubicki, M. E. Castillo, A. Karabanov, V. V. Shvartsman, M. de Rosário Soares, V. Šablinskas, A. N. Salak, D. C. Lupascu, and J. Banys, "Phase transitions, screening and dielectric response of $CsPbBr_3$," *J. Mater. Chem. A*, vol. 8, pp. 14 015–14 022, 2020.

[189] M. J. Trimpl, A. D. Wright, K. Schutt, L. R. V. Buizza, Z. Wang, M. B. Johnston, H. J. Snaith, P. Mueller-Buschbaum, and L. M. Herz, "Charge-Carrier Trapping and Radiative Recombination in Metal Halide Perovskite Semiconductors," *Adv. Funct. Mater.*, vol. 30, no. 42, p. 2004312, 2020.

[190] A. Takagi, K. Nomura, H. Ohta, H. Yanagi, T. Kamiya, M. Hirano, and H. Hosono, "Carrier transport and electronic structure in amorphous oxide semiconductor, a-$InGaZnO_4$," *Thin solid films*, vol. 486, no. 1-2, pp. 38–41, 2005.

[191] C.-Y. Park, S.-P. Jeon, J. B. Park, H.-B. Park, D.-H. Kim, S. H. Yang, G. Kim, J.-W. Jo, M. S. Oh, M. Kim *et al.*, "High-performance ITO/a-IGZO heterostructure TFTs enabled by thickness-dependent carrier concentration and band alignment manipulation," *Ceram. Int.*, vol. 49, no. 4, pp. 5905–5914, 2023.

[192] J. Sheng, T. Hong, H.-M. Lee, K. Kim, M. Sasase, J. Kim, H. Hosono, and J.-S. Park, "Amorphous IGZO TFT with high mobility of 70 $cm^2/(V\ s)$ via vertical dimension control using PEALD," *ACS Appl. Mater. Interfaces*, vol. 11, no. 43, pp. 40 300–40 309, 2019.

[193] R. Martins, P. Almeida, P. Barquinha, L. Pereira, A. Pimentel, I. Ferreira, and E. Fortunato, "Electron transport and optical characteristics in amorphous indium zinc oxide films," *J. Non-Cryst. Solids*, vol. 352, no. 9-20, pp. 1471–1474, 2006.

[194] J. Yao, N. Xu, S. Deng, J. Chen, J. She, H.-P. D. Shieh, P.-T. Liu, and Y.-P. Huang, "Electrical and photosensitive characteristics of a-IGZO TFTs related to oxygen vacancy," *IEEE Trans. Electron Devices*, vol. 58, no. 4, pp. 1121–1126, 2011.

[195] Y. Li, Y. Pei, R. Hu, Z. Chen, Y. Zhao, Z. Shen, B. Fan, J. Liang, and G. Wang, "Effect of channel thickness on electrical performance of amorphous IGZO thin-film transistor with atomic layer deposited alumina oxide dielectric," *Curr. Appl. Phys.*, vol. 14, no. 7, pp. 941–945, 2014.

[196] Y. Wang, X. W. Sun, G. K. L. Goh, H. V. Demir, and H. Y. Yu, "Influence of channel layer thickness on the electrical performances of inkjet-printed In-Ga-Zn oxide thin-film transistors," *IEEE Trans. Electron Devices*, vol. 58, no. 2, pp. 480–485, 2010.

[197] S.-H. Choi and M.-K. Han, "Effect of deposition temperature of SiOx passivation layer on the electrical performance of a-IGZO TFTs," *IEEE Electron Device Lett.*, vol. 33, no. 3, pp. 396–398, 2012.

[198] F. Zhou, H. Lin, L. Zhang, J. Li, X. Zhang, D. Yu, X. Jiang, and Z. Zhang, "Top-gate amorphous IGZO thin-film transistors with a SiO buffer layer inserted between active channel layer and gate insulator," *Curr. Appl. Phys.*, vol. 12, no. 1, pp. 228–232, 2012.

[199] K. Akaiwa, K. Kaneko, K. Ichino, and S. Fujita, "Conductivity control of Sn-doped α-Ga_2O_3 thin films grown on sapphire substrates," *Jpn. J. Appl. Phys.*, vol. 55, no. 12, p. 1202BA, nov 2016. [Online]. Available: https://dx.doi.org/10.7567/JJAP.55.1202BA

[200] H. Takane, H. Izumi, H. Hojo, T. Wakamatsu, K. Tanaka, and K. Kaneko, "Effect of dislocations and impurities on carrier transport in α-Ga_2O_3 on m-plane sapphire substrate," *J. Mater. Res.*, vol. 38, no. 10, pp. 2645–2654, May 2023. [Online]. Available: https://doi.org/10.1557/s43578-023-01015-8

List of Figures

2.1 The band structure of a semiconductor or insulator is shown in subfigure (a) with a filled valence band and a bandgap between the valence and conduction band. The band structure of a conductor is shown in subfigure (b) with a partially filled band. $g(\varepsilon)$ is the density of states at a given ε energy, E_g is the bandgap. The figure is from *Solid State Physics* by Neil W. Ashcroft and N. David Mermin [39]. 7

2.2 Energy levels of the acceptor and donor states in the band structure of semiconductors. From *Fundamentals of the physics of solids* by Jenő Sólyom[40]. . . . 10

2.3 (a): Temperature dependence of the chemical potential and (b): temperature-dependent regions of charge carrier generation by thermal excitation. From *Fundamentals of the physics of solids* by Jenő Sólyom[40]. 11

2.4 The crystal structure of methylammonium lead halide perovskites. The illustration on the left side presents one unit cell. From *Organic and Hybrid Solar Cells* by Lukas Schmidt-Mende, Stefan Kraner, and Azhar Fakharuddin[50]. The illustration on the right side presents the methylammonium group surrounded by eight octahedra of PbX_6. From *Ionic transport in hybrid lead iodide perovskite solar cells* by Christopher Eames *et al.*[51]. 12

2.5 Subfigure (a) presents the colloidal form of the $CsPbX_3$ perovskites. In subfigure (b) the shift in the normalized photoluminescence is shown as the halide content changes. The absorption (solid lines) and photoluminescence (dashed lines) spectra are presented in subfigure (c) for samples with different halide content. Subfigure (d) shows the transient photoluminescent signal of the perovskites as the halide content changes. From *Nanocrystals of Cesium Lead Halide Perovskites ($CsPbX_3$, X = Cl, Br, and I): Novel Optoelectronic Materials Showing Bright Emission with Wide Color Gamut*, Loredana Protesescu *et al.*[5]. 12

2.6 The structure of the cubic, tetragonal, and orthorhombic phases from two different viewpoints. The figure was made for tin-based perovskites. From *Tin Halide Perovskites: From Fundamental Properties to Solar Cells* by Matteo Pitaro *et al.*[74]. 13

2.7 Schematic representation of a tandem solar cell. From *Inorganic $CsPbI_3$ Perovskite-Based Solar Cells: A Choice for a Tandem Device* by Waqar Ahmad *et al.* [101]. 15

2.8 Schematic representation of the Shockley-Read-Hall, radiative, and Auger recombination process in subfigures (a), (b), and (c) respectively. From *Semiconductor Material and Device Characterization* by Dieter K. Schroder[133]. . . . 16

2.9 Injection-dependent lifetime for the Auger, SRH, and radiative recombination processes. The bulk lifetime is presented as well. The SRH process is shown for two different defects. From *Untersuchungen zur Ladungsträgerlebensdauer in kristallinem Silizium für Solarzellen* By Kevin Lauer [135]. 20

2.10 Dangling bonds on the surface of silicon wafers. P_1, P_b, and P_{b0} are the designations of the dangling bonds. From *Semiconductor Material and Device Characterization* by Dieter K. Schroder[133]. 20

2.11 The effective lifetime of charge carriers (τ_{eff} in the figure) as a function of wafer thickness (d) for multiple surface recombination velocity (s_r) values. From *Semiconductor Material and Device Characterization* by Dieter K. Schroder[133]. 21

2.12 Simulation of the surface impedance as a function of resistivity for two frequencies. The real and imaginary parts of the surface impedance are both shown in the graph. The green dotted line presents two typical values for low and highly-doped silicon. 23

2.13 Simulation of the reflection coefficient for the general, low conductivity, and high conductivity cases. The figure includes the real and imaginary part of the reflection coefficient besides its amplitude as well. The low and high conductivity cases fall on the general case at their respective regions. Note that the engineering notation is used for the horizontal scale. 24

2.14 Simulation of the reflection coefficient for multiple different probing frequency values. A shift can be observed in the reflection coefficient towards lower conductivity values as the frequency of the probing microwave signal increases. . . 25

2.15 Possible contact realization on the sample surface for the van der Pauw sheet resistance measurement. The image is taken from *Semiconductor Material and Device Characterization* by Dieter K. Schroder[133]. 29

2.16 Schematic drawing of the contacts for the sheet resistance measurement on the left side and the Hall effect measurement on the right side. 29

2.17 Schematic figure representing the direction of charge carrier transport, electric field, and magnetic field. 32

3.1 (a): Raw signal with the averaged values of the binning methods scattered on the signal. (b): Charge-carrier recombination dynamics calculated by smoothing the signal before the numerical derivation. (c-d): Charge-carrier recombination dynamics calculated by binning the measured data into linearly or logarithmically distributed bins. 37

3.2 Experimental setup built with a coplanar waveguide acting as the antenna. The measurement system includes a cryostat, a Q-switched pulsed laser that can be easily switched between 532 nm and 1064 nm output, a self-assembled microwave bridge responsible for the generation and downconversion of the microwave signal, and an oscilloscope for the transient photoconductivity measurement. 38

3.3 Left side: Photograph of the CPW placed on the cold finger of the cryostat. A sample is located on the surface of the CPW. The waveguide is terminated with two SMD resistances to realize a 50 Ω termination. Right side: cross-section of the conductor-backed coplanar waveguide. The dotted line in the insulator layer represents the via-holes. 39

3.4 The geometry of a conductor-backed CPW is presented on the left and in the middle. The image on the right side presents a quasi-TEM wave's electric and magnetic field distribution. From *RF and Microwave Engineering: Fundamentals of Wireless Communications* by Frank Gustrau [169]. 39

3.5 Equivalent circuit of a coplanar waveguide. The model is normalized to unit length. 39

3.6 Block diagram of the IQ mixer. Downloaded from the manufacturers website, https://markimicrowave.com/products/connectorized/iq-mixers/iq-0618lxp/datasheet/ [170]. 41

3.7 The PDL-1000 Hall effect measurement system is shown on the left side and the cylindrical magnet pair inside the measurement system is shown on the right side[174]. 44

3.8 Left side: Three methylammonium lead halide single crystals presented on millimeter paper for scale. From left to right: $CH_3NH_3PbI_3$, $CH_3NH_3PbBr_3$, and $CH_3NH_3PbCl_3$. Right side: $CsPbBr_3$ single crystal placed on millimeter paper for scale. 46

4.1 The experimental setup used for microwave photoconductivity measurements during the presented study is shown in subfigure (a). The block diagram includes the modification needed for switching between steady-state and transient photoconductivity measurements. (b) Schematic diagram of laser light delivery to the sample placed inside the microwave cavity with the TEM modes of the cavity presented. The illustration of the light delivery system is presented in subfigure (c). The left photo in (c) presents the quartz rod used during the measurement without the sample, the middle photo shows the same rod when the optical excitation is present, and the right photo shows the $MAPbBr_3$ sample attached to the rod ready for measurement. The optical excitation used for the illustration of the light delivery system is not the same, as the laser used for the measurement. The light source used for illustration is a CW LED with a wavelength of $\lambda = 470$ nm made by ADSresonances Sàrl. 49

4.2 Comparison of the measurement conducted with a lock-in amplifier and an oscilloscope. The figure on the right side presents the ability of the two measurement processes to follow the hysteretic effects of phase transition. 50

4.3 The recombination dynamics of photoexcited charge carriers observed through the decay of microwave reflection as a function of time. The red and black curves represent the recorded signals, and the red and green curves are the fitted single exponents. The large digital noise is the result of the relatively poor vertical resolution of the used oscilloscope. 51

4.4 charge-carrier lifetime (a-c) and photoconductance (d-f) as a function of temperature for $MAPbI_3$, $MAPbBr_3$, and $MAPbCl_3$ crystals. All investigated samples show maximal values in photoconductivity and ultralong charge-carrier recombination times at low temperatures. The maximal observed recombination time is over 68 μs for $MAPbBr_3$. The vertical lines represent the temperature of phase transitions. All samples show significant changes in both parameters at the orthorhombic to tetragonal phase transition. 52
4.5 Comparison of hysteretic effect around the phase transition measured with a lock-in amplifier (left panel) and an oscilloscope (right panel). 54
4.6 Reproducibility of photoconductivity and lifetime for three measurement runs. . 55
4.7 Charge-carrier lifetime (left panel) and photoconductivity (right panel) of a $MAPbBr_3$ single crystal as a function of increasing temperature after being cooled slowly and quickly. The charge-carrier recombination time is significantly shorter in the orthorhombic phase in the case of a quenched sample than for the same sample cooled slowly. The trend is the opposite for the photoconductivity, as the photoconductivity observed in the case of the quenched sample is approximately thrice the maximal value of the slowly cooled sample. 56
4.8 Charge-carrier recombination dynamics of three $MAPbBr_3$ samples with varying crystalline morphology. The top panel shows photographs of the three crystals. From left to right: the cubic, amorf (acid-based growth), and needle-shaped samples. Subfigure (a) presents the charge-carrier recombination time, and (b) presents the change in photoconductivity as a function of temperature. 58
4.9 Charge-carrier recombination dynamics of three $MAPbI_3$ samples with varying crystalline morphology. Subfigure (a) presents the charge-carrier recombination time, and (b) presents the change in photoconductivity as a function of temperature. 59

5.1 Block diagram of the realized measurement system. The device can be operated with CW and pulsed lasers as well and the signal may be recorded with a lock-in amplifier or an oscilloscope. 62
5.2 First observation of the ultralong recombination time of $CsPbBr_3$ at cryogenic conditions. The relaxations were recorded at 18.83 K in the case of subfigure (a), and 300.9 K in the case of subfigure (b). Note the very different time scales in the two experiments. 64
5.3 Transient photoluminescence measurement of the $CsPbBr_3$ single crystal at room temperature. The measurement was done by Hidetsugu Shiozawa. 65
5.4 The temperature-dependent microwave reflection of the CPW in the dark is presented without a sample in subfigure (a), with the $CsPbBr_3$ sample in subfigure (b), and the difference of these temperature-dependent reflection tendencies in subfigure (c). 66
5.5 The reflected microwave voltage as a function of time during the relaxation process at four different temperatures between 20 K and room temperature are presented in subfigures (a) and (c). The recombination time values as a function of time obtained through the analysis presented in the text for the same relaxation processes are shown in subfigures (b) and (d). The inset in subfigure (d) shows the measured single crystal sample. 67

5.6 Subfigure (a) presents the charge-carrier recombination time as a function of reflected microwave signal of a $CsPbBr_3$ single crystal at 7 temperature values between 18 K and room temperature. The maximal value of the reflected signal is presented in subfigure (b). The recombination time measured at the beginning and end of the recombination process as well as the recombination time obtained from the steady state measurement is shown in subfigure (c). All measurements were conducted at an average irradiance of approximately 399 μJ/cm^2. 69
5.7 Charge-carrier recombination time as a function of reflected microwave voltage at different temperature settings for two $CsPbBr_3$ samples. 69
5.8 Measurement of the maximal value of the decay curve in subfigure (a) and charge-carrier recombination time at the beginning and end of the recombination process in subfigure (b) as a function of temperature with a higher resolution in the temperature sweep. The averaging of TRMCD curves was lowered to decrease the time needed for the measurement. The subpar signal-to-noise ratio leads to higher standard deviation for the τ_c values and the inability to measure the end of the recombination process above 200 K. 71
5.9 Charge-carrier recombination time of the $CsPbBr_3$ single crystal at 6 different temperatures with various excitation levels. The recombination time values are shown as a function of reflected microwave voltage. An arrow on the graphs corresponding to 20 K and 150 K temperatures shows the increasing fluence of the excitation settings. 73
5.10 Band model of $CsPbBr_3$ with the escape and capture processes noted in the figure. The band model used here consists of a trap and an SRH state besides the valence and conduction band. 74
5.11 Subfigure (a) shows the recombination dynamics with only one recombination process. The process is a trap state that can capture electrons and holes with different capture rates. The recombination process happens when a trap state captures charge carriers of both types. (b) shows the carrier recombination time as a function of carrier concentration with a shallow and a deep-level trap included in the model. It should be noted, that the x-axis represents the density of free electrons and holes, while the $n(t=0)$ initial excitation represents the excitation of electron-hole pairs. This means that $n(t=0)=1$ excites 1 a.u. electrons and 1 a.u. holes that lead to an initial value of $n=2$ in the x-axis. . . . 75
5.12 Charge carrier concentration values for electrons and holes in individual charge states obtained during the simulation. 77

6.1 Dynamics of sheet resistance during and after illumination is presented in subfigure (a). The time domain before the black vertical division presents illuminated measurements, this region is followed by the relaxation of sample properties in the dark. The fitted curves are single exponents. Subfigures (b, c, d) show the variation in measured parameters caused by the different excitation of the samples between taking them out of the containment and placing them in the measurement unit. 82
6.2 Illumination-dependent charge carrier concentration, sheet resistance, and mobility recorded on the same sample simultaneously. The vertical divisions in the figure separated the illumination levels. 83

6.3 Reproducibility of the measurement observed for several runs. The charge carrier mobility is shown on the left, carrier concentration in the middle, and sheet resistance on the right. All presented measurements were recorded as a function of time with the same illumination before the relaxation process. 83
6.4 The mobility of charge carriers recorded in the three runs presented as a function of charge carrier density. 84
6.5 Charge carrier density (a) and mobility (b) values as a function of time after excitation for five different sample variations. The vertical yellow line presents the division between illuminated and dark conditions. 85
6.6 Comparison of the change in conductivity for three different parameters: sample thickness (a), presence of an insulator layer (b), and oxygen content during sample preparation (c). All presented graphs include the rise during excitation and relaxation in the dark of conductivity. 86
6.7 Effect of persistent photoconductivity on the Ga_2O_3 sample during and after optical excitation with the help of an ultraviolet LED. The excitation-dependent change is presented in subfigure (a). The subfigure shows the sheet resistance as the illumination is increased and decreased. The time dependence of sheet resistance is presented in (b) during illumination and after excitation in the dark. 88
6.8 Mobility of charge carriers as a function of charge carrier density. The measurement was conducted by increasing and decreasing the optical excitation. . . 88